The Dissertation Committee for Yunping Fei Certifies that this is the approved version of the following dissertation:

Functional Polymer Grafted Nanoparticles Synthesis, Characterization and Applications

Committee:

Christopher J. Ellison, Supervisor

Donald R. Paul

Isaac C. Sanchez

Benny D. Freeman

Wei Li

Functional Polymer Grafted Nanoparticles Synthesis, Characterization and Applications

by

Yunping Fei, B.E.

Dissertation

Presented to the Faculty of the Graduate School of

The University of Texas at Austin

in Partial Fulfillment

of the Requirements

for the Degree of

Doctor of Philosophy

The University of Texas at Austin

December 2016

Dedication

Dedicated to my grandpa Fen Fei, who was the first hard-working engineer I have seen in my life.

Acknowledgements

First of all, I would like to thank my advisor Dr. Christopher Ellison. I deeply appreciate the opportunity he offered for me to join his group six years ago, when I was bold enough to tell him that I was interested in working in the research area of polymer, with little knowledge about polymer or lab experience. During the past six years, Dr. Ellison has provided me with guidance and advice on my research, as well as encouragements and support during my struggles in grad school. I believe the lessons I learned as a grad student in this group will benefit my career in the future. I am very grateful for all my committee members, Profs. Donald Paul, Isaac Sanchez, Benny Freeman and Wei Li for their input and advice to my research and the very helpful courses they taught.

Secondly, I would like to thank my first mentor since I joined the lab, Jeff Easley. The beginning of my lab work would have been much harder if I did not have Jeff as my mentor, who demonstrated how to set up a reaction in the hood repeatedly till I felt comfortable doing it by myself, who was always patient in answering my questions. I also learned a lot of useful lab skills from Christian Jarquin, who was then an undergrad on the project. At the beginning of my Ph.D., my lab-mates Dr. Josh Katzenstein, Dr. Julie Cushen, Paola Gonzalez, Dr. Dustin Janes, and Dr, Kadhir Shanmuganathan all played important roles in helping me fit in the new lab environment. I appreciate their help very much.

I could not have made it through my Ph.D. without the support I received from many incredible Ellison group members. Here, I want to give my special thanks to Sunshine Zhou and Reika Katsumata, who have helped me extensively in lab and also made me a more outgoing person. I know that our friendship will extend far beyond grad

school. I appreciate my friend Dr. Chae Bin Kim who was always there to give me his frank opinions. Dr. Amanda Jones has been an invaluable editor for my manuscripts and dissertation, who I have had so much fun sharing an office with. I feel very lucky to have worked and become friends with Dr. Joon Hee Cho, Dr. Heonjoo Ha, Greg Blachut, Philip Liu, Melanie Merrick, Dr. Sateesh Peddini and Dr. Raj Tiwari.

From my 4th year here, I had an opportunity to join the project funded by Advanced Energy Consortium (AEC). I appreciate Dr. Keith Johnston very much for giving me the opportunity to join such an exciting project. I have learned so much from working with different people who have different working styles and on a variety of research topics. I would like to thank the people who I have worked closely with on the AEC project: Dr. Muhammad Iqbal, Dr. Zheng Xue, Dr. Esteban Urena, Dr. Joohyung Lee, Dr. Abhijit Paul, Dr. Lynd Foster, Dr. Seong Kong, Edward Lin, Eric Larsen, and Chola Dandamudi. I want to thank the undergrad researchers Yi Lu, Prashant.Ranganath, Kevin Javier, who have not only made contributions to the project, but also trained me to be a better mentor. The work we have accomplished would not have been possible without our collaborators from other institutions, including Drs Alp Esen and Wenli Bi from Argonne National Lab, and Prof. Linda Doerrer and Jesse Guillet from Boston University, who performed Mössbauer spectroscopy measurements and data fitting, and Prof. Kurt Pennell and Dr. Bonnie Lyon from Tufts University who did awesome work on dynamic flow column experiments with our synthesized nanoparticles. I am also grateful for the help from the AEC coordinators Drs. Mohsen Ahmadian and Carla Thomas on this highly collaborative project.

There are many people who have offered their incredible support and friendship to me throughout my years as a grad student at UT Austin. First, I want to thank two professors in Tongji University who shared their own experience with me and strongly encouraged me to pursue a Ph.D. degree in the US when I was an undergrad. I also felt

extremely blessed to have my close friend Linyi Gu as a companion through the application process to grad school. My life in the US would not have been this happy if I have not met Yingying Jiang, Mengqi Yuan, Qian Shao and Xiaotang Lu. Xiaotang Lu, in particular, was more than an amazing roommate, interesting friend, who also served as my teacher (together with her lab-mate Yixuan Yu) in helping me get on track for the nanoparticle synthesis. I am blessed to have the unwavering support from Sihong Ma, who I have known since we were both 15. Last but super importantly, I would like to thank my parents whom I knew would always have my back no matter what happens and who gave me the happiness genes!

Functional Polymer Grafted Nanoparticles Synthesis, Characterization and Applications

Yunping Fei, Ph.D.

The University of Texas at Austin, 2016

Supervisor: Christopher J. Ellison

Incorporating nanoparticles and polymers into one composite material have opened new pathways for generating novel material structures and advancing the properties of conventional materials. The developments in the field of nanocomposites have been accelerated by the progress in fabrication of nanoparticles with designed shape and precise size control, surface modification techniques covering a variety of nano-scale materials including clay sheets, carbonaceous materials, metal oxide particles, etc., as well as new syntheses of polymers with targeted architecture and functionality. The control of interfacial interactions is the key to property enhancement of almost all nanocomposite materials. Grafting polymer chains directly onto the surface of nanoparticles is a relatively new approach for obtaining novel nanocomposite structures and it offers better control of grafting density and maximizes the interfacial interactions between nanoparticles and polymeric matrices.

The first project in this thesis describes the preparation of nanocomposites via surface initiated polymerization of block copolymer chains directly from the surface of montmorillonite clay. A 'graft-from' synthesis protocol was developed for the preparation of the nanocomposites. Comprehensive material characterization was performed to understand the structure and properties of the nanocomposites. Crystallization behavior of

the bulk material and optical properties of nanocomposite films were examined. The relationship between material synthesis, structure and properties is also discussed in these chapters.

The second project involves grafting polyelectrolytes onto magnetic nanoparticles for the application of electromagnetic imaging in high temperature, high salinity gas and oil reservoir environments. The fabrication of magnetic nanoparticles is described with a focus on both size control and achieving colloidal stability. The synthesized nanoparticles were used as core materials for their outstanding magnetic properties. Subsequent surface functionalization and a 'grafting-to' method was developed to coat the nanoparticles with a surface layer of polyelectrolytes, which provides nanoparticles with excellent transport mobility for high temperature, high salinity aqueous flow conditions through porous rock and sediment.

Table of Contents

List of Tables

List of Figures

List of Schemes

Chapter 1. Overview of Polymer Grafted Nanoparticles

1.1 Introduction to Nanocomposite Materials

Both the rapid progress in material synthesis and emergence of nanotechnology have enabled scientists to merge the unique features of both inorganic nanoparticles and polymeric materials into one composite material.[1–5] Some examples of the desirable properties, which can often be synergistically combined, include the mechanical properties and heat and flame resistance of clays, barrier properties of inorganic materials and flexibility of polymers, and the optical transparency and easy processability of polymeric materials.[6–9] The first industrially relevant nanocomposite product was a nylon 6-clay hybrid material produced by Toyota researchers in 1993 which showed impressive mechanical reinforcement and increased heat distortion temperature compared to bulk nylon 6 by adding 1-5 wt% of clay nanoplatelets.[10,11] This led to the first use of lightweight polymer based composites as engine covers in passenger automobiles. Though improvement in mechanical properties is often a first target, other property enhancements through the addition of nanoparticles have been explored including conductivity, magnetic responsiveness, flame retardancy, barrier properties and so on.[6,7,12–18] The developments in the field of nanocomposites have also been accelerated by the progress of surface modification techniques covering a variety of nano-scale materials including clays, carbon nanotubes, metal oxide particles, and graphene sheets.[19–23] Other advancements in the synthesis of polymers with targeted functional groups, polymer processing techniques and grafting procedures for attaching polymers onto nanoparticles further added to the development of the nanocomposite field.[4,8,9,24,25]

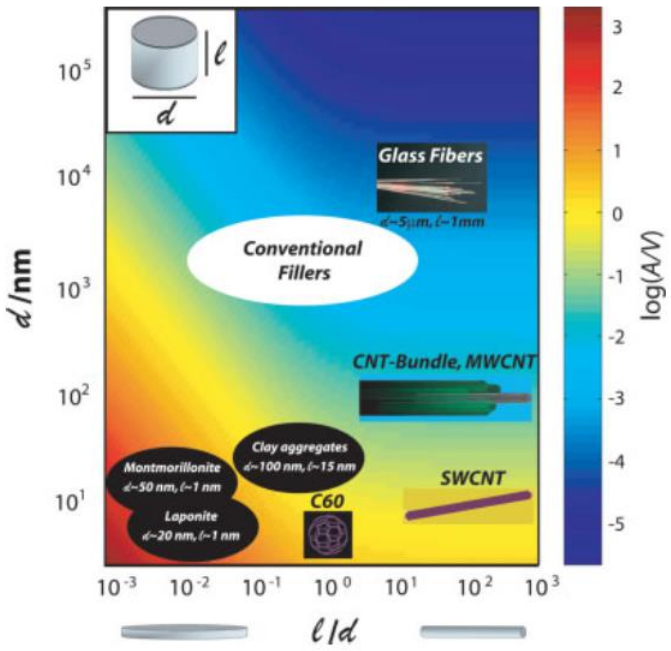

Figure 1.1: Calculated interfacial area per volume (A/V) of particles (in nm^{-1}), assuming a right-circular cylindrical particle shape, for different particle diameters and aspect ratios. Exfoliated clay (laponite or montmorillonite) particles, spherical nanoparticles, and single-walled carbon nanotubes (SWCNTs) generate up to four orders of magnitude more interfacial area compared to conventional filler materials like glass fibers of equal volume-filling fraction (MWCNT: multi walled carbon nanotube). Reproduced with permission from ref.[12] Copyright © 2005 WILEY-VCH Verlag GmbH & Co. KGaA, Weinheim.

The property enhancements observed in nanocomposite materials by incorporating nanofillers into polymeric matrices have exceeded those that have been observed in previous generations of composite materials, where the featured dimension of the fillers was on the micron scale (**Figure 1.1**).[5,12,26,27] The primary reason for this improvement was attributed to the interaction between the filler and polymer matrix on a molecular scale (1-100 nm). With proper dispersion of the nanofillers in the host polymer matrix (i.e. no or limited agglomerations), the size of the nanofiller is comparable in magnitude with the

characteristic feature sizes of the host polymer matrix such as the radius of gyration (*Rg*) of polymer chains. Other, more sophisticated polymers such as block copolymers (BCP) can introduce domain-segregated features (~1-100 nm) to be considered in nanocomposites. BCPs can form different morphologies on the nanoscale, depending on the degree of incompatibility between blocks (χ), degree of polymerization (N), and block volume composition (f_A) (**Figure 1.2**).[28] In the case that the host matrix is a BCP, the nanofiller dispersion can potentially be further stabilized (or compatibilized) by preferentially wetting the filler surface with one block and/or completely disturb the phase segregation and shift the BCP phase diagram from that of neat BCP.[12,29] This size compatibility between BCP domains and nanofillers provides new opportunities for controlling filler dispersion and orientation,[30,31] as well as introducing new methods for impacting the microstructure of the BCP.[12,32–34] This can result in substantial changes in bulk material properties, which cannot be achieved by conventional micro-filler composites due to the disparity in feature size.

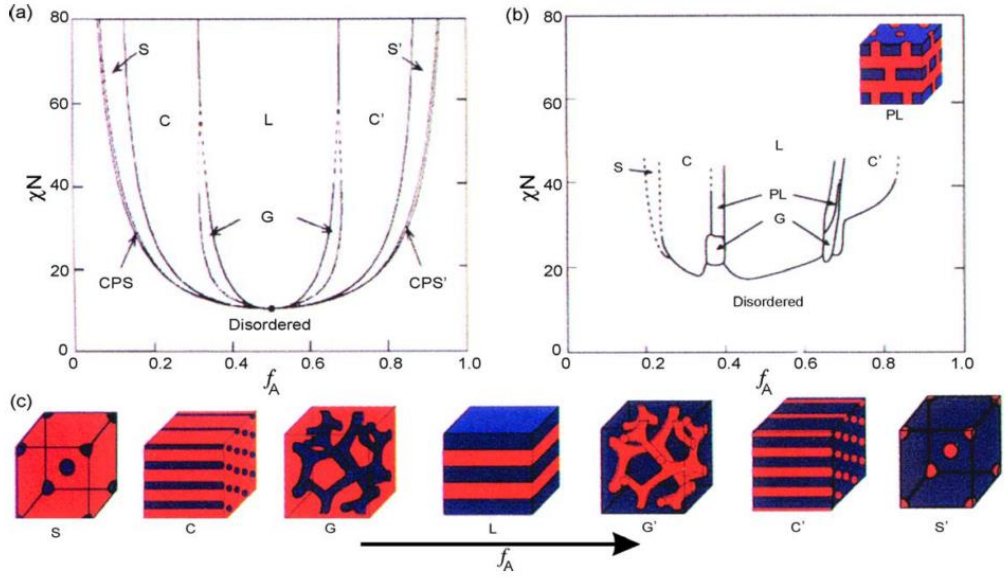

Figure 1.2: (a) Phase diagram for linear AB diblock copolymer predicted by self-consistent mean field theory, including four equilibrium morphologies: spherical (S), cylindrical (C), gyroid (G) and lamellar (L), depending on the composition f_A and domain segregation strength parameter χN. (b) Experimental data proved the theoretical prediction. (c) A variety of domain segregated geometries are observed as a function of relative lengths (proportional to f_A) of the two blocks. Reproduced from Block Copolymers-Designer Soft Materials, with the permission of the American Institute of Physics.[28] (DOI: http: //dx.doi.org/10.1063/1.882522)

1.2 Fundamental Considerations for Dispersing Nanoparticles in Polymeric Matrices

Dispersing nanofillers evenly within the polymer matrix is expected to maximize polymer-filler contacts leading to the largest possible property enhancements or synergies. Achieving a good dispersion, however, is not trivial due to the intrinsic disparity of surface energy that is often encountered between the two components. In a nanocomposite system, the degree of dispersion of a nanofiller is directly linked to the interplay of enthalpy and entropy. The enthalpy of the nanocomposite system is determined by the affinity of the polymer chains to the surface of nanofillers, while the entropy is indicated by the number of configurations that the polymer chains and nanofillers can adopt in the nanocomposite

system. When an inorganic material and polymer are mixed, often where there is little to no chemical affinity between the two, they will simply form a macroscopically phase separated mixture. When the surface of the filler has been chemically modified to be more compatible with the polymer matrix, some polymer chains will migrate to the particle surface during the nanocomposite preparation process and reside in the interstitial regions between particles, forming an intercalated structure. These regions between particles can be small enough to have a nanoconfinement effect on the polymer chains within them.[35] The associated entropic penalty of locating chains between particles, however, can be offset or overcome by the change in system enthalpy if there is sufficient attraction between the polymer segments and the surface modifier on the nanofiller. In this most desired situation more polymer chains migrate into the regions between the particles during the preparation process forcing the distance between the filler particles to increase by polymer steric repulsion, eventually reaching an exfoliated state where the structural order of the nanofiller is completely lost and a good dispersion is achieved. The system entropy is maximized at this stage, where the fillers are homogeneously dispersed throughout the polymer matrix. A mean-field, lattice-based model of polymer melt intercalation of an organically-modified layered silicate (OLS; also called organically-modified clay) has been proposed by Vaia and Giannelis, which indicated that complete exfoliation of clay fillers can be obtained if polymer occupies every potential interaction site on the surface of the OLS. Furthermore, more polar or hydrophilic polymers, which have a higher affinity for the OLS surfaces, achieve an even higher degree of exfoliation in bulk nanocomposites.[36,37]

Besides chemical composition (which determines the mixing enthalpy), the size and shape compatibility of the nanofiller and the host polymer matrix should also be considered when preparing nanocomposites. Shape contributes to both the interaction

between individual nanofillers as well as between the fillers and the molecular features of the host polymer matrix on the nanoscale. Progressing from spherical nanoparticles (zero-dimensional) to cylindrical nanorods (one-dimensional) to nanoscale thick sheets (two-dimensional) increases the energy of interaction per pair of nanoparticles and, therefore, increases the complexity of the filler dispersion in polymer matrix.[4] When nanofillers are dispersed in a BCP matrix with a specific microstructure, shape compatibility of the filler with the BCP microstructure should be considered in order to maximize the contact area between the particle surface and the favorable contacting domain in the BCP matrix (**Figure 1.3**).[12]

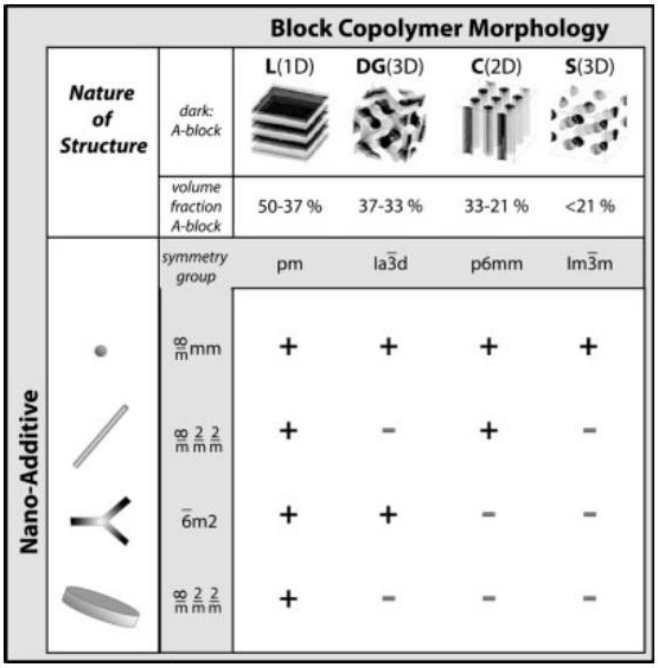

Figure 1.3: Schematic BCP phase diagram showing the various "classical" non-crystalline diblock copolymer microdomain morphologies. The dark domain is the minority domain that is embedded in the majority domain (light). The "symmetry compatibility map" lists the commensurate combinations of particle point-group and BCP space-group representations, respectively. The compatibility of a particle's point symmetry group within the minority component of a respective BCP space group is indicated by (+), incompatibility by (-). L=lamellar, DG=double gyroid, C=cylindrical, and S=spherical BCP morphologies. Reproduced with permission from ref.[12] Copyright © 2005 WILEY-VCH Verlag GmbH & Co. KGaA, Weinheim.

1.3 Preparation Methods for Nanocomposites

Different processing techniques of producing nanocomposites have been developed with the goal of dispersing inorganic nanoparticles homogeneously in a polymer matrix. The most common approaches include melt blending, solution intercalation, and surface grafting of polymers. As the most widely adopted method by industry to date, melt blending is a process involving heating the polymer to a liquid melt above its glass transition temperature (T_g) and crystallite melting temperature (T_m), mixing with

nanofillers and surfactant additives if necessary, and processing by extrusion or injection molding. It is a relatively economical process with the obvious advantages of being readily compatible with industrial mass production facilities and many formulations with commercial polymer feedstock are easily possible. However, the degree of disaggregation of particles or delamination of nano-platelets after processing by melt blending is affected by the viscosity of the polymer melt and duration of the process. Even so, the key factor is still the chemical affinity between the polymer chains and nanoparticle surfaces. For most cases, the composite system is composed of polar fillers and a non-polar polymer matrix, and it remains difficult to achieve ideal dispersions via melt blending.

Solvent intercalation is another method to overcome mixing challenges between nanoparticles and polymers. This method uses a solvent to simultaneously dissolve the polymer and disperse the nanoparticles. Here, the solution acts as an intermediate platform for a homogeneous mixture of the two components, which were originally immiscible. A nanocomposite film can be obtained once the solvent is evaporated. Spin coating and solution casting methods can be used depending on the target thickness of the film product. The main challenge with this technique is to control solvent evaporation kinetics in order to produce a high quality casted film.

Given the chemical incompatibility between the often times polar nanoparticle surfaces and non-polar polymer matrix, agglomeration of nanoparticles and phase separation between the filler and matrix remain challenging issues for a variety of nanocomposite systems. Attempts have been made to form nanocomposites by grafting polymers directly on the surface of nanofillers. The two major routes are the ‘graft-to’ method and the ‘graft-from’ method. Both of these methods require certain surface modification procedures for the nanoparticle surfaces so to form reactive functional groups on the nanoparticle surfaces as anchors for polymer chains in the subsequent grafting step.

The graft-to method forms polymer grafted nanoparticle structures by reacting previously synthesized polymer chains with functional groups on the surface modified nanofillers. Given the long chain coiled structure of most polymers, it is straightforward that steric hindrance may, to some extent, limit the grafting density of the polymer chains. The other method, graft-from, involves grafting surface initiators on the nanoparticles, mixing the nanoparticles with a monomer of choice, and performing a subsequent in situ polymerization step initiated directly from the nanoparticle surfaces. This approach enables formation of a dense polymer brush structure on the nanoparticle surface by minimizing the steric repulsion during the grafting process.

Formation of nanocomposites through direct grafting of polymer chains onto nanoparticle surfaces is a relatively new approach for obtaining novel nanocomposite structures. Better control of grafting density and a higher degree of homogeneous nanoparticle distribution can both be achieved, leading to improved bulk properties (i.e. optical, mechanical). Furthermore, alternative interesting morphologies can be generated via grafting polymer chains onto the nanoparticle, the study of which probe the understanding of interfacial interactions and help establish synthesis-structure-property relationships.

1.4 Synthetic Approaches for Surface Initiated Polymerization

1.4.1 Anionic and cationic polymerization

Anionic and cationic polymerizations enable precise targeting of molecular weight and low polydispersity, but remain highly intolerant of impurities such as oxygen or water due to the reactivity of anions or cations. Previous studies focusing on synthesis of polystyrene from the nanoparticle surface have revealed the challenges in adapting these techniques in surface initiated polymerizations. Polystyrene has been grafted from TiO_2

particle surfaces by using 2,2′-azobis(2-amidinopropane) dihydrochloride (AIBA) as an initiator for in situ polymerization.[8] Attempts have also been made to synthesize polystyrene via anionic polymerization from clay surfaces after attaching a 1,1-diphenylethylene (DPE) derivative (functionalized by a triethylammonium bromide group) as a surface initiator on the clay surface.[38] High temperature (120 °C) and high vacuum were required to remove trace impurities, such as H_2O, for successful growth of monodisperse polymer chains. Due to the affinity to oxygen and moisture, the often times hydrophilic inorganic nanoparticle surface is inherently undesirable for in situ anionic or cationic polymerization processes.

1.4.2 Controlled free radical polymerization

1.4.2.1 Atom transfer radical polymerization (ATRP)

The Matyjaszewski group is credited with developing a versatile and robust ATRP synthesis protocol with a number of mechanistic studies and supporting kinetic modeling work.[39–43] As is illustrated in **Figure 1.4**, the ATRP equilibrium (characterized by $K_{ATRP} = k_{act}/k_{deact}$) involves homolytic cleavage of an alkyl halide bond R–X using a reversible redox reaction of a transition metal complex activator Mt^n/L (metal/ligand complex), which subsequently generates an alkyl radical R• and the corresponding higher oxidation state metal halide deactivator Mt^{n+1}/L (**Figure 1a**). The free radical R• can then propagate with a vinyl monomer (M), be deactivated in this equilibrium by Mt^{n+1}/L, or be terminated by either coupling or disproportionation with another R•, at which point two equivalents of deactivator accumulate as persistent radicals (persistent radical effect). With appropriate selection of the complexing ligand of the ATRP catalyst (and consequently, the reducing power of the complex), the ATRP equilibrium (**Figure 1.4**) can be easily and appropriately

adjusted for more or less reactive monomers. The rate of polymerization is proportional to the activator/deactivator ratio ((Mt^n/L):(Mt^{n+1}/L)) in the system.

Due to the persistent radical effect, one can easily rationalize that high amounts of transition metal catalyst are required in order to maintain the rate of polymerization and reach high conversion as the activator/deactivator ratio decreases with time (i.e. as Mt^{n+1}/L accumulates in the reaction). For situations where a high amount of metal catalyst in polymer products should be avoided, two variations of normal ATRP have been introduced: initiators for continuous activator regeneration (ICAR) ATRP and activators regenerated by electron transfer (ARGET) ATRP. ICAR ATRP uses a small amount of free radical initiators to constantly regenerate Mt^n/L activators, which are otherwise consumed by radical termination. This polymerization scheme can lead to additional homopolymer chains generated by the free radical initiators, which could alter the properties if one is synthesizing a BCP.

In an ARGET ATRP reaction, a mild reducing agent is often added to aid the regeneration of Mt^n/L activators, which do not generate new polymers. Tin(II) 2-ethylhexanoate ($Sn(EH)_2$)[44] or ascorbic acid[45] are most frequently used as reducing agents. When the mild reducing agent is added in excess, constant regeneration of the Mt^n/L activators throughout the polymerization process becomes possible, and therefore the amount of metal catalyst needed for a reasonable polymerization rate and low polydispersity is dramatically reduced. Previous work by Jakubowski et al. demonstrated good control over polystyrene synthesis with ARGET ATRP using only 10ppm Cu catalyst (more than 100 times less catalyst than a typical normal ATRP process).[42] Thus, ARGET ATRP is a powerful technique for achieving good control over polymer topologies and targeting a variety of monomer compositions/ functionalities for synthesizing homopolymers, BCPs, or surface initiated polymers.[39,42,46]

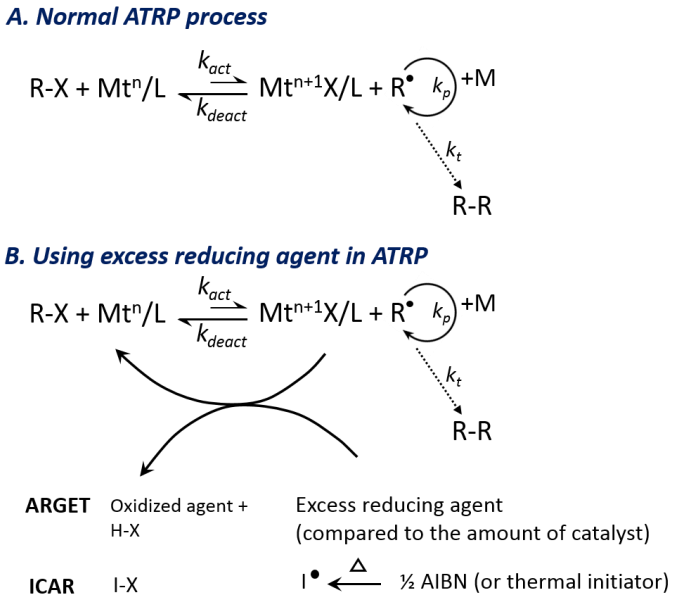

Figure 1.4: Reaction mechanisms for ATRP, ICAR ATRP and ARGET ATRP processes.[39]

1.4.2.2 Radical addition-fragmentation chain transfer (RAFT) polymerization

RAFT is a living radical polymerization, which offers good control over molecular weight and the polydispersity index.[47,48] Certain dithio compounds are used as highly efficient reversible addition-fragmentation chain transfer agents to provide this polymerization technique with living characteristics. The unavoidable (small amount) byproduct of homopolymer chains remains an issue for synthesis of BCPs and the sequence of the blocks formed during synthesis is sometimes predetermined due to the nature of the RAFT chain transfer agent.

1.5 PROJECT OVERVIEW

This chapter (and much of the work within this thesis) has focused on the goal of maximizing the interaction between a polymer matrix and nanofillers. To that end, my

research has been focused on synthesis, structural characterization, and structure-property relationships of polymer-inorganic nanocomposite systems prepared by grafting polymers directly from or to the surface of the nanoparticles. Chapters 2 and 3 focus on preparation of nanocomposites via surface initiated polymerization of BCP chains directly from the surface of montmorillonite clay. By using the graft-from method, a high degree of clay exfoliation was achieved. The resulting microstructure of the BCP matrix as well as the optical properties of the nanocomposite film were examined. Chapters 4-7 focus on grafting polyelectrolytes onto magnetic nanoparticles so that the composite material can survive high salinity solutions at high temperature for oil reservoir mapping applications. In this system, we fabricated the nanocomposite by the graft-to method and the colloidal stability of the clusters (formed by nanoparticles) and their transport properties are examined and discussed.

1.6 REFERENCES

(1) Balazs, A. C.; Emrick, T.; Russell, T. P. Nanoparticle Polymer Composites: Where Two Small Worlds Meet. *Science* **2006**, *314*, 1107–1110.

(2) Paul, D. R.; Robeson, L. M. Polymer Nanotechnology: Nanocomposites. *Polymer (Guildf).* **2008**, *49*, 3187–3204.

(3) Kumar, S. K.; Jouault, N.; Benicewicz, B.; Neely, T. Nanocomposites with Polymer Grafted Nanoparticles. *Macromolecules* **2013**, *46*, 3199–3214.

(4) Krishnamoorti, R. Strategies for Dispersing Nanoparticles in Polymers. *MRS Bull.* **2007**, *32*, 341–347.

(5) Krishnamoorti, R.; Vaia, R. A. Polymer Nanocomposites. *J. Polym. Sci. Part B Polym. Phys.* **2007**, *45*, 3252–3256.

(6) LeBaron, P.; Wang, Z.; Pinnavaia, T. Polymer-Layered Silicate Nanocomposites: An Overview. *Appl. Clay Sci.* **1999**, *15*, 11–29.

(7) Gilman, J. W.; Kashiwagi, T.; Lichtenhan, J. D. Nanocomposites: A Revolutionary New Flame Retardant Approach. *Sampe Journal*, 1997, *33*, 40–46.

(8) Bourgeat-Lami, E. Organic–Inorganic Nanostructured Colloids. *J. Nanosci. Nanotechnol.* **2002**, *2*, 1–24.

(9) Althues, H.; Henle, J.; Kaskel, S. Functional Inorganic Nanofillers for Transparent Polymers. *Chem. Soc. Rev.* **2007**, *36*, 1454.

(10) Kojima, Y.; Usuki, A.; Kawasumi, M.; Okada, A.; Kurauchi, T.; Kamigaito, O. Synthesis of Nylon 6–clay Hybrid by Montmorillonite Intercalated with ε-Caprolactam. *J. Polym. Sci. Part A Polym. Chem.* **1993**, *31*, 983–986.

(11) Kojima, Y.; Usuki, A.; Kawasumi, M.; Okada, A.; Fukushima, Y.; Kurauchi, T.; Kamigaito, O. Mechanical Properties of Nylon 6-Clay Hybrid. *J. Mater. Res.* **1993**, *8*, 1185–1189.

(12) Bockstaller, M. R.; Mickiewicz, R. a.; Thomas, E. L. Block Copolymer Nanocomposites: Perspectives for Tailored Functional Materials. *Adv. Mater.* **2005**, *17*, 1331–1349.

(13) Liff, S. M.; Kumar, N.; McKinley, G. H. High-Performance Elastomeric Nanocomposites via Solvent-Exchange Processing. *Nat. Mater.* **2007**, *6*, 76–83.

(14) Fredrickson, G. H.; Bicerano, J. Barrier Properties of Oriented Disk Composites. *J. Chem. Phys.* **1999**, *110*, 2181.

(15) Lin, Y.; Böker, A.; He, J.; Sill, K.; Xiang, H.; Abetz, C.; Li, X.; Wang, J.; Emrick, T.; Long, S.; *et al.* Self-Directed Self-Assembly of Nanoparticle/copolymer Mixtures. *Nature* **2005**, *434*, 55–59.

(16) Oberdisse, J. Aggregation of Colloidal Nanoparticles in Polymer Matrices. *Soft Matter* **2006**, *2*, 29–36.

(17) Payne, A. R. Effect of Dispersion on Dynamic Properties of Filler-Loaded Rubbers. *Rubber Chem. Technol.* **1966**, *39*, 365–374.

(18) Zhu, Z.; Thompson, T.; Wang, S.; von Meerwall, E. D.; Halasa, A. Investigating Linear and Nonlinear Viscoelastic Behavior Using Model Silica-Particle-Filled Polybutadiene. *Macromolecules* **2005**, *38*, 8816–8824.

(19) Bartholmai, M.; Schartel, B. Layered Silicate Polymer Nanocomposites: New Approach or Illusion for Fire Retardancy? Investigations of the Potentials and the Tasks Using a Model System. *Polym. Adv. Technol.* **2004**, *15*, 355–364.

(20) Moniruzzaman, M.; Winey, K. I. Polymer Nanocomposites Containing Carbon Nanotubes. *Macromolecules* **2006**, *39*, 5194–5205.

(21) Yoo, B. M.; Shin, H. J.; Yoon, H. W.; Park, H. B. Graphene and Graphene Oxide and Their Uses in Barrier Polymers. *J. Appl. Polym. Sci.* **2014**, *131*, 1–23.

(22) Li, X.; Zhu, Y.; Cai, W.; Borysiak, M.; Han, B.; Chen, D.; Piner, R. D.; Colombo, L.; Ruoff, R. S. Transfer of Large-Area Graphene Films for High-Performance Transparent Conductive Electrodes. *Nano Lett.* **2009**, *9*, 4359–4363.

(23) Peng, E.; Wang, F.; Xue, J. M. Nanostructured Magnetic Nanocomposites as MRI Contrast Agents. *J. Mater. Chem. B* **2015**, *3*, 2241–2276.

(24) Kumar, S. K.; Jouault, N.; Benicewicz, B.; Neely, T. Nanocomposites with Polymer Grafted Nanoparticles. *Macromolecules* **2013**, *46*, 3199–3214.

(25) Mackay, M. E. General Strategies for Nanoparticle Dispersion. *Science.* **2006**, *311*, 1740–1743.

(26) Fischer, H. Polymer Nanocomposites: From Fundamental Research to Specific Applications. *Mater. Sci. Eng. C* **2003**, *23*, 763–772.

(27) Jancar, J.; Douglas, J. F.; Starr, F. W.; Kumar, S. K.; Cassagnau, P.; Lesser, a. J.; Sternstein, S. S.; Buehler, M. J. Current Issues in Research on Structure–property Relationships in Polymer Nanocomposites. *Polymer (Guildf).* **2010**, *51*, 3321–3343.

(28) Bates, F. S.; Fredrickson, G. H. Block Copolymers—Designer Soft Materials. *Phys. Today* **1999**, *52*, 32.

(29) Vaia, R. A.; Wagner, H. D. Framework for Nanocomposites. *Mater. Today* **2004**, *7*, 32–37.

(30) Srivastava, S.; Agarwal, P.; Archer, L. A. Tethered Nanoparticle–Polymer Composites: Phase Stability and Curvature. *Langmuir* **2012**, *28*, 6276–6281.

(31) Tao, P.; Viswanath, A.; Schadler, L. S.; Benicewicz, B. C.; Siegel, R. W. Preparation and Optical Properties of Indium Tin Oxide/Epoxy Nanocomposites with Polyglycidyl Methacrylate Grafted Nanoparticles. *ACS Appl. Mater. Interfaces* **2011**, *3*, 3638–3645.

(32) Behling, R. E.; Kalluru, S. H.; Cochran, E. W. Morphological and Mechanical Behavior of Montmorillonite Grafted Block Copolymer Brushes. *J. Polym. Sci. Part B Polym. Phys.* **2016**, *54*, 353–361.

(33) Behling, R. E.; Wolf, L. M.; Cochran, E. W. Hierarchically Ordered Montmorillonite Block Copolymer Brushes. *Macromolecules* **2010**, *43*, 2111–2114.

(34) Ha, Y.; Kwon, Y.; Breiner, T.; Chan, E. P.; Tzianetopoulou, T.; Cohen, R. E.; Boyce, M. C.; Thomas, E. L. An Orientationally Ordered Hierarchical Exfoliated Clay−Block Copolymer Nanocomposite. *Macromolecules* **2005**, *38*, 5170–5179.

(35) Gam, S.; Meth, J. S.; Zane, S. G.; Chi, C.; Wood, B. A.; Seitz, M. E.; Winey, K. I.; Clarke, N.; Composto, R. J. Macromolecular Diffusion in a Crowded Polymer Nanocomposite. *Macromolecules* **2011**, *44*, 3494–3501.

(36) Vaia, R. A.; Giannelis, E. P. Lattice Model of Polymer Melt Intercalation in Organically-Modified Layered Silicates. *Macromolecules* **1997**, *30*, 7990–7999.

(37) Vaia, R. a; Giannelis, E. P. Polymer Melt Intercalation in Organically-Modified Layered Silicates: Model Predictions and Experiment. *Macromolecules* **1997**, *30*, 8000–8009.

(38) Zhou, Q.; Fan, X.; Xia, C.; Mays, J.; Advincula, R. Living Anionic Surface Initiated Polymerization (SIP) of Styrene from Clay Surfaces. *Chem. Mater.* **2001**, *13*, 2465–2467.

(39) Matyjaszewski, K.; Jakubowski, W.; Min, K.; Tang, W.; Huang, J.; Braunecker, W. A.; Tsarevsky, N. V. Diminishing Catalyst Concentration in Atom Transfer Radical Polymerization with Reducing Agents. *Proc. Natl. Acad. Sci.* **2006**, *103*, 15309–15314.

(40) Wang, J.; Matyjaszewski, K. Controlled/"living" radical Polymerization. Atom Transfer Radical Polymerization in the Presence of Transition-Metal Complexes. *J. Am. Chem. Soc.* **1995**, *117*, 5614–5615.

(41) Qin, S.; Matyjaszewski, K.; Xu, H.; Sheiko, S. S. Synthesis and Visualization of Densely Grafted Molecular Brushes with Crystallizable Poly(octadecyl Methacrylate) Block Segments. *Macromolecules* **2003**, *36*, 605–612.

(42) Jakubowski, W.; Min, K.; Matyjaszewski, K. Activators Regenerated by Electron Transfer for Atom Transfer Radical Polymerization of Styrene. *Macromolecules* **2006**, *39*, 39–45.

(43) Matyjaszewski, K.; Tsarevsky, N. V. Macromolecular Engineering by Atom Transfer Radical Polymerization. *J. Am. Chem. Soc.* **2014**, *136*, 6513–6533.

(44) Jakubowski, W.; Matyjaszewski, K. Activator Generated by Electron Transfer for Atom Transfer Radical Polymerization. *Macromolecules* **2005**, *38*, 4139–4146.

(45) Min, K.; Gao, H.; Matyjaszewski, K. Preparation of Homopolymers and Block Copolymers in Miniemulsion by ATRP Using Activators Generated by Electron Transfer (AGET). *J. Am. Chem. Soc.* **2005**, *127*, 3825–3830.

(46) Jakubowski, W.; Matyjaszewski, K. Activators Regenerated by Electron Transfer for Atom-Transfer Radical Polymerization of (Meth)acrylates and Related Block Copolymers. *Angew. Chemie - Int. Ed.* **2006**, *45*, 4482–4486.

(47) Chong, B. Y. K.; Le, T. P. T.; Moad, G.; Rizzardo, E.; Thang, S. H. A More Versatile Route to Block Copolymers and Other Polymers of Complex Architecture by Living Radical Polymerization: The RAFT Process. *Macromolecules* **1999**, *32*, 2071–2074.

(48) Chiefari, J.; Chong, Y. K. B.; Ercole, F.; Krstina, J.; Jeffery, J.; Le, T. P. T.; Mayadunne, R. T. A.; Meijs, G. F.; Moad, C. L.; Moad, G.; *et al.* Living Free-Radical Polymerization by Reversible Addition−Fragmentation Chain Transfer: The RAFT Process. *Macromolecules* **1998**, *31*, 5559–5562.

Chapter 2. Hierarchically Ordered Montmorillonite Semi-crystalline Block Copolymer Nanocomposites Prepared by Surface Initiated Polymerization

2.1 INTRODUCTION

2.1.1 Montmorillonite (MMT) clay as a filler in polymer nanocomposites

As one of the most commonly used nanofillers, MMT nanoclays have been extensively used in polymer matrices in order to enhance various material properties such as mechanical strength,[1] thermal stability,[2,3] barrier properties,[4,5] and flame retardancy.[6] Since these significant property enhancements directly result from strong interactions between MMT and polymer chains,[7] a good dispersion of the MMT into the host polymer matrix is critical for optimization of the aforementioned material properties. Among the various properties that can be improved by incorporating MMT clay platelets into polymer, gas barrier properties are of particular interest because gas barrier films can be used in a variety of industrial applications including food,[8–10] medicine,[11–13] electronics,[3,4] and others.[14] For example, Nielsen and co-workers have demonstrated that MMT fillers create tortuosity in the gas diffusion pathway, resulting in enhanced gas barrier properties compared to neat polymer without MMT.[15] However, the enhancement achieved from the incorporation of MMT is often limited by aggregation of the nanoclays due to their incompatibility with the polymer matrix.

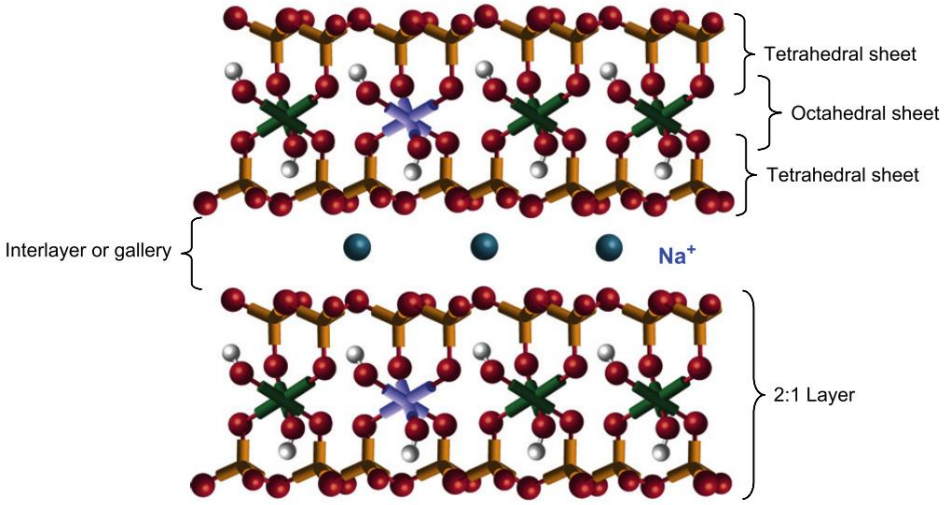

Figure 2.1: Structure of sodium MMT clay. Reproduced with permission from ref.[16] Copyright © 2008 Elsevier Ltd.

Previous studies on the structure of clays have revealed that a single MMT clay sheet is 1 nm thick with lateral dimension varied from 30 nm up to several microns. Each sheet is composed of layers of tetrahedral and octahedral crystalline structures at a ratio of 2:1 (**Figure 2.1**).[16] The central layer of the octahedral crystal lattice is composed of alumina or magnesia, which is sandwiched between two layers of silica tetrahedra. In their natural state, these clay sheets are stacked together due to van der Waals attraction, with a regular gap in between them which is referred to as the 'interlayer' or 'gallery' (**Figure 2.2a**). The substitution of Al^{3+} by Mg^{2+}, or in some cases Fe^{2+} and Li^{+}, in the central layer creates a cation deficiency which renders the surface of each clay sheet negatively charged. Therefore, earth-abundant alkali cations such as Na^{+} are distributed in the galleries as counterions. These Na^{+} ions can be ion exchanged with certain amphiphilic organic cations, which typically have an alkyl tail with an ammonium cation head.[17] Such surface modifications will transform the clay surface to be more hydrophobic, which promotes compatibilization with other organic materials. Surface modification treatments can also

expand the galleries a bit (e.g., several Angstroms to nanometers) and provide initiation sites on the clay surface for subsequent polymer grafting reactions (**Figure 2.2b**). Once the long chain polymers are grafted on the clay surface, in between the galleries, the initial stacked structure will be totally disrupted, and thereby exfoliation of clay sheets can be achieved (**Figure 2.2c**).[16]

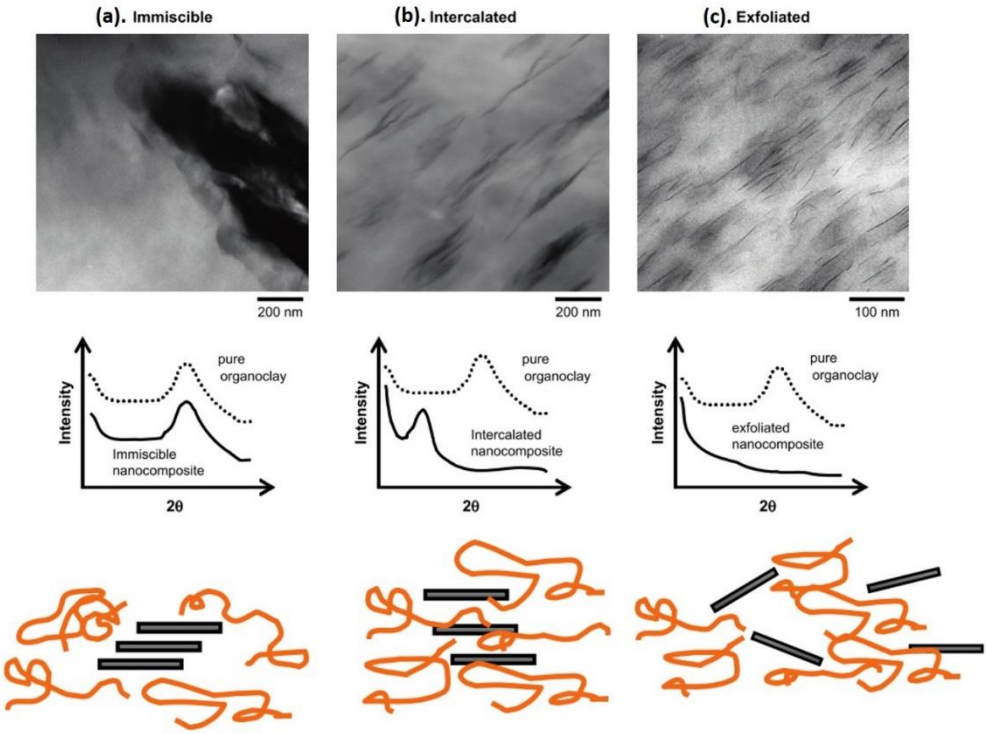

Figure 2.2: Illustration of different states of dispersion of organoclays in polymers with corresponding X-Ray Diffraction (XRD) and transmission electron microscopy (TEM) results. Reproduced with permission from ref.[16] Copyright © 2008 Elsevier Ltd.

Various techniques exist to disperse incompatible filler materials into polymer matrices as has been described in Chapter 1. Some of the most common methods include melt-blending,[18–20] solution intercalation,[21,22] and surface initiated polymerization (SIP).[23–

[28] SIP, in particular, is an attractive approach since anchoring of the newly grown chains on the filler surface is essentially guaranteed by the graft-from method.[25] As a result, a much higher content of exfoliated nanoclay, when compared to conventional melt blending approaches (usually < 5 wt%),[16] can be achieved without sacrificing the bulk properties of the polymer matrix (e.g. flexibility, optical transparency, etc.). The combination of SIP with careful selection of the tethering polymer chemistry is one technique to further enhance desired materials properties.

2.1.2 Semi-crystalline block copolymer (BCP) as a matrix material in nanocomposites

Semi-crystalline polymers have been broadly used as gas barrier films. The chain packing in crystalline domains is impermeable to small gas molecules.[29,30] Wang et al. previously reported a confined geometry in multilayer films can increase chain packing efficiency of semi-crystalline polyethylene oxide (PEO) compared to the bulk polymer. This results in significantly lower gas permeability (more than two orders of magnitude) with decreasing PEO layer thickness (several microns down to 20 nm). Since SIP yields densely grafted polymer chains on the filler surface, a polymer containing semi-crystalline segments grafted onto the MMT surface could produce enhanced chain packing efficiency of the semi-crystalline polymer as well. If a side chain crystalline polymer can be successfully anchored on the MMT surface, the resulting nanocomposites might possess densely packed crystalline domains in a parallel direction to the MMT, possibly further enhancing gas barrier properties.

Conventionally, most barrier materials contain several layers where each layer serves to inhibit rapid diffusion of a particular species (e.g., water, oxygen, chemical agents, etc.).[14] As a potential solution to reduce the production cost associated with multi-layer formation, we examined a BCP as a scaffold material due to its ability to

spontaneously self-assemble into nanoscale morphologies.[31,32] If each block in the BCP portion of the hybrid material were selected to serve as a nanoscale barrier layer, then the multi-step production process of making a multilayer barrier structure could be completely replaced with a single layer of this hybrid BCP material, leading to a significant reduction of production costs. Most importantly, the fact that the clay and BCP are an integrated subunit should render these materials not only melt and solution processable, but also recyclable.

2.1.3 Summary of work

For the clay nanocomposites produced in this study, we conducted SIP of BCPs directly from the clay surface using activators regenerated by electron transfer atom transfer radical polymerization (ARGET ATRP). This synthetic technique is highly versatile and allows for the controlled synthesis of a wide range of vinyl monomer-derived polymers.[33] It is also a robust process compared to other living polymerization processes because propagating radicals are less sensitive to impurities than ionic reactions. Additionally, the ARGET enhancement of traditional ATRP, in which significantly less catalyst species is required by addition of a reducing agent,[34] further eradicates sensitivity to impurities and allows for less contamination of the final product by catalyst.

In the following section, we present a synthetic strategy to produce poly(octadecyl acrylate)-block-polystyrene (PODA-b-PS) BCPs tethered to MMT surfaces using surface initiated ARGET ATRP. Poly(octadecyl acrylate) (PODA) is a side chain crystalline polymer with a crystal melting temperature around 50 °C. A rigid polystyrene (PS) block was chosen as a subsequent block to ensure the resulting BCP composites maintain their structural integrity. Also, the final composite samples are expected to exhibit thermoplastic elastomer like behavior within a certain temperature range, which could aid in the

composite material's processability and recyclability. By controlling synthesis parameters, the BCPs with targeted composition were successfully synthesized from the MMT surface. The resulting BCP tethered on the MMT surfaces exhibited a fivefold increase in effective clay loading without significant clay aggregation (especially when compared to processing by melt blending).[16] The films cast from the nanocomposite solution were optically transparent with 92 % transmittance to visible light through a 6.2 μm thick film sample. Moreover, due to the high grafting density of BCPs on the MMT platelet, the percent crystallinity of the BCP nanocomposite samples was increased up to 440 % when compared to non-tethered but otherwise identical BCPs. We believe this material can potentially be used as a recyclable, flexible, and optically transparent gas barrier film that would be useful for advanced barrier and packaging purposes.

2.2 Synthesis, Characterization and Properties of Surface Grafted MMT-BCP Nanocomposites

2.2.1 Surface initiated synthesis of PODA-b-PS BCP from MMT clay

BCPs were synthesized via surface-initiated polymerization (SIP) from MMT platelets by adapting established ARGET ATRP methods (**Figure 2.3**).[25,26] First, sodium MMT was ion exchanged with a long alkyl chain surfactant that contained an initiator moiety for ARGET ATRP. The initiator-functionalized MMT (MMT-SI) thus served as the initiator for ARGET ATRP of PODA. After polymerization of the PODA block, ARGET ATRP of styrene was conducted from the MMT-PODA macroinitiator. The resulting BCP composite material (MMT-PODA-PS) was purified by precipitation in methanol.

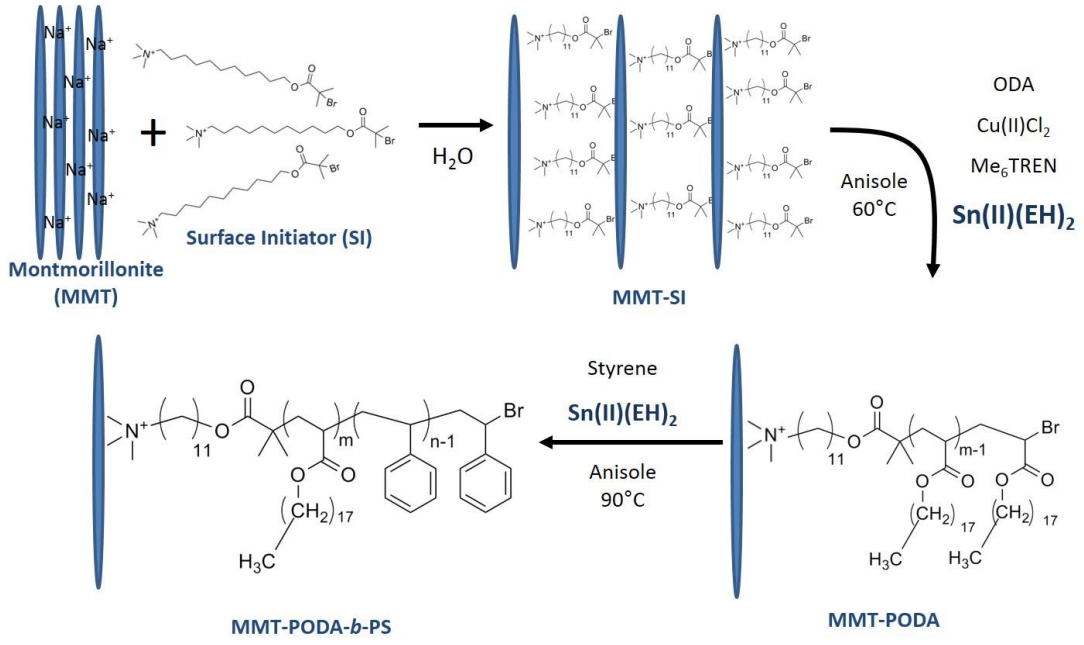

Figure 2.3: ARGET ATRP of PODA-b-PS BCPs from the surface of MMT clay.

The polymers synthesized from the surface of MMT were characterized by gel permeation chromatography (GPC) after ion exchange to cleave the polymer chains from the clay particles. Then the polymer underwent a transesterification procedure with octadecanol to remove the charged end groups without disrupting the octadecyl acrylate side chain structure. This step eliminated interactions between the charged end groups and the GPC columns, enabling accurate characterization of the molecular weight of prepared samples. **Table 2.1** summarizes the compositions of all synthesized BCP nanocomposites as well as the molecular weight and polydispersity of the corresponding building blocks. As are shown in **Table 2.1**, the M_n of PODA measured by GPC matches well with the theoretical M_n calculated based on monomer conversion, a good indication of the 'living' polymerization process of the first block of PODA from the clay surface. The 'livingness' of the bromide end group of MMT-PODA macroinitiators was confirmed by the

subsequent grafting of PS block with controlled molecular weight and low PDI. A uniform horizontal shift of refractive index (RI) signal toward a lower elution volume in the GPC chromatogram as shown in **Figure 2.4a** is consistent with uniform growth of the PS chains from the MMT-PODA macroinitiators. Representative samples in **Table 2.1** were all targeted with a ~50 vol% of each block, with the purpose of potentially forming a lamellar structure of the BCP matrix.

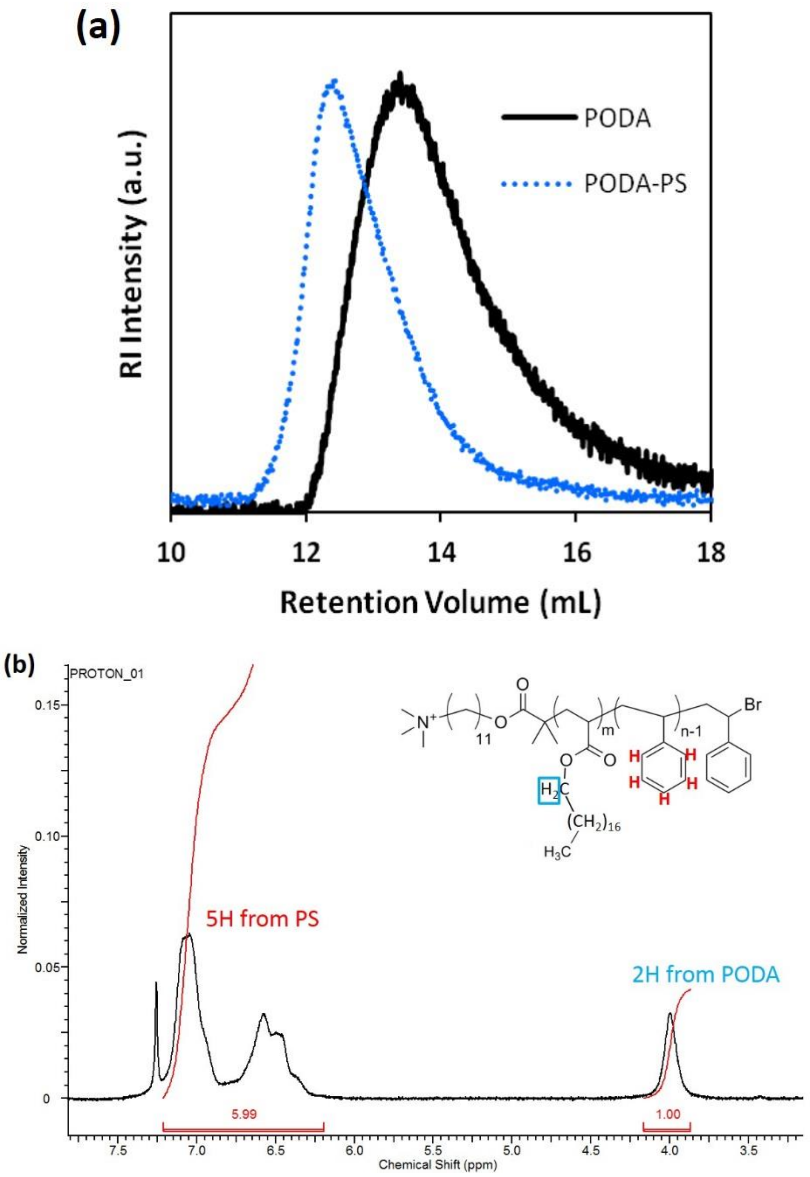

Figure 2.4: (a) GPC chromatograms of BCP after ion exchange and transesterification of MMT-PODA$_{67}$ and MMT-PODA$_{67}$-PS$_{54}$ where the subscripts indicate the number average molecular weight (M_n) of the components in kDa. (b) Proton NMR of BCP after ion exchange of MMT-PODA$_{67}$-PS$_{54}$.

Table 2.1: Composition of MMT-PODA-PS nanocomposites

Sample	MMT-PODA, M_n (kDa)[a]	MMT-PODA, $M_{n,theo}$ (kDa)[b]	MMT-PODA, PDI[a]	MMT-PODA-PS, M_n (kDa)[c]	MMT-PODA-PS, PDI[a]	Vol% of PS, f_{PS} (%)[d]
MMT-$PODA_{16}$-PS_{20}	15.7	12.2	1.26	35.7	1.18	56
MMT-$PODA_{23}$-PS_{17}	22.8	23.9	1.15	39.7	1.15	43
MMT-$PODA_{46}$-PS_{45}	46.3	44.4	1.23	85.0	1.32	46
MMT-$PODA_{67}$-PS_{54}	66.9	68.8	1.31	121	1.17	42

a. Number averaged molecular weight (M_n) determined by tetrahydrofuran (THF) GPC after ion-exchange with LiBr and transestirification with octadecanol. A dn/dc of 0.06257 (mL/g) in THF was determined experimentally by plotting the integrated refractive index signal for the PODA homopolymer peak for various sample concentrations and extracting the slope. The dn/dc value was used to molecular weight calculation of the PODA block.

b. The theoretical molecular weight $M_{n,\ theo}$ was calculated as $M_{n,\ theo}$ (g/mol) = [Monomer] /[Initiator]*(conversion%)*324.54 where the percentage monomer conversion was calculated from the ethylene double bond conversion of octadecyl acrylate by ^{1}H NMR.

c. M_n of the PS block was determined by ^{1}H NMR (**Figure 2.4b**) and Mn of MMT-PODA-PS was calculated.

d. Volume percentage of PS was calculated using a density of 0.985 g/cm^3 for PODA[29] and 1.040 g/cm^3 for PS.

Thermal transitions of the synthesized BCP nanocomposites were characterized by differential scanning calorimetry (DSC) and the corresponding thermograms are shown in **Figure 2.5**. Two distinct thermal transitions were detected for all samples. The thermal transitions correlated well with established literature values for PODA[35] and PS[36] homopolymers. The endothermic peak ca. 53 °C represents the melting transition (T_m) of the PODA side chain crystals while the second thermal transition around 108 °C is attributed to the glass transition temperature (T_g) of the PS block. These two separate

transitions appearing near the expected values of their pure homopolymer analogs suggest that BCP micro-phase segregation occurred for all prepared samples. The T_g of PODA was estimated to be close to -111 °C.[37] But it was not observed by DSC, possibly due to crystalline side chain immobilization of the backbone making the T_g relatively weak or the fact that this transition temperature was too close to the lower temperature limit of the DSC instrumentation. The T_g of the PS block was similar to the accepted value for PS homopolymer, which implies the segmental mobility of the PS block was not significantly altered by the surface grafting.[38] Based on the DSC thermograms, the BCP composites would be expected to be rigid solids at temperatures below 53 °C and thermoplastic elastomer-like materials between 53 °C and 108 °C because the rigid MMT and PS domains are interconnected by liquid PODA chains. At temperatures above 108 °C, they are expected to be melts or liquids (i.e., melt processable).

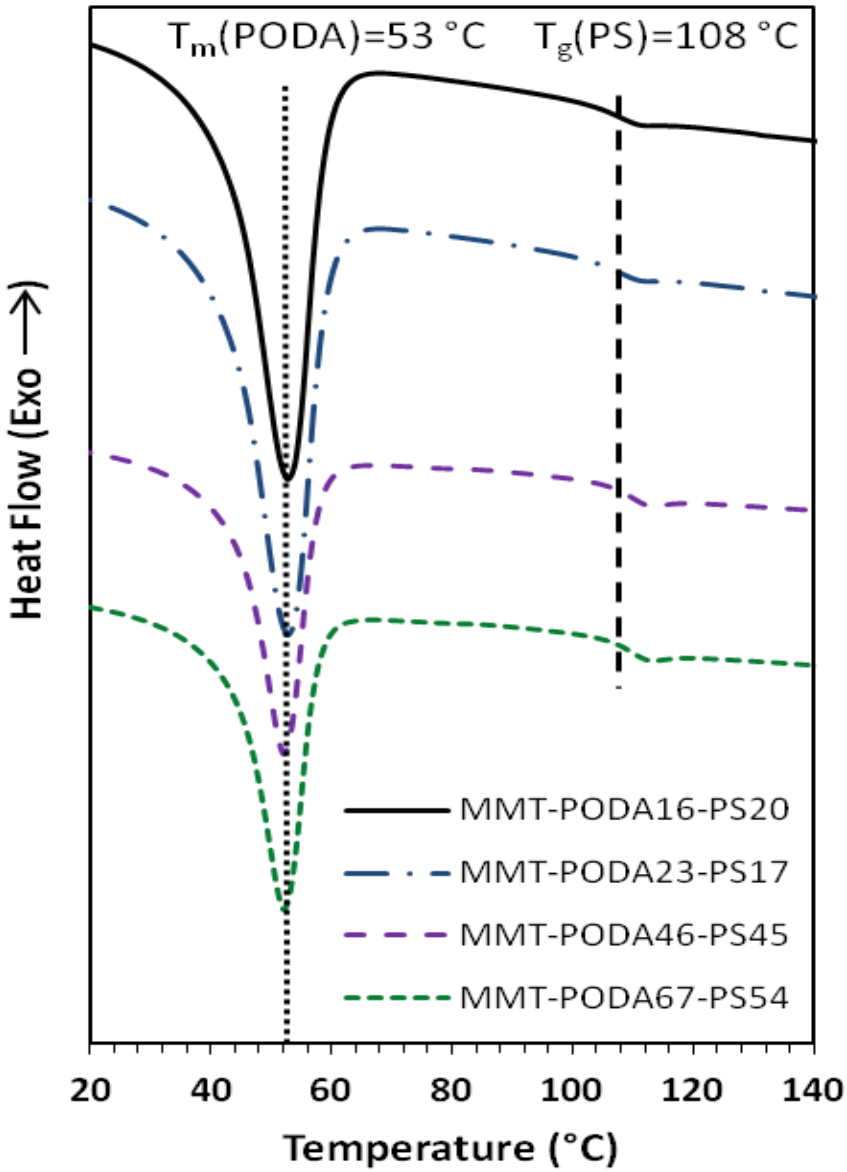

Figure 2.5: DSC thermograms of nanocomposites collected during second heating at a heating rate of 20 °C/min.

2.2.2 Clay content and dispersion

Because the degree of exfoliation (i.e., in this case, exfoliation means disruption of the natural stacked clay structure such that MMT is dispersed, ideally, as isolated platelets uniformly in the matrix) is often correlated to property enhancement in nanocomposite materials, XRD was conducted to discern the degree of the exfoliation of the MMT after the synthesis. **Figure 2.6** shows the results of XRD measurements on samples at various synthetic stages. Natural MMT with sodium counterions has a well-characterized inter-gallery spacing (d-spacing) of 12.2 Å, which then increased to 18.5 Å upon addition of the surface initiator, denoting that the surface initiator displaced the existing sodium cations. After the PODA block was grafted onto the MMT platelets, the absence of a characteristic diffraction peak suggests the exfoliation of the MMT particles.

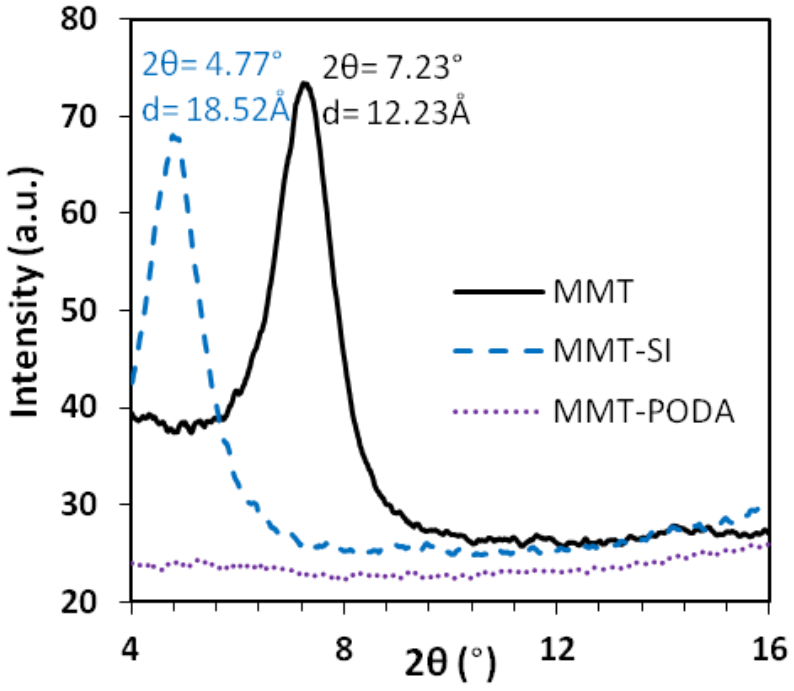

Figure 2.6: XRD profile with indicated scattering peaks and corresponding d-spacing.

To further characterize the degree of exfoliation, representative TEM images of thin sections of the MMT-PODA-PS nanocomposite samples prepared by cryomicrotome are shown in **Figure 2.7**. Individual platelets appear as very faint streaks or dots in the image. At low magnification, **Figure 2.7a** suggests the dispersion of the MMT platelets is uniform with only a few small MMT aggregates (dark spots) indicating an overall good dispersion. As shown in **Figure 2.7b**, a higher magnification image of the identical sample revealed many fully exfoliated single clay sheets along with a few doublets, triplets, etc. Combining TEM with XRD, one can conclude that the MMT is well-dispersed in the polymer, as expected for an in-situ polymerized system.

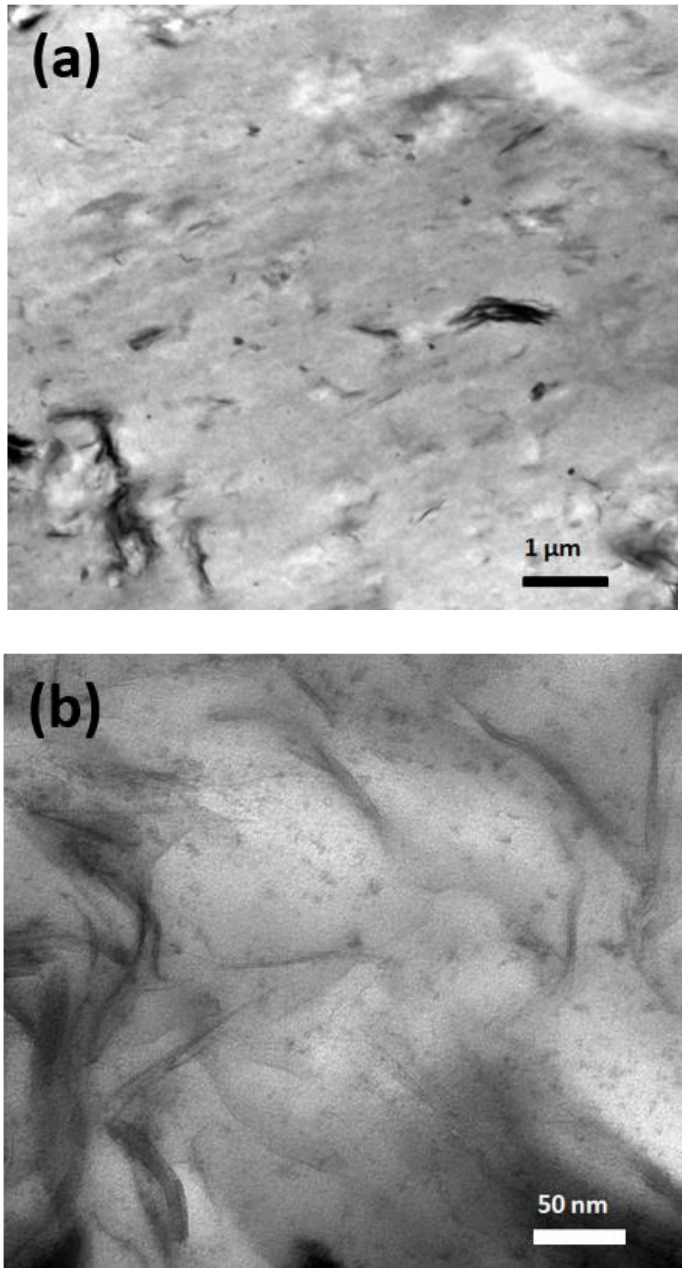

Figure 2.7: TEM images of MMT-PODA$_{16}$-PS$_{20}$ microtomed sections at low (a) and high (b) magnifications. Total clay content is 12 wt% (6.4 vol%) for this sample.

In order to induce micro-phase segregation of the BCP attached to the MMT, the bulk nanocomposite samples were thermally annealed at 170 °C for 2 - 4 days in vacuum.

Subsequently, the annealed samples were microtomed into thin sections of ca. 70 nm thickness and deposited onto TEM grids. **Figure 2.8** shows a representative morphology of the BCP domains in the nanocomposite sample (MMT-PODA$_{67}$-PS$_{54}$). The BCP exhibited a high degree of phase segregation with good contrast between the two polymer blocks without additional staining. This could be due to the presence of MMT which enhanced the contrast between the PODA block that encapsulates the adjacent MMT and the PS block, allowing for direct imaging of the domains without staining. We attributed the darker regions to the PODA domains because of their crystallinity and MMT content. Image analysis of the TEM micrographs revealed the ratio between dark and bright areas was ~ 1.3. Considering the volume fraction of clay sheets in this sample is 2.9 %, the ratio of dark area contributed by PODA to the bright area from PS is therefore ~1.2, which is consistent with the volume ratio of the corresponding blocks in the sample (i.e. PODA to PS). The morphology resembled the 'corona' morphology, which had been previously observed for MMT-PS-b-poly(tert-butyl acrylate)[39] specimens with a similar block volume ratio.

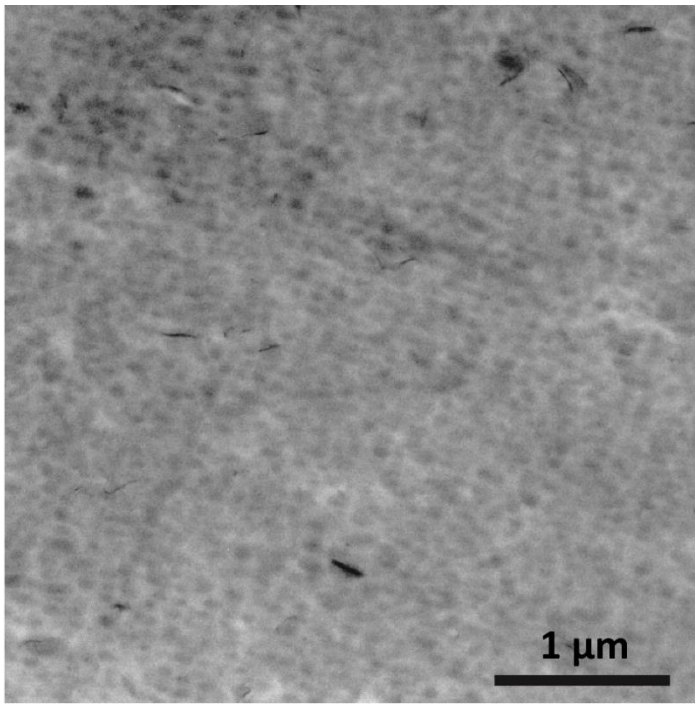

Figure 2.8: TEM image of MMT-PODA$_{67}$-PS$_{54}$ microtomed section.

The synthesized MMT-PODA-PS nanocomposite samples were examined in thermogravimetric analysis (TGA) under N_2 atmosphere up to 800 °C. As is shown in **Figure 2.9**, besides the initial evaporation of water, the degradation of organic components within pristine MMT up to 600 °C is about 5.5 wt%. After grafting of the surface initiator, the modified clays are found to have 28.9 wt% of volatile degradable components. And it can be calculated that about 24.8 wt% of the MMT-SI is composed of the alkyl ammonium surface initiator, corresponding to 94.8% of Na^+ ion being exchanged on the MMT clay surface, calculated from the MMT clay ion exchange capacity of 92 milliequivalent/100g.[40] The calculation steps are listed below.

X - non-volatile clay component
Y - volatile clay component
Z - surface initiator

From TGA results: $\frac{y}{x+y} = 5.5\ \%$ and $\frac{y+z}{x+y+z} = 28.9\ \%$

The SI content in MMT-SI (wt%) is: $\frac{z}{x+y+z} = 24.8\%$

For 100g neat MMT clay, mass of SI is: $\frac{y+z}{x+y+z} = \frac{24.8g*100g}{(100-24.8)g} = 33.0g$

Mw(SI) = 379.4 g/mol, for 100g neat MMT clay, moles of SI is: $\frac{33.0g}{379.4g/mol} = 0.0872\ mol = 87.2 mmol$

Percent Na^+ exchanged: $\frac{87.2(\frac{mmol}{100g})}{92(\frac{mmol}{100g})} * 100\% = 94.8\ \%$

Assuming 100% initiator activity, the grafting density is: $\frac{0.0872\ mol * 6.02 * 10^{23}\ chains/mol}{600\ m^2/g * 100\ g * 10^{18}\ nm^2/m^2} = 0.87\ chain/nm^2$

To determine the initiator efficiency of the SIP, we compared the molecular weight obtained from GPC results with the theoretical molecular weight calculated based on monomer conversion and the assumption of 100% initiator activity. They match well as is demonstrated in **Table 2.1**. This validates the assumption of ~100% initiator activity, which was also proved by the previous work by Behling et al. on MMT-PS grafting reactions.[41] The grafting density was therefore calculated as 0.87 chain/nm^2 which was based on the estimated specific surface area of MMT of ca. 600 m^2/g.[42] Compared to the previous densely grafted polymer brush systems, where 16 kDa PS were grafted on planar gold surface with a grafting density of 0.31 chain/nm^2,[43] where the poly(methyl methacrylate) (PMMA) chains on silica wafer at 0.7 chain/nm^2,[44] and where a surface initiated ATRP of PS reaching 1 chain/nm^2,[41] the grafting density of PODA-PS chains on

the clay surface in this work is high enough to be in the dense brush regime. Considering the bulky side chains of the PODA segment in particular, the PODA-PS chains form a highly stretched brush on the clay surfaces. This high grafting density is attributed to the surface initiated polymerization and a minimized steric hindrance during the grafting process.[41]

The clay content of each sample was determined based on the residual weight of the silicate components of the MMT clay (**Table 2.2**). The clay content in the bulk nanocomposite samples ranged from 5 to 12 percent by weight. Note that the polymer chains were grafted from the clay surface meaning that the clay inclusion in the PODA block in particular reached as high as 27 wt%. This further demonstrates the capability of the SIP synthetic route to obtain a high contents of filler material in a polymer matrix. Considering the high degree of clay exfoliation mentioned in the previous section, this SIP procedure clearly demonstrates its advantages in maximizing the interaction of the inorganic filler and the polymeric matrix in an exfoliated state compared to traditional melt blending methods which, in most cases, produce nanocomposites with exfoliated filler material only when inorganic content is below 10 wt%.[45–47]

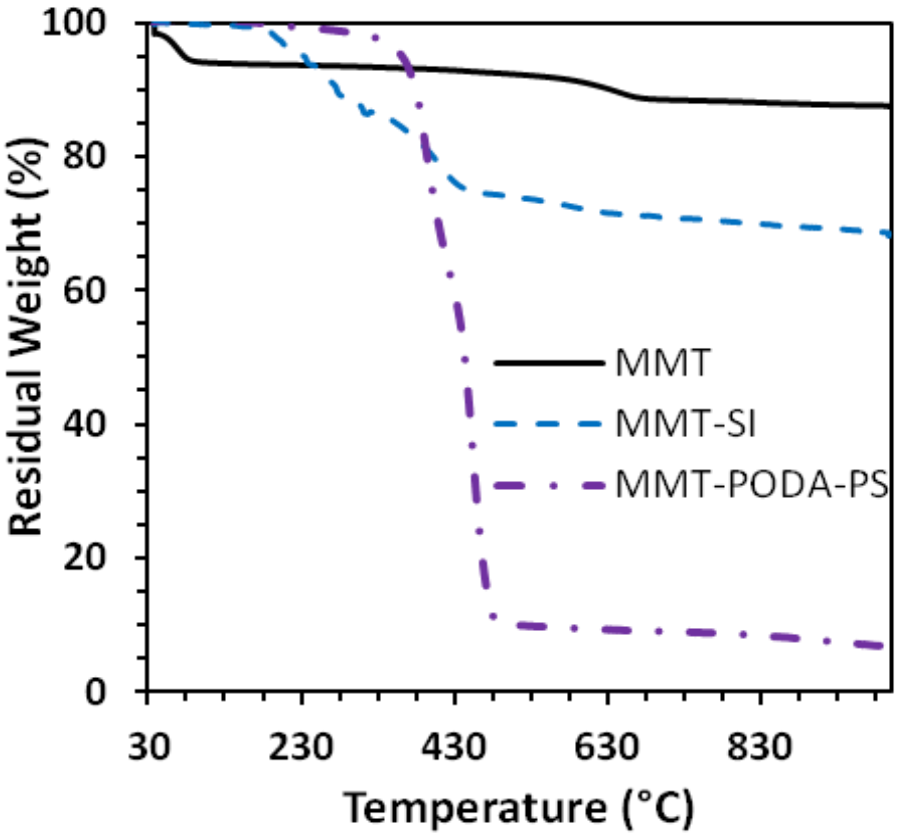

Figure 2.9: Representative TGA profile with a heating rate of 10 °C/min in N_2 showing decomposition of organic components.

Table 2.2: Clay content in MMT-PODA-PS BCP nanocomposites

MMT-PODA-PS Sample	Total Mw (kDa)	Clay Weight Percent (%)	Clay Weight Percent in MMT-PODA (%)
MMT-$PODA_{16}$-PS_{20}	35.7	12	27
MMT-$PODA_{23}$-PS_{17}	39.7	9.1	16
MMT-$PODA_{46}$-PS_{45}	85.0	8.6	16
MMT-$PODA_{67}$-PS_{54}	121	5.7	10

2.2.3 Crystallinity and optical properties of the BCP nanocomposite films

To evaluate whether the high grafting density of the BCPs on the MMT surface enhanced crystallinity of the PODA block, non-isothermal crystallization experiments were performed with DSC. The crystallinity of the anchored BCP chains on the MMT clay surface was compared with those of non-anchored BCP analogs. For this comparison, the polymer chains were cleaved from the surface of MMT via ion exchange with excess salt to produce non-anchored BCP samples with crystalline PODA blocks. The fraction of crystallinity in the PODA block, x_c, was calculated from Eq. (1), where ΔH_f is the enthalpy of fusion of the sample measured by DSC and ΔH_{f0} is the enthalpy of fusion of the perfect PODA crystal. The value of ΔH_{f0} for PODA is 220.0 J/g.[48]

$$x_c = \left(\frac{\Delta H_f}{\Delta H_{f0}}\right) \qquad (1)$$

The estimated percent crystallinity for all samples are listed in **Table 2.3**. For all samples, percent crystallinity was increased at least 300 %. We strongly believe this crystallinity enhancement was caused by the high grafting density of the BCPs on the clay surface which partially stretched/elongated the chains. Here, the crystalline side chains of the PODA block are geometrically confined by being anchored to MMT at the chain end, yet the side chains are pre-organized due to the stretched polymer backbone enhancing the crystalline chain packing compared to non-anchored PODA. **Figure 2.10** illustrates a conceptual comparison of this BCP morphology. In the anchored BCP, the side chains are forced to grow closer to the neighboring chains as is shown in **Figure 2.10b** than they would in their non-anchored state, **Figure 2.10a**. It is observed that the improvement in percent crystallinity increases with molecular weight of PODA block in the system of MMT-PODA-PS. Without more information about the exact microstructure of the BCP, however, it is difficult to rationalize the trend. MMT-PODA was also examined after the

polymerization of the first block, which showed mostly comparable but slightly higher values for 3 of the samples compared to MMT-PODA-PS. MMT-PODA and MMT-PODA-PS have the same high grafting density, causing the PODA segments near the clay surfaces to be stretched to a comparable extent, which contributes to the increased crystallinity in both cases compared to neat PODA-PS BCP. However, the PODA segments in MMT-PODA-PS are restricted at both ends, leading to a loss in segmental mobility and less ability for PODA segments to rearrange as they incorporate into the crystal.

Table 2.3: Comparison of crystallinity in the PODA block

Nanocomposite Sample	**Crystallinity in PODA block (%)**			**% Crystallinity Increase (MMT-PODA-PS vs. neat PODA-PS)**
	PODA-PS	MMT-PODA	MMT-PODA-PS	
MMT-PODA$_{16}$-PS$_{20}$	7.71	41.5	32.8	325
MMT-PODA$_{23}$-PS$_{17}$	6.38	41.6	31.0	386
MMT-PODA$_{46}$-PS$_{45}$	7.34	38.7	36.0	390
MMT-PODA$_{67}$-PS$_{54}$	8.50	36.3	46.2	444

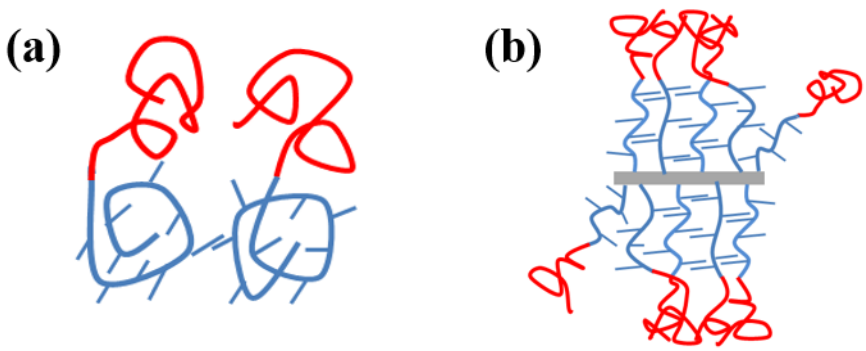

Figure 2.10: Illustration of the structures of (a) free BCP chains and (b) densely grafted BCP chains.

As optical transparency is a distinctive advantage of many polymeric films, when a nanocomposite material is formed, achieving a good dispersion of nanofillers in bulk nanocomposites is always crucial for retaining good optical properties of the bulk material. In order to examine optical properties of nanocomposite films with the dispersion of MMT clay sheets in the PODA-PS BCP matrix, the visible light transmittance was collected with UV-Vis spectroscopy for MMT-$PODA_{16}$-PS_{20} nanocomposite films, which corresponds to the specimen with the highest clay content (27 wt%). Nanocomposite films were solution cast onto a quartz plate out of toluene. All films with thicknesses up to 6.2 μm exhibited a high transmittance (> 92 %) across the entire visible light range (390 nm-700 nm). **Figure 2.11** shows the average light transmittance to visible light as a function of film thickness. The high optical clarity is also strong supporting evidence that the MMT is well dispersed since the MMT aggregates would significantly scatter light. The thickest film (6.2 μm) has an average transmittance of 92.3% across the entire visible light spectrum, which is nearly 20 % higher than previously reported nanocomposite films made by solution intercalation.[4,49] From an application perspective, the desirable optical transparency renders these materials potential candidates for transparent coatings, or clear packaging materials.

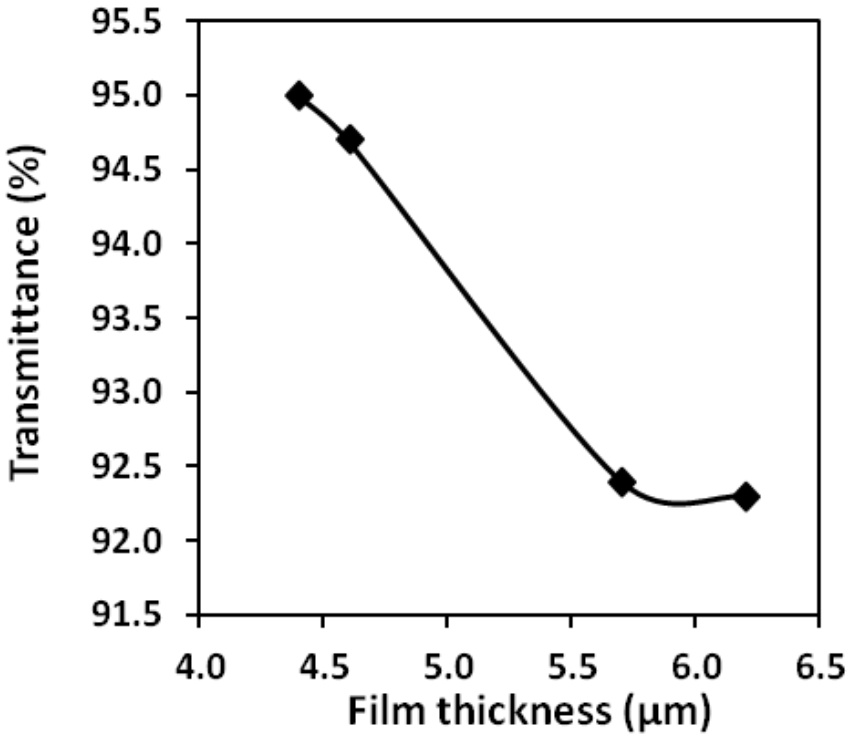

Figure 2.11: Average visible light transmission as a function of film thickness measured on fused quartz slides. Films were solution cast onto quartz slides out of toluene and thicknesses of specific spots were measured by profilometry.

2.3 EXPERIMENTAL

2.3.1 Materials

MMT clay was generously provided by Southern Clay Products Inc. All the reagents were purchased from Sigma-Aldrich and used as received unless otherwise noted. Octadecyl acrylate monomer (100mL) (melting point = 32 °C) was purified with aluminum oxide (0.5g) and calcium hydride (0.5g) at 40 °C under agitation for 1 hour to remove all the inhibitor and residual water in the monomer. Styrene monomer (Sigma Aldrich, 99%) (100mL) was purified with a mixture of calcium hydride (0.5g) and aluminum oxide (0.5g) at room temperature for 1 hour. Anisole (Sigma Aldrich, 99%) was also purified with a

mixture of calcium hydride (0.5g) and aluminum oxide (0.5g) at room temperature for 1 hour. All of the solutions were filtered to remove the solid purification agent particles prior to polymerization. Copper(II) chloride, Tin(II) 2-ethylhexanoate ($Sn(EH)_2$), Tris[2-(dimethylamino)ethyl]amine (Me_6TREN) (Fisher) were used as received.

2.3.2 MMT surface modification

The surface initiator, 11'-(N,N,N-trimethylammonium bromide)-undecyl-2-bromo-2-methyl propionate, was synthesized according to a previous procedure[50]. MMT (2.5 g) was dispersed in 800 mL of deionized water and sonicated using a 400W probe sonicator (Branson, Digital Sonifier 450) at 20% amplitude for 30 min. Surface initiator (1 g) was then dissolved in 100 mL of deionized water and the solution was slowly added into the MMT dispersion. The mixture was vigorously stirred for 48 hours. The suspension was filtered and washed with copious amounts of DI water to remove unattached surface initiators. The solids were filtered and dried under vacuum to obtain a dry free-flowing powder of MMT-SI.

2.3.3 Polymerization of octadecyl acrylate monomer to form PODA attached to the MMT clay surface

ARGET ATRP was used to polymerize the octadecyl acrylate monomer to form the PODA block attached to the MMT surface. MMT-SI, $CuCl_2$, Me_6TREN, and $Sn(EH)_2$ were added at molar ratios of 1 : 0.1 : 1 : 2. The molar feed ratio of octadecyl acrylate relative to surface initiator was controlled to target different molecular weights while the monomer conversions were kept around 30 % in all reactions. The polymerization was conducted at 60 °C with 50 wt% of anisole as the reaction solvent. MMT-SI, octadecyl acrylate, $CuCl_2$, Me_6TREN and anisole were added into a round bottom flask. The reducing agent $Sn(EH)_2$ was measured in a separate Erlenmeyer flask. Both flasks were purged with

dried argon at room temperature for at least 30 min to remove the oxygen. A luer lock syringe with a needle attached was purged with argon for 5 min and used to transfer the reducing agent to the round bottom flask. The flask was immediately placed in an oil bath at 60 °C and reacted for 0.5 to 2 hrs. The polymerization was terminated by placing the flask into liquid nitrogen followed by exposing the reaction mixture to air. The product MMT-PODA was purified by first diluting with THF and then precipitating in acetone.

2.3.4 Polymerization of the styrene block from the MMT-PODA macro-initiator

The subsequent polymerization of the styrene block was performed similarly using ARGET ATRP. As a representative example, the molar ratios of styrene, MMT-PODA as the macroinitiator, $CuCl_2$, Me_6TREN, $Sn(EH)_2$ were 375 : 1 : 0.188 : 1.88 : 3.76. For different samples, the monomer to macroinitiator ratios were adjusted according to targeted molecular weights of the PS block. The polymerization was run at 90 °C for 48 hours with 40 wt% anisole as reaction solvent.

2.3.5 Cleavage of polymer chains from clay surface and removal of charged end groups for GPC characterization

MMT-PODA was ion exchanged with LiBr salt in THF for 2 hours. The solution was centrifuged and the supernatant was collected in order to recover polymer chains cleaved from the clay. Dried polymer products (160 mg) were dissolved in 7 mL THF with 200 mg of octadecanol. The solution was refluxed at 100 °C. Sulfuric acid (approx. 20 drops) was slowly added to the solution and the subsequent transestirification reaction was allowed to continue at 100 °C for 7 days. The resulting solution was precipitated with ethanol, centrifuged, collected and finally dried in a vacuum oven.

2.3.6 Characterization

2.3.6.1 Gel permeation chromatography (GPC)

GPC was used to obtain the polymer molecular weights and polydispersity indicies, using a Viscotek GPCMax VE 2001 GPC solvent/sample module with a Viscotek model 270 Dual Detector viscometer/light scattering detector, Viscotek VE 3580 refractive index detector with two Viscotek I-Series Mixed Bed Low MW Columns. THF was used as the eluent and the flowrate was 1.0 mL/min.

2.3.6.2 Proton nuclear magnetic resonance (^{1}H NMR)

NMR spectra were recorded on a Varian 400 MHz DirectDrive NMR with SMS sample changer to determine the conversion of ODA monomer after the synthesis of the PODA block, and the ratio of PS to PODA in the BCP after synthesis of the PS block. Specifically, the octadecyl acrylate block has characteristic peaks at 3.70 - 4.20 ppm (2 protons in the PODA side chain adjacent to the ester group) and the styrene block has characteristic peaks at 6.18 - 7.21 ppm (5 aromatic protons).

2.3.6.3 X-ray diffraction (XRD)

XRD was performed on a Rigaku R-Axis Spider diffractometer with an image plate detector using Cu K_α radiation (λ = 1.54 Å) and a graphite monochromator. XRD samples were prepared by mixing a small amount of sample with a droplet of mineral oil and mounting on a cryoloop.

2.3.6.4 Thermogravimetric analysis (TGA)

Thermal decomposition behavior of the copolymers was investigated using a thermogravimetric analyzer (DSC/TGA 1, Mettler Toledo). Samples were heated from 25 °C to 1000 °C at 10 °C/min under nitrogen atmosphere.

2.3.6.5 Differential scanning calorimetry (DSC)

Samples were heated and scanned under a continuous nitrogen purge (50 mL/min) at 20 °C/min within the temperature range of 0 -150 °C using a Mettler Toledo DSC 1. The T_g for each sample was taken as the midpoint step increment in the specific heat of the second heating cycle. The crystallinity of PODA was calculated based on the enthalpy of fusion (ΔH_{f0}) for PODA of 220.0 J/g.[48]

2.3.6.6 Microtome and transmission electron microscopy (TEM)

Ultra-thin sections of ~60-70 nm were cut cryogenically from annealed bulk nanocomposite samples with a diamond knife at - 60 °C using an RMC PowerTome XL ultramicrotome. TEM images were acquired on a FEI Tecnai Spirit Bio Twin operated at 80 kV.

2.3.6.7 UV–vis spectroscopy

Visible light transmission of nanocomposite films was measured using a Thermo Scientific Evolution 220 UV-Visible Spectrophotometer. Films were solution cast on quartz slides out of toluene and thicknesses of specific spots were measured by profilometry to report thickness corrected transmission values.

2.4 REFERENCES

(1) LeBaron, P.; Wang, Z.; Pinnavaia, T. Polymer-Layered Silicate Nanocomposites: An Overview. *Appl. Clay Sci.* **1999**, *15*, 11–29.

(2) Yoon, P. J.; Fornes, T. D.; Paul, D. R. Thermal Expansion Behavior of Nylon 6 Nanocomposites. *Polymer (Guildf).* **2002**, *43*, 6727–6741.

(3) Ebina, T.; Mizukami, F. Flexible Transparent Clay Films with Heat-Resistant and High Gas-Barrier Properties. *Adv. Mater.* **2007**, *19*, 2450–2453.

(4) Grunlan, J. C.; Grigorian, A.; Hamilton, C. B.; Mehrabi, A. R. Effect of Clay Concentration on the Oxygen Permeability and Optical Properties of a Modified Poly(vinyl Alcohol). *J. Appl. Polym. Sci.* **2004**, *93*, 1102–1109.

(5) Priolo, M. a.; Gamboa, D.; Holder, K. M.; Grunlan, J. C. Super Gas Barrier of Transparent Polymer-Clay Multilayer Ultrathin Films. *Nano Lett.* **2010**, *10*, 4970–4974.

(6) Bartholmai, M.; Schartel, B. Layered Silicate Polymer Nanocomposites: New Approach or Illusion for Fire Retardancy? Investigations of the Potentials and the Tasks Using a Model System. *Polym. Adv. Technol.* **2004**, *15*, 355–364.

(7) Bréchet, Y.; Cavaillé, J.-Y.; Chabert, E.; Chazeau, L.; Dendievel, R.; Flandin, L.; Gauthier, C. Polymer Based Nanocomposites: Effect of Filler-Filler and Filler-Matrix Interactions. *Adv. Eng. Mater.* **2001**, *3*, 571.

(8) Jagadish, R. S.; Raj, B.; Asha, M. R. Blending of Low-Density Polyethylene with Vanillin for Improved Barrier and Aroma-Releasing Properties in Food Packaging. *J. Appl. Polym. Sci.* **2009**, *113*, 3732–3741.

(9) Dong, T.; Yun, X.; Li, M.; Sun, W.; Duan, Y.; Jin, Y. Biodegradable High Oxygen Barrier Membrane for Chilled Meat Packaging. *J. Appl. Polym. Sci.* **2015**, *132*, 41871.

(10) Duncan, T. V. Applications of Nanotechnology in Food Packaging and Food Safety: Barrier Materials, Antimicrobials and Sensors. *J. Colloid Interface Sci.* **2011**, *363*, 1–24.

(11) Di, L.; Kerns, E. H.; Fan, K.; McConnell, O. J.; Carter, G. T. High Throughput Artificial Membrane Permeability Assay for Blood–brain Barrier. *Eur. J. Med. Chem.* **2003**, *38*, 223–232.

(12) Reichel, A.; Begley, D. J. Potential of Immobilized Artificial Membranes for Predicting Drug Penetration Across the Blood-Brain Barrier. *Pharm. Res.* **1998**, *15*, 1270–1274.

(13) Chatham, H. Oxygen Diffusion Barrier Properties of Transparent Oxide Coatings on Polymeric Substrates. *Surf. Coatings Technol.* **1996**, *78*, 1–9.

(14) Lange, J.; Wyser, Y. Recent Innovations in Barrier Technologies for Plastic Packaging?a Review. *Packag. Technol. Sci.* **2003**, *16*, 149–158.

(15) Nielsen, L. E. Models for the Permeability of Filled Polymer Systems. *J. Macromol. Sci. Part A - Chem.* **1967**, *1*, 929–942.

(16) Paul, D. R.; Robeson, L. M. Polymer Nanotechnology: Nanocomposites. *Polymer (Guildf).* **2008**, *49*, 3187–3204.

(17) Giannelis, E. P.; Krishnamoorti, R.; Manias, E. Polymer-Silicate Nanocomposites: Model Systems for Confined Polymers and Polymer Brushes. In *ADVANCES IN POLYMER SCIENCE*; 1999; Vol. 138, pp. 107–147.

(18) Vaia, R. A.; Teukolsky, R. K.; Giannelis, E. P. Interlayer Structure and Molecular Environment of Alkylammonium Layered Silicates. *Chem. Mater.* **1994**, *6*, 1017–1022.

(19) Heinz, H.; Vaia, R. a; Farmer, B. L. Interaction Energy and Surface Reconstruction between Sheets of Layered Silicates. *J. Chem. Phys.* **2006**, *124*, 224713.

(20) Giannelis, E. P. Polymer Layered Silicate Nanocomposites. *Adv. Mater.* **1996**, *8*, 29–35.

(21) Sinha Ray, S.; Okamoto, M. Polymer/layered Silicate Nanocomposites: A Review from Preparation to Processing. *Prog. Polym. Sci.* **2003**, *28*, 1539–1641.

(22) Hussain, F. Review Article: Polymer-Matrix Nanocomposites, Processing, Manufacturing, and Application: An Overview. *J. Compos. Mater.* **2006**, *40*, 1511–1575.

(23) Biasci, L.; Aglietto, M.; Ruggeri, G.; Ciardelli, F. Functionalization of Montmorillonite by Methyl Methacrylate Polymers Containing Side-Chain Ammonium Cations. *Polymer (Guildf).* **1994**, *35*, 3296–3304.

(24) Huang, X.; Lewis, S.; Brittain, W. J.; Vaia, R. A. Synthesis of Polycarbonate-Layered Silicate Nanocomposites via Cyclic Oligomers. *Macromolecules* **2000**, *33*, 2000–2004.

(25) Kalluru, S. H.; Cochran, E. W. Synthesis of Polyolefin/Layered Silicate Nanocomposites via Surface-Initiated Ring-Opening Metathesis Polymerization. *Macromolecules* **2013**, *46*, 9324–9332.

(26) Fan, X.; Xia, C.; Advincula, R. C. On the Formation of Narrowly Polydispersed PMMA by Surface Initiated Polymerization (SIP) from AIBN-Coated/intercalated Clay Nanoparticle Platelets. *Langmuir* **2005**, *21*, 2537–2544.

(27) Zhou, Q.; Fan, X.; Xia, C.; Mays, J.; Advincula, R. Living Anionic Surface Initiated Polymerization (SIP) of Styrene from Clay Surfaces. *Chem. Mater.* **2001**, *13*, 2465–2467.

(28) Datta, H.; Bhowmick, A. K.; Singha, N. K. Tailor-Made Hybrid Nanostructure of Poly (Ethyl Acrylate)/ Clay by Surface-Initiated Atom Transfer Radical Polymerization. **2008**, 5014–5027.

(29) Bassett, D. C. *Principles of Polymer Morphology (Cambridge Solid State Series)*; Cambridge University Press: Cambridge, England, 1981.

(30) Wang, H.; Keum, J. K.; Hiltner, A.; Baer, E.; Freeman, B.; Rozanski, A.; Galeski, A. Confined Crystallization of Polyethylene Oxide in Nanolayer Assemblies. *Science (80-.).* **2009**, *323*, 757–760.

(31) Bates, F. S.; Fredrickson, G. H. Block Copolymers—Designer Soft Materials. *Phys. Today* **1999**, *52*, 32.

(32) Cochran, E. W.; Morse, D. C.; Bates, F. S. Design of ABC Triblock Copolymers near the ODT with the Random Phase Approximation. *Macromolecules* **2003**, *36*, 782–792.

(33) Matyjaszewski, K.; Tsarevsky, N. V. Nanostructured Functional Materials Prepared by Atom Transfer Radical Polymerization. *Nat. Chem.* **2009**, *1*, 276–288.

(34) Matyjaszewski, K.; Jakubowski, W.; Min, K.; Tang, W.; Huang, J.; Braunecker, W. A.; Tsarevsky, N. V. Diminishing Catalyst Concentration in Atom Transfer Radical Polymerization with Reducing Agents. *Proc. Natl. Acad. Sci.* **2006**, *103*, 15309–15314.

(35) Mogri, Z.; Paul, D. . Gas Sorption and Transport in Side-Chain Crystalline and Molten Poly(octadecyl Acrylate). *Polymer (Guildf).* **2001**, *42*, 2531–2542.

(36) Fox, T. G.; Flory, P. J. Second-Order Transition Temperatures and Related Properties of Polystyrene. I. Influence of Molecular Weight. *J. Appl. Phys.* **1950**, *21*, 581–591.

(37) Jordan, E. F. Side-Chain Crystallinity. III. Influence of Side-Chain Crystallinity on the Glass Transition Temperatures of Selected Copolymers Incorporating N-Octadecyl Acrylate or Vinyl Stearate. *J. Polym. Sci. Part A-1 Polym. Chem.* **1971**, *9*, 3367–3378.

(38) Zhao, H.; Shipp, D. a. Preparation of Poly(styrene- Block -Butyl Acrylate) Block Copolymer−Silicate Nanocomposites. *Chem. Mater.* **2003**, *15*, 2693–2695.

(39) Behling, R. E.; Wolf, L. M.; Cochran, E. W. Hierarchically Ordered Montmorillonite Block Copolymer Brushes. *Macromolecules* **2010**, *43*, 2111–2114.

(40) Hang, P. T. Methylene Blue Absorption by Clay Minerals. Determination of Surface Areas and Cation Exchange Capacities (Clay-Organic Studies XVIII). *Clays Clay Miner.* **1970**, *18*, 203–212.

(41) Behling, R. E.; Williams, B. a.; Staade, B. L.; Wolf, L. M.; Cochran, E. W. Influence of Graft Density on Kinetics of Surface-Initiated ATRP of Polystyrene from Montmorillonite. *Macromolecules* **2009**, *42*, 1867–1872.

(42) Shen, Y.-H. Estimation of Surface Area of Montmorillonite by Ethylene Oxide Chain Adsorption. *Chemosphere* **2002**, *48*, 1075–1079.

(43) Jordan, R.; Ulman, a; Kang, J. F.; Rafailovich, M. H.; Sokolov, J. Surface-Initiated Anionic Polymerization of Styrene by Means of Self-Assembled Monolayers. *J. Am. Chem. Soc.* **1999**, *121*, 1016–1022.

(44) Yamamoto, S.; Ejaz, M.; Tsujii, Y.; Fukuda, T. Surface Interaction Forces of Well-Defined, High-Density Polymer Brushes Studied by Atomic Force Microscopy. 2. Effect of Graft Density. *Macromolecules* **2000**, *33*, 5608–5612.

(45) Kawasumi, M.; Hasegawa, N.; Kato, M.; Usuki, A.; Okada, A. Preparation and Mechanical Properties of Polypropylene−Clay Hybrids. *Macromolecules* **1997**, *30*, 6333–6338.

(46) Hasegawa, N.; Kawasumi, M.; Kato, M.; Usuki, A.; Okada, A. Preparation and Mechanical Properties of Polypropylene-Clay Hybrids Using a Maleic Anhydride-Modified Polypropylene Oligomer. *J. Appl. Polym. Sci.* **1998**, *67*, 87–92.

(47) Zhang, Q.; Fu, Q.; Jiang, L.; Lei, Y. Preparation and Properties of Polypropylene/montmorillonite Layered Nanocomposites. *Polym. Int.* **2000**, *49*, 1561–1564.

(48) Broadhurst, M. G. An Analysis of the Solid Phase Behavior of the Normal Paraffins. *J. Res. Natl. Bur. Stand. Sect. A Phys. Chem.* **1962**, *66A*, 241.

(49) Bharadwaj, R. K.; Mehrabi, a. R.; Hamilton, C.; Trujillo, C.; Murga, M.; Fan, R.; Chavira, a.; Thompson, a. K. Structure–property Relationships in Cross-Linked Polyester–clay Nanocomposites. *Polymer (Guildf).* **2002**, *43*, 3699–3705.

(50) Zhao, H.; Farrell, B. P.; Shipp, D. a. Nanopatterns of Poly(styrene-Block-Butyl Acrylate) Block Copolymer Brushes on the Surfaces of Exfoliated and Intercalated Clay Layers. *Polymer (Guildf).* **2004**, *45*, 4473–4481.

Chapter 3. Conclusions and Future Work

3.1 Conclusions

In Chapter 2, a series of poly(octadecyl acrylate-block-polystyrene) grafted montmorillonite clay (MMT-PODA-PS) nanocomposites resembling thermoplastic elastomers were successfully synthesized and characterized for the first time. Surface initiated activators regenerated by electron transfer atom transfer radical polymerization (ARGET ATRP) using a quaternary ammonium functionalized initiator was used to control the architecture of the block copolymers (BCPs) anchored to the surface of MMT; this polymerization methodology simultaneously promoted exfoliation and good dispersion of the MMT platelets. The resultant nanocomposite showed a higher degree of clay inclusion without significant aggregation of nanofillers in the polymer matrix compared to melt- or solution-mixed analogs using preformed polymers. This feature directly contributed to the optical transparency of films made from these nanocomposite materials. Surface initiated polymerization also enabled the semi-crystalline PODA portions of the chains to be more densely packed near the MMT surfaces resulting in a significant increase in the crystallinity of the PODA side chains. Higher crystallinity in polymer nanocomposites is a desirable attribute for barrier film materials and this is an area for future study.

3.2 Future Work

With the synthesis of the MMT-PODA-PS composite system in hand, there are several areas of interest for future research which aim to gain a deeper understanding about the interaction between the MMT filler and BCP matrix. In addition, a more thorough study of their properties and how they are connected to their unique structure would be instructive to realizing their full potential in applications.

3.2.1 Morphological behavior

In the previous chapter, several imaging results were shown for the MMT-BCP composites primarily to demonstrate the exfoliation and dispersion of clay sheets in the polymer matrix. However, further investigation of the morphological behavior of the PODA-PS BCP grafted to clay sheets is recommended. Previous studies have shown that adding a filler material into a BCP matrix can significantly alter the phase diagram.[1–4] For example, Behling et al. investigated poly(n-butyl acrylate-block-styrene) (PnBA-PS) BCPs that were directly attached to MMT filler and found that the lamellar morphology is more preferred than for free PnBA-PS BCPs.[4] They constructed a BCP phase diagram, which clearly shows lamellar structures outside the expected compositional regions for neat PnBA-PS BCP (**Figure 3.1**). The MMT-PnBA-PS samples were annealed at 150 °C *in vacuo* for 4 days and the aforementioned behavior did not depend on the order of the two blocks.

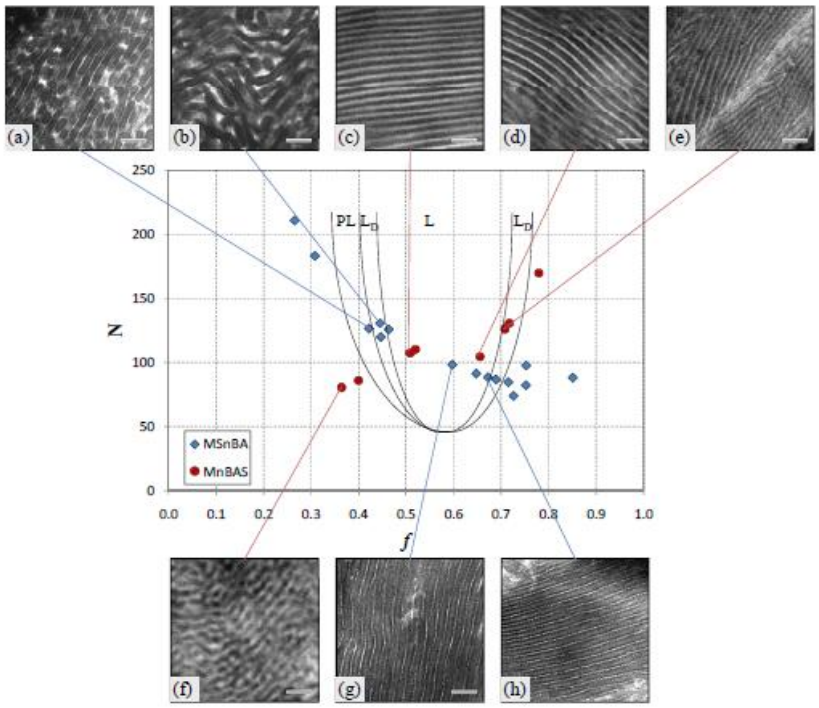

Figure 3.1: Representative transmission electron microscopy (TEM) micrographs of different observed morphologies in MMT-PS-PnBA nanocomposites, perforated lamellae, disordered lamellae, and lamellae. Phase lines are an approximation intended to guide the eye. Diamonds refer to MMT-PS-PnBA and circles refer to MMT-PnBA-PS. Scale bar is 50nm. Reproduced with permission from ref.[4] Copyright © 2015 Wiley Periodicals, Inc.

An outstanding question of why the lamellar morphology was not observed in our experiments is discussed below along with recommended modifications that could be made to our experimental procedures for producing such structures. In our studies, we have attempted thermal annealing of MMT-PODA-PS samples at 170 °C under vacuum for up to 4 days. However, we did not observe by microscopy clear phase segregation and/or formation of microdomains for the different blocks, although domains rich in each block were strongly suggested by differential scanning calorimetry thermograms. One contributing factor could be the much longer side chain for ODA molecules compared to

nBA, which renders the PODA block relatively inflexible/bulky block compared to nBA. Beiner and Huth have concluded from X-ray scattering and relaxation spectroscopy data for a series of poly(n-alkyl acrylates) and poly(n-alkyl methacrylates) that nanophase separation occurred in the polymer melt for polymers with long side chains, and the alkyl groups of the polymers aggregate and form self-assembled alkyl nanodomains with a typical size of 0.5-2 nm depending on the length of side chains.[5] The mobility of the polymer backbone is restricted as the side chain length increases. For poly(n-alkyl acrylate), the cross over from amorphous to crystalline alkyl nanodomains started at polymers with side chains of 10 carbons.[6] The impact of this structural transition on the mobility of the polymer backbone remains an interesting research topic for further studies. We suspect that this inflexibility/bulkiness dramatically reduces the mobility of the BCP during thermal annealing which limits its ability to thermally rearrange, especially considering that all the PODA segments are anchored on the surface of relatively stiff clay sheets (another mobility restricting factor). Thermal annealing or solvent annealing for much longer periods of time could be potential strategies to reach equilibrium structures in our BCP.

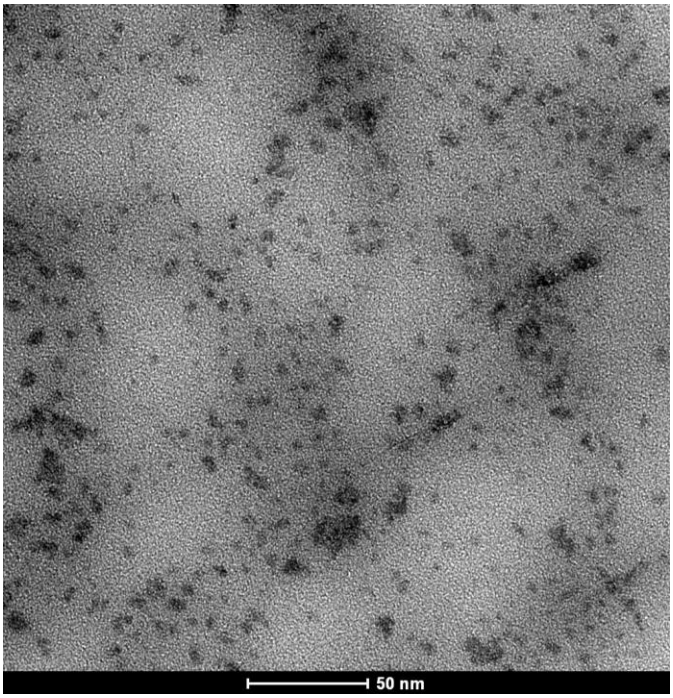

Figure 3.2: TEM image of MMT-PODA-PS nanocomposite. Dark spots are residual metals in the sample.

In the TEM images of the microtomed thin film MMT-PODA-PS samples, we have observed quite a number of dark residual impurities (**Figure 3.2**) which were identified as metal tin (Sn) by dark field TEM with energy-dispersive spectroscopy (EDS) elemental analysis. With an ARGET ATRP process where the copper(Ⅱ) chloride catalyst amount is below 100 ppm, the removal of catalyst and reducing agent is often times not a major concern.[7] In our synthesis, however, a relatively high ratio of initiator to catalyst was used, leading to a higher concentration of reducing agent. This high amount of catalyst and reducing agent was required due to the reaction kinetics for controlled polymerization of ODA monomer, which has a much higher propagation rate and a much lower termination rate than acrylate monomers with shorter side chains.[8] The residual metal in the sample could mask contrast between different domains even after staining. Therefore, removal of

tin and copper could be a necessary step for properly acquiring high quality images of MMT-PODA-PS structures. In conclusion, more extensive studies optimizing annealing conditions and sample purification for imaging needs should be completed in order to draw solid conclusions regarding the morphological behavior of PODA-PS BCPs that are attached to clay sheets.

3.2.2 Applications of MMT-BCP nanocomposites

Barrier properties of semi-crystalline polymer-clay nanocomposites are presumably determined by two contributors: the crystalline structure of the polymer matrix and the dispersion of clay sheets. Both the presence of the crystalline structure[9,10] and the plate-like clay sheets[11] are generally impermeable to small penetrant molecules, forcing those molecules to travel along a tortuous path through the amorphous phase. Previous experimental work on polyethylene terephthalate-clay nanocomposites synthesized by in-situ polymerization showed a 2-fold reduction in oxygen permeability with only 1wt% addition of clay.[12]

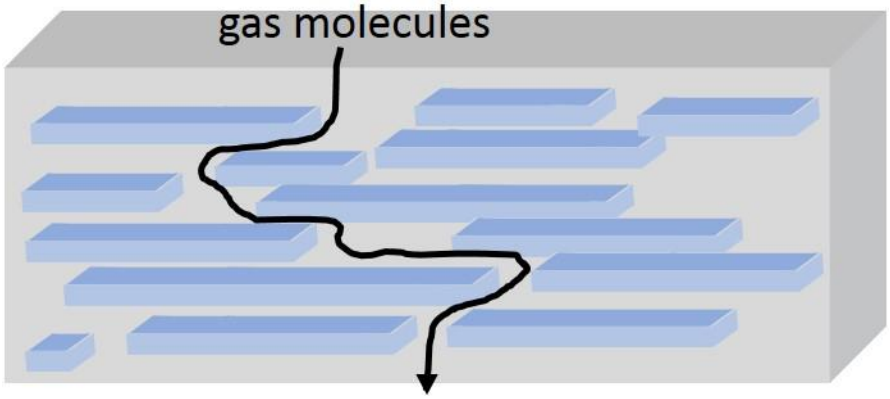

Figure 3.3: Permeation path imposed by nanoplatelet modification of polymer films.

Thus, the additional barrier provided by the high crystallinity from the PODA block in our PODA-PS-MMT block copolymers provides strong motivation for use of this

polymer as a barrier material. However, the high crystallinity also led to a decrease in the mechanical properties of the material resulting in brittle behavior, which was seemingly not improved by the glassy state of the other block (PS). To increase ductility, it may be interesting to synthesize one block composed of both amorphous and semi-crystalline acrylate monomers, instead of making a homopolymer PODA block. The inclusion of more rubbery acrylate units may mitigate the brittle behavior. An alternative strategy could be to reduce the grafting density of the chains on the MMT surface by blending initiator-functionalized with alkyl-functionalized quaternary ammonium molecules. This may allow the chains on nearby MMT platelets to more easily interdigitate for transferring mechanical load. A third strategy could be to introduce crosslinks between chains on adjacent MMT platelets. This could be accomplished by blending together two different MMT-BCP materials with a small fraction of complementary reactive groups (amines and epoxides or alkynes and azides, among many other possibilities) near chain ends or by doping into the composite a universal cross-linker such as bisbenzophenone. If the mechanical properties of these composites can be enhanced, the composite films can be tested more rigorously for membrane applications.

3.3 REFERENCES

(1) Bockstaller, M. R.; Mickiewicz, R. a.; Thomas, E. L. Block Copolymer Nanocomposites: Perspectives for Tailored Functional Materials. *Adv. Mater.* **2005**, *17*, 1331–1349.

(2) Ha, Y.; Kwon, Y.; Breiner, T.; Chan, E. P.; Tzianetopoulou, T.; Cohen, R. E.; Boyce, M. C.; Thomas, E. L. An Orientationally Ordered Hierarchical Exfoliated Clay−Block Copolymer Nanocomposite. *Macromolecules* **2005**, *38*, 5170–5179.

(3) Behling, R. E.; Wolf, L. M.; Cochran, E. W. Hierarchically Ordered Montmorillonite Block Copolymer Brushes. *Macromolecules* **2010**, *43*, 2111–2114.

(4) Behling, R. E.; Kalluru, S. H.; Cochran, E. W. Morphological and Mechanical Behavior of Montmorillonite Grafted Block Copolymer Brushes. *J. Polym. Sci. Part B Polym. Phys.* **2016**, *54*, 353–361.

(5) Beiner, M.; Huth, H. Nanophase Separation and Hindered Glass Transition in Side-Chain Polymers. *Nat. Mater.* **2003**, *2*, 595–599.

(6) Jordan, E. F.; Feldeisen, D. W.; Wrigley, A. N. Side-Chain Crystallinity. I. Heats of Fusion and Melting Transitions on Selected Homopolymers Having Long Side Chains. *J. Polym. Sci. Part A-1 Polym. Chem.* **1971**, *9*, 1835–1851.

(7) Matyjaszewski, K.; Jakubowski, W.; Min, K.; Tang, W.; Huang, J.; Braunecker, W. A.; Tsarevsky, N. V. Diminishing Catalyst Concentration in Atom Transfer Radical Polymerization with Reducing Agents. **2006**, *103*, 15309–15314.

(8) Beers, K.; Matyjaszewski, K. The Atom Transfer Radical Polymerization of Lauryl Acrylate. *J. Macromol. Sci. Part A* **2001**, *38*, 731–739.

(9) Michaels, A. S.; Bixler, H. J. Flow of Gases through Polyethylene. *J. Polym. Sci.* **1961**, *50*, 413–439.

(10) Wang, H.; Keum, J. K.; Hiltner, A.; Baer, E.; Freeman, B.; Rozanski, A.; Galeski, A. Confined Crystallization of Polyethylene Oxide in Nanolayer Assemblies. *Science.* **2009**, *323*, 757–760.

(11) Paul, D. R.; Robeson, L. M. Polymer Nanotechnology: Nanocomposites. *Polymer (Guildf).* **2008**, *49*, 3187–3204.

(12) Choi, W. J.; Kim, H. J.; Yoon, K. H.; Kwon, O. H.; Hwang, C. I. Preparation and Barrier Property of Poly(ethylene Terephthalate)/clay Nanocomposite Using Clay-Supported Catalyst. *J. Appl. Polym. Sci.* **2006**, *100*, 4875–4879.

Chapter 4. Water Dispersible Magnetite Nanoparticles with Ultra-high Magnetic Susceptibility for Low Field Applications

4.1 INTRODUCTION

Magnetic nanoparticles have attracted widespread attention due to their potential applications in diverse areas such as contrast agents for electromagnetic subsurface imaging,[1,2] magnetic resonance imaging (MRI),[3,4] targeted drug delivery,[5,6] magnetic hyperthermia treatments,[7,8] wastewater treatment,[9] and data storage.[10–12] These particles, if smaller than 20 nm, are superparamagnetic,[13] in which the unpaired spins of these particles are randomly oriented in the absence of a magnetic field, but can be aligned reversibly by an external magnetic field as a result of the competition between thermal energy and the magnetic anisotropy energy. Magnetite (Fe_3O_4) nanoparticles have appealing characteristics as they have a high saturation magnetization, which is 92.8 emu/g Fe_3O_4,[14] are non-toxic and feasible to produce in large quantities.[15]

An important parameter for low magnetic field applications is the initial magnetic susceptibility (χ), which can be determined from the Langevin equation approximated to the following relationship assuming that the applied field strength (H) is sufficiently small,[16–18]

$$\chi = \left(\frac{\mathrm{dM}}{\mathrm{dH}}\right)_{\mathrm{H}\to 0} = \frac{\Theta \mu_0 \pi {M_d}^2 {D_p}^3}{18 k_{\mathrm{B}} \mathrm{T}}$$

where μ_0 is the magnetic permeability in vacuum, M_d is the bulk (solid) saturation magnetization, D_p is the magnetic diameter of the particle, Θ is the particle volume fraction, k_{B} is Boltzmann's constant, and T is the absolute temperature. Larger particles within the superparamagnetic regime exhibit higher χ. The cluster size, however, also plays an important role in determining the χ when they are colloidally dispersed. Ge et al. have demonstrated that magnetite nanocrystal clusters can respond to external magnetic field

much more sensitively than individual primary nanoparticles without compromising the superparamagnetic characteristics of the ferrofuid.[19]

While abundant studies have been conducted on the saturation magnetization of magnetic nanoparticles, relatively few studies have focused on the initial magnetic susceptibility at low fields (below 13 Oe or 1000 A/m), which is important in cross-well electromagnetic imaging, heavy metal removal from wastewater, etc., where the magnetic field inevitably weakens over a large distance/space. Thus, nanoparticles with high magnetic susceptibility are preferred for magnetic sensor and contrast agent applications. The effect of primary nanoparticle size on the initial susceptibility of an aqueous ferrofluid synthesized by a co-precipitation approach was studied by Yoon et al. and a χ of 0.85 was obtained at a nanoparticle concentration of 1.6% by volume.[20] It was also demonstrated that at low particle concentrations (< 5 vol%), χ increased linearly with the volume fraction of the nanoparticles. At higher concentrations, however, interparticle interactions can lead to a non-linear increase of susceptibility. Fannin et al. observed that an aqueous dispersion of magnetite nanoparticles showed a χ of 0.20 for a 2.3 vol% solution and a χ of 2.92 when the solution was concentrated to 7 vol%.[21] Similarly, Ewijk et al. reported a χ of 0.2 at 2 vol% for a ferrofluid composed of 15 nm magnetite nanoparticles,[14] and a linear increase in χ with particle volume fraction up to ~5 vol%.[22,23] In this work, we focus only on dilute ferrofluid systems (<4.5 vol%) and report χ data at 2 vol% for different systems by linear extrapolation for direct comparison.

Despite the fact that iron oxide nanoparticles (IONPs) are well studied materials, the industrial scale synthesis remains a challenge. The two most industrially applicable ways to synthesize IONPs so far has been co-precipitation and thermal decomposition. Co-precipitation occurs in water with Fe (II) and Fe (III) salts mixed at a 1:2 molar ratio in alkaline conditions in the presence of stabilizers which can be citrate, oleic acid or

polymers (dextran, or polyvinyl alcohol).[24–27] However, co-precipitation in aqueous media usually results in poor crystallinity and a broad size distribution. Recently, thermal decomposition of metal-organic compounds in a high boiling point polyol solvent has been used to produce high quality nanoparticles.[28–30] The obtained nanoparticles are usually coated with a layer of either hydrophilic or hydrophobic ligands depending on the polyol media and the chemical environment of the nanoparticle dispersion. The temperature profile can be controlled to enable fast nucleation and slow crystal growth in order to obtain monodisperse primary particles with targeted sizes.[31,32] The strong coordination of the polyol solvent with iron cations on the IONP surface forms stable colloidal dispersions with a small cluster size. Solvents such as diethylene glycol (DEG), triethylene glycol (TEG) and ascorbic acid can also act as a mild reducing agent throughout the reaction to control oxidation state of the nanoparticles.

Herein, we report a new method of synthesizing magnetite nanoparticles which involves thermal decomposition of Fe (II) acetate in TEG at 210 °C under ambient pressure. The synthesis yields highly crystalline magnetite nanoparticles with a relatively uniform primary particle diameter around 16 nm. These IONPs showed a high initial susceptibility of 3.5 at 2 vol% under an applied magnetic field of 3 Oe, and a saturation magnetization close to the theoretical limit of bulk magnetite at high fields of ~10 kOe. These nanoparticles are readily dispersible in aqueous media and suitable for a variety of low magnetic field applications. The nanoparticles are coated with a thin layer of silica for stabilization making them amenable for a range of subsequent functionalizations.[15]

4.2 RESULTS AND DISCUSSION

4.2.1 Synthesis and characterization of IONP

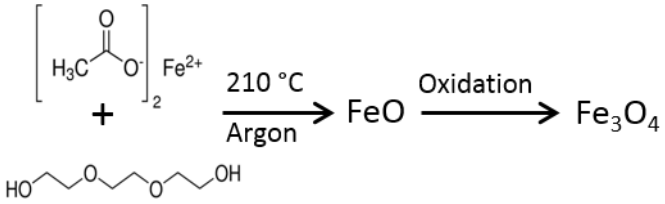

Scheme 4.1: Synthesis route of magnetite nanoparticles.

The IONPs were synthesized by thermal decomposition of iron (II) acetate in the presence of TEG at 210 °C. The molar ratio of iron (II) acetate to TEG was varied at 1:12, 1:22 and 1:33 to control the particle size of the IONPs. The synthesis was carried out using an overhead mechanical stirrer to avoid aggregation that could take place if using a submerged magnetic stir bar. A generally accepted reaction mechanism is composed of a two-step process (**Scheme 4.1**): first the formation of black wüstite (FeO) nanoparticles and then the formation of magnetite (Fe_3O_4) by oxidation.[33,34] Iron (II) acetate decomposed around 180 °C, where the reaction color rapidly turned from light brown to black. The reaction was heated to 210 °C and maintained at this temperature for two hours to allow crystal growth under an argon atmosphere before the heat was removed. The resulting TEG capped magnetic nanoparticles were readily dispersible in water (pH=3.5) with negligible aggregation after removal of excess TEG.

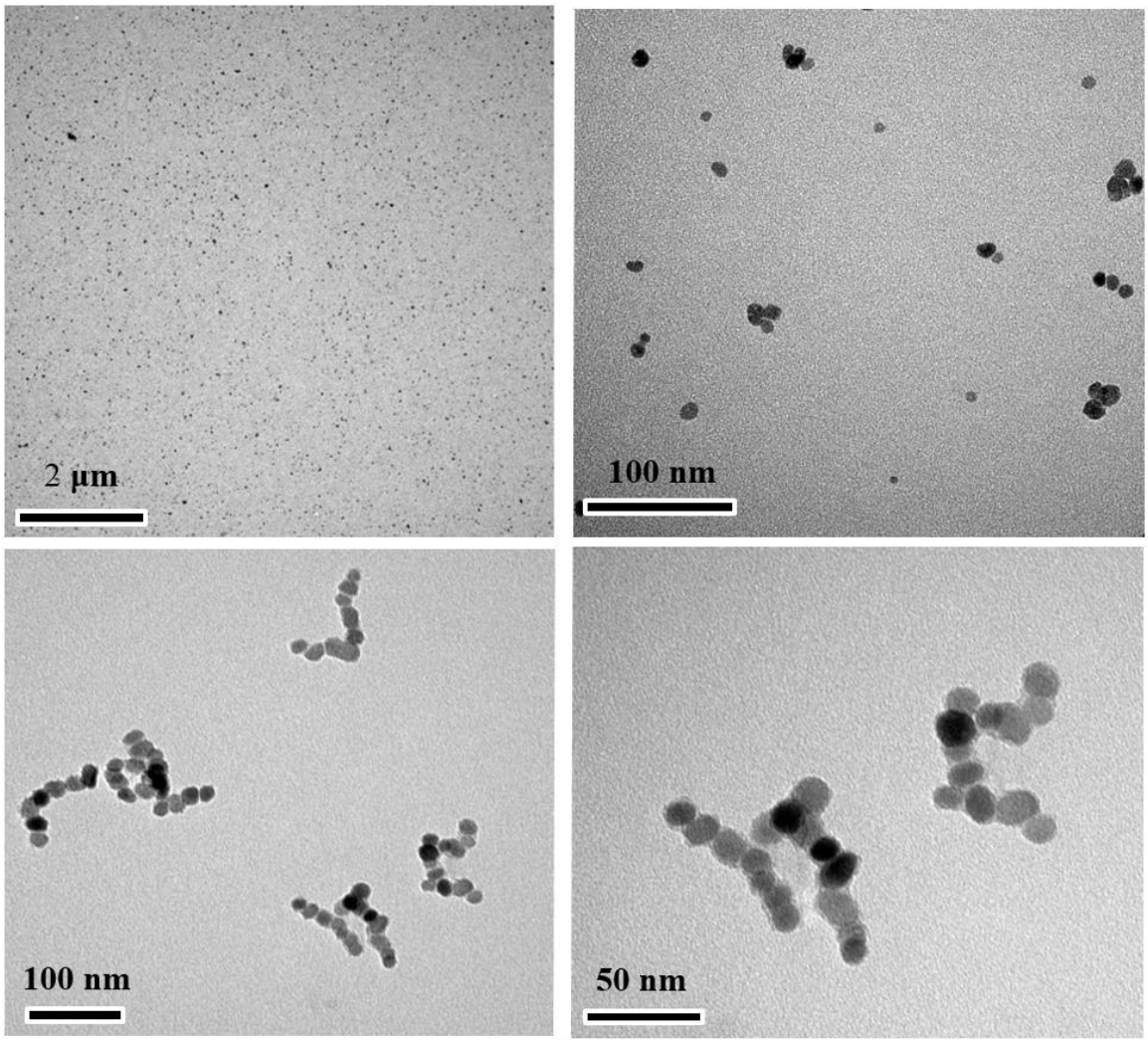

Figure 4.1: Representative transmission electron microscopy (TEM) images showing clusters and primary particles of TEG functionalized IONPs.

The size of the primary IONPs were examined with TEM and detailed images are provided in **Figure A.1** and **Figure A.2** in Appendix A. The primary particle size increased with the concentration of the precursor in the reaction (**Table A.1**). The molar ratio of 1:12 (iron(II) acetate to TEG) yielded the largest spherical primary particles among the three with an average size of (15.8±1.5 nm) (**Figure 4.1**), yet small enough to be in the

superparamagnetic regime. The cluster size (**Figure 4.1**) was consistent with the hydrodynamic size of ~42 nm obtained by dynamic light scattering (DLS). No significantly bigger aggregates were observed under low magnification.

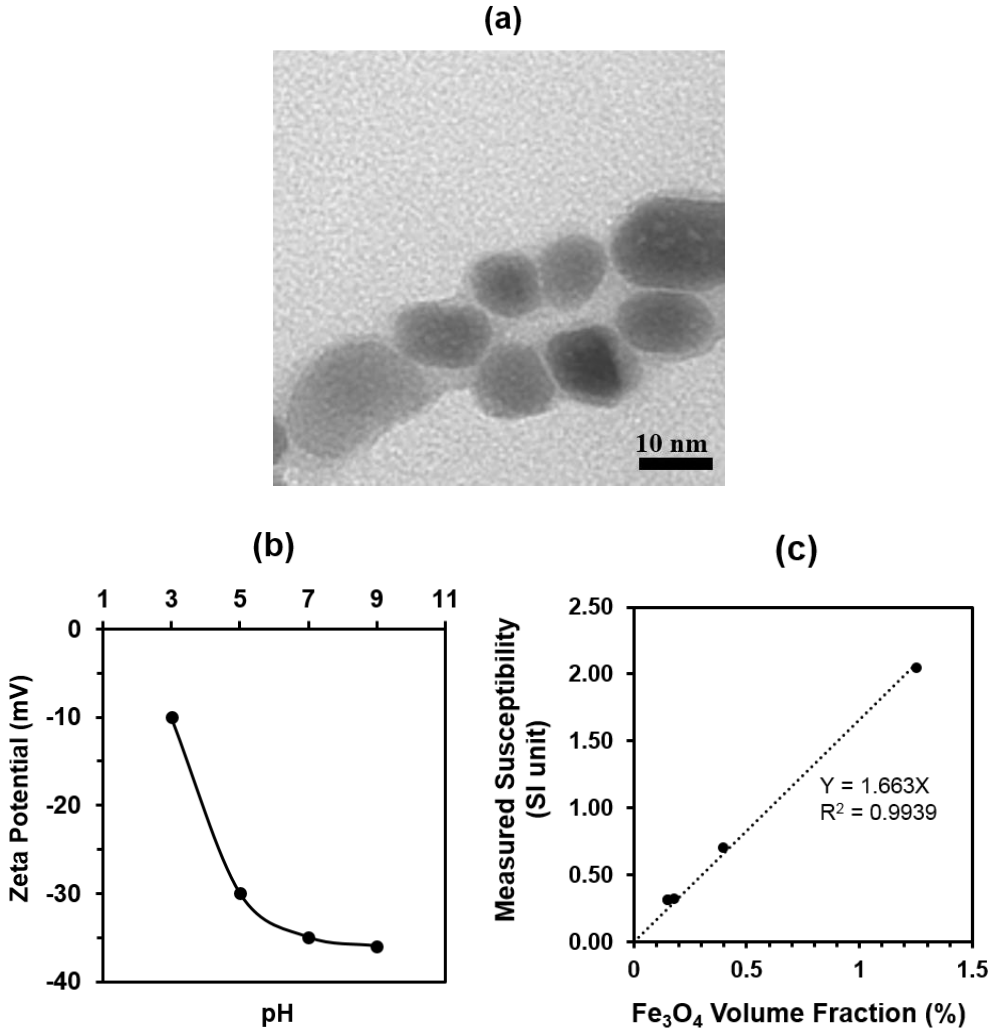

Figure 4.2: (a) TEM of silica coated IONPs (b) zeta potential curve of silica coated IONPs at a range of pHs (c) linear correlation of initial susceptibility under a 3 Oe magnetic field as a function of IONP concentration.

The surface of the TEG coated IONP is relatively inert, which is not easily further functionalized. Furthermore, a monolayer of TEG on IONPs may not be sufficient to

provide steric stabilization at high concentrations which is required for certain applications. Therefore, to improve the surface reactivity and colloidal stability, the IONPs are coated with a thin shell of silica via sol-gel processing, the thickness of which should not compromise the magnetic properties of the magnetic core. In this work, the silica coating procedure reported by Kralj et al.[35] was adapted to our system. The thickest silica coating observed under TEM was 1-2 nm (**Figure 4.2a**) and the hydrodynamic size did not change significantly after coating. The zeta potential of silica coated IONPs was measured at various pHs and the trend showed that the colloid surface bears negative charges at a pH above 3, indicating the potential for an electrostatic repulsion stabilized colloidal dispersion (**Figure 4.2b**). The silica coated IONP dispersion was prepared at different concentrations (<2 vol%) to confirm the linearity of the measured initial susceptibility versus particle volume fraction. The correlation shown in **Figure 4.2c** validates our extrapolation of susceptibility data measured at different concentrations all to 2 vol% for comparison.

Table 4.1: Colloidal dispersion properties of a representative silica coated IONP (Sample D in Table 4.4)

Hydrodynamic Diameter (nm)	Primary Particle Diameter by X-ray diffraction (XRD) [a] (nm)	Primary Particle Diameter from TEM [b] (nm)	Magnetic Diameter [c] (nm)	Concentration of Fe_3O_4 (mg/mL)	Vol% of Fe_3O_4	Measured Susceptibility (SI)	2 vol% Susceptibility (SI)	Saturation Magnetization (emu/g Fe_3O_4)
34	13.4	16.0 ± 2.8	17.5	25.1	0.478	0.813	3.41	92.0

a. Calculated by Scherrer equation.
b. Volume averaged diameters and standard deviation were obtained with image analysis of >100 nanoparticles for each sample in Image J.
c. Calculated from Langevin equation with a lognormal particle size distribution.[17]

4.2.2 Crystalline structure characterization

The crystalline structure of the powdered sample of IONP was studied by XRD (**Figure 4.3**). An inverse spinel structure of magnetite crystalline phase was identified with the International Center for Diffraction Data (ICDD) card No. 19-0629. The diffraction pattern is indexed to a cubic spinel Fe_3O_4 structure, showing (220), (311), (400), (422), (511), and (440) diffraction peaks. It is known that the bulk magnetite (Fe_3O_4) and maghemite (γ-Fe_2O_3) have nearly identical spinel structure with only about 1% difference in the cubic lattice constant, which is very challenging to discern from the XRD patterns.[36,37] The sharp scattering peaks indicate a highly crystalline structure of the nanoparticles. The Scherrer equation was used to calculate the crystallite size of the particle using the (311) peak. The calculated crystalline sizes of IONPs is 13.4 nm which is in good agreement with sizes measured by means of TEM. τ is the mean size of the ordered crystalline domains. K is the shape factor of 0.9. λ is the wavelength of the Cu K-alpha X-ray. β is the line broadening at half the maximum intensity (FWHM). θ is the Bragg angle.

$$\tau = \frac{K\lambda}{\beta \cos\theta} \quad , K = 0.9, \lambda = 0.15418 \ nm, \beta = 0.0108, \theta = 17.7°$$

$$\tau = 13.4 \ nm$$

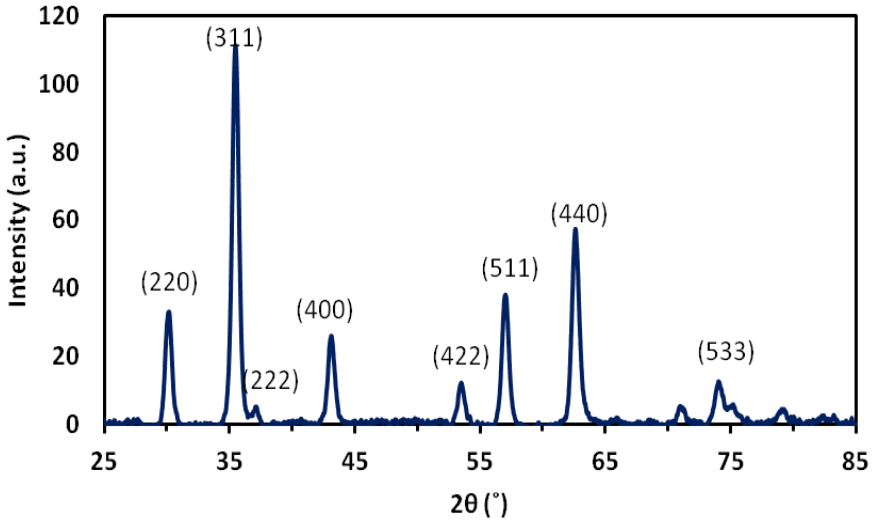

Figure 4.3: Representative powder XRD spectra of magnetite nanoparticles.

Table 4.2: Mössbauer parameters obtained from fit of the room temperature spectra

Site	Isomer shift (mm/s)[a]	Hyperfine field (T)	Area (%)
A (tetrahedral Fe^{3+})	0.34	50.4	74
B (octahedral Fe^{3+}, Fe^{2+})	0.38	44.4	26

*a. The isomer shift was calibrated to α-Fe foil.

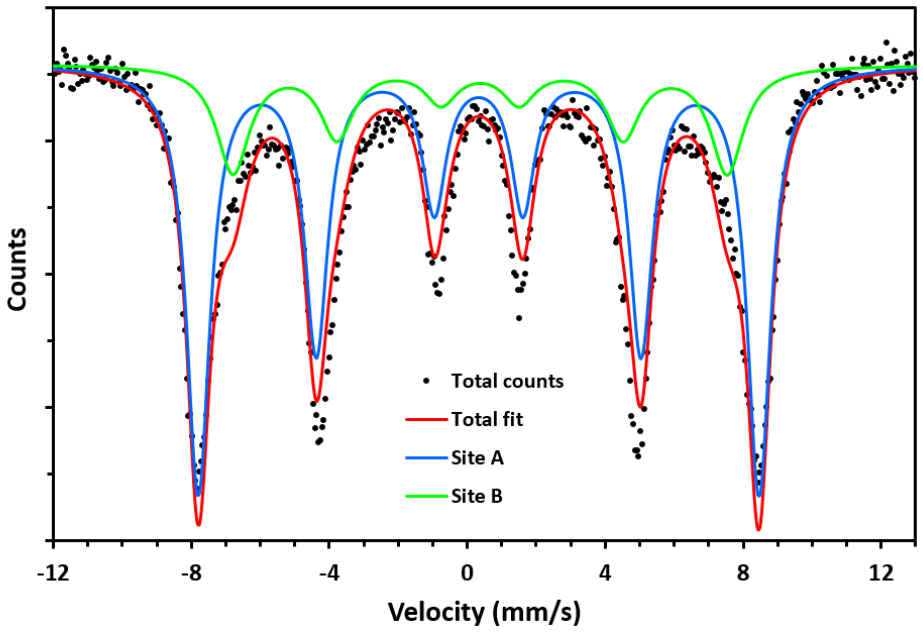

Figure 4.4: Mössbauer spectroscopy of TEG coated IONPs.

Room temperature Mössbauer spectroscopy measurements were performed to further distinguish the crystalline phase between magnetite (Fe_3O_4) and maghemite (γ-Fe_2O_3). The measured spectrum was fit to two discrete magnetic sextets (**Figure 4.4**). The hyperfine parameters are listed in **Table 4.2**. The narrower sextet with the smaller isomer shift of 0.34 mm/s and the larger hyperfine field of 50.4 T was associated with the high spin Fe^{3+} ions occupying the tetrahedral A sites in the inverse spinel structure of magnetite. The broader sextet with the higher isomer shift of 0.38 mm/s and lower hyperfine field of 44.4 T would correspond to the octahedral B sites occupied by Fe^{2+} and Fe^{2+} ions.[38] The sample is therefore identified as a magnetite (Fe_3O_4) phase. The lower isomer shift of sextet for site B (0.38 mm/s) in our magnetite compared to a previously reported bulk value for stoichiometric Fe_3O_4 (0.66 mm/s)[39] could imply that our sample is nonstoichiometric with a lower content of Fe^{2+} ions than stoichiometric Fe_3O_4, or could be attributed to the small

size of our synthesized nanoparticles.[40,41] The line broadening for room temperature spectra can be attributed to the size distribution of the nanoparticles.

4.2.3 Magnetic properties of silica coated IONPs

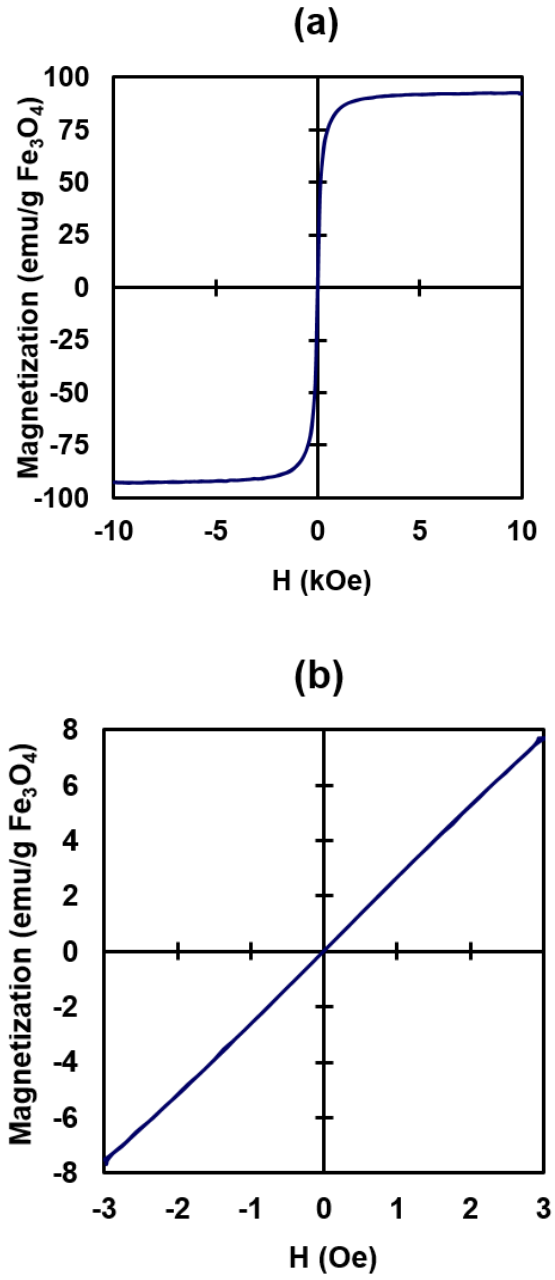

Figure 4.5: Magnetization loop of IONP dispersions up to (a)10 kOe and (b) 3 Oe by vibrating sample magnetometer (VSM).

Magnetic properties of the silica coated IONPs were measured by VSM (**Figure 4.5**) where particles are vibrated in a direction perpendicular to the magnetic field. The unpaired spins of the IONPs are oriented under the applied field, the strength of which is swept over a range of magnetic fields (H) at a steady speed. The synthesized IONP dispersions were examined under both high and low magnetic field to investigate the initial susceptibility and saturation magnetization of IONPs, respectively. Specifically, to determine the saturation magnetization, a high field sweep from -10 kOe to +10 kOe was applied to generate a full magnetization loop [(**Figure 4.5a**]. The measured saturation magnetization of a representative sample (Sample D; **Table 4.1**) was 92.0 emu/g Fe_3O_4, approaching the theoretical saturation magnetization value of bulk magnetite (92.8 emu/g Fe_3O_4). This is a good indication that the synthesized magnetite cores have a highly ordered crystalline structure with little magnetic dead layer on the surface, and the surface coating is thin enough not to compromise the core properties. The uniform crystallinity over the entire volume of the particle was confirmed by bright field HR-TEM which shows a measured d-spacing of 4.8 Å (**Figure 4.6a**), corresponding to the (111) planes of the Fe_3O_4 single crystal with cubic inverse spinel structure.[42–44] A complementary suite of electron microscopy techniques and associated spectroscopic methods provide valuable insight into the core–shell structure of the silica coated IONPs. STEM-EDX mapping was performed to reveal the Fe rich core with a Si rich shell while O was present in both the core and the shell with more prevalence in the core structure (**Figure 4.6b-f**).

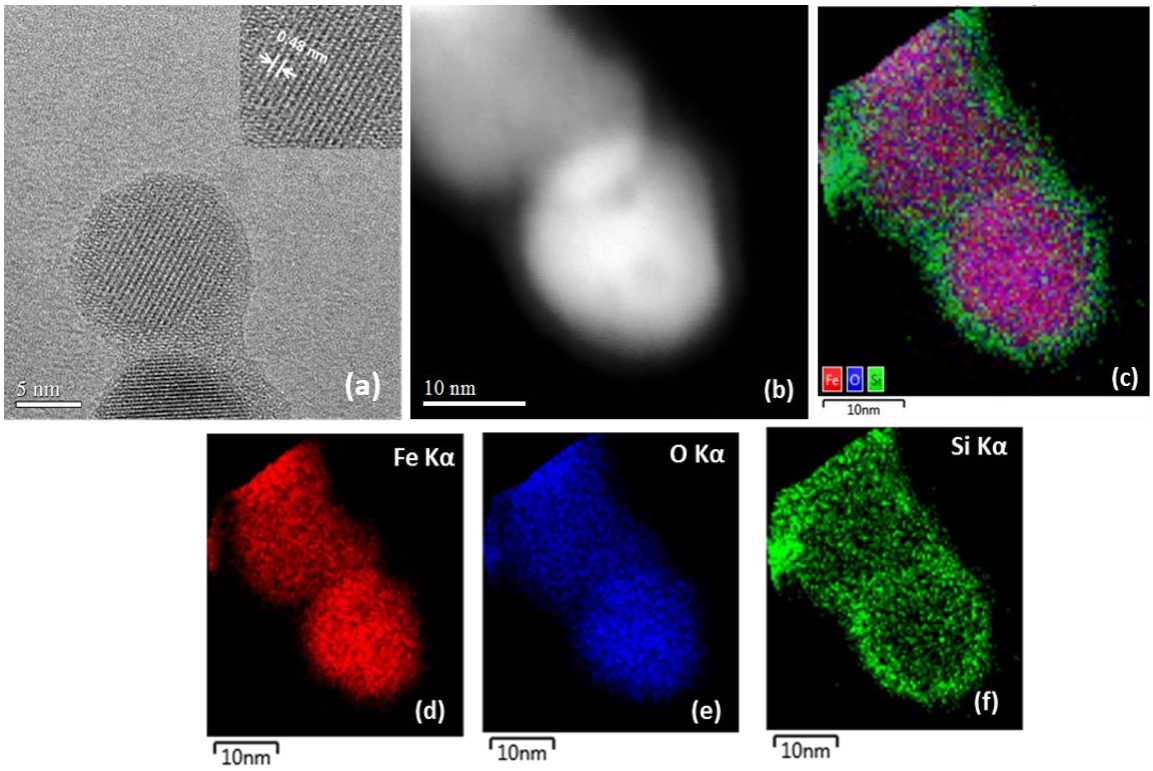

Figure 4.6: Electron microscopy imaging and elemental analyses of IONPs. (a) Bright-field HR-TEM image of IONPs. Inset represents the lattice fringes, (b) HAADF-STEM image of silica coated IONPs, (c) STEM-EDS mapping of silica coated IONPs and (d-f) elemental mapping of the Fe, O and Si.

The initial magnetic susceptibility was measured by applying a low magnetic field sweep up to 3 Oe on the same magnetite sample [**Figure 4.5b**]. The magnetization of the colloids was 8.0 emu/g Fe_3O_4, reaching about one tenth of its saturation magnetization under an external field of only 3 Oe. The slope of the magnetization curve was used to calculate the initial magnetic susceptibility (χ) which is 3.41 on an extrapolated 2 vol% basis (**Table 4.1**). The magnetic core size was also calculated using the method from Chantrell et al. by assuming a lognormal size distribution in the ferrofluid[17] and as tabulated in **Table 4.1** and **Table 4.2**, the results agreed well the sizes measured by TEM (**Figure 4.1** and **Figure A.2**).

In comparison with commercially available ferrofluids (**Table 4.3**), the χ obtained here is at least 6 times higher than the best commercial sample measured at the same condition. Negligible hysteresis was observed from magnetization loops, showing the superparamagnetic characteristics of the synthesized IONPs. With all the aforementioned characterization on the synthesized IONPs, we attribute the high susceptibility of the particles to the following: (i) the large size of primary particles (15.8 ± 1.5 nm) in the superparamagnetic regime, and controlled cluster size (~42nm),[45,46] (ii) a highly crystalline magnetite phase as evidenced by XRD, Mössbauer spectroscopy and HRTEM and (iii) controlled surface modification without disruption of the core structure. In our case, the silica coating provides highly stabilized colloids in solution (unchanged hydrodynamic size). It is thin enough not to shield magnetic sensitivity of the core, as evidenced by consistent susceptibility of TEG coated IONPs versus silica coated IONPs (**Table 4.4**). By coating a silica shell, we also avoided the possible spin disorder on the particles surface which could be caused by usage of ionic surfactants. As revealed by previous studies, surface spin disorder could reduce the inter-particle dipolar interaction, leading to a reduced magnetic susceptibility.[47]

Table 4.3: Comparison of magnetic properties of synthesized IONP and commercial ferrofluid

Sample	Source	Hydrodynamic Diameter (nm)	Primary Particle Diameter from TEM (nm)	Concentration of Fe_3O_4 (mg/mL)	Vol% of Fe_3O_4	Measured Susceptibility (SI)	2 vol% Susceptibility (SI)	Saturation Magnetization (emu/g Fe_3O_4)
Ferrofluid 1	FerroTec MSG W08	53	8.1 ± 1.9	45.2	0.861	0.255	0.59	99.1
Ferrofluid 2	FerroTec MSG W10	49	7.9 ± 2.0	35.8	0.683	0.213	0.62	97.8

To investigate the reproducibility of the IONPs, the synthesis was repeated multiple times and at various reaction scales. The silica coating did not cause any obvious loss of

magnetic properties as evidenced by the comparison of TEG and silica coated IONPs as presented in **Table 4.4** showing an average initial magnetic susceptibility χ of 3.55 ± 0.26 and a saturation magnetization of 85.8 ± 6.5 emu/g Fe_3O_4. The high reproducibility of producing the sensitive magnetic cores and a robust surface coating protocol renders this synthetic procedure of much industrial interest for large scale production of IONPs for remote sensing and mapping applications.

Table 4.4: Reproducibility of TEG-functionalized IONPs at different reaction scales

Sample	Hydrodynamic Size (nm)	Concentration of Fe_3O_4 (mg/mL)	Vol% of Fe_3O_4	Primary Particle Diameter from TEM[a] (nm)	Calculated Magnetic Diameter (nm)	Measured Susceptibility (SI)	2 vol% Susceptibility (SI)	Saturation Magnetization (emu/g Fe_3O_4)	Reaction Scale (gram of precursor)	Coating on the IONP
A	33	24.4	0.465	14.3 ± 2.2	16.3	0.766	3.29	76.3	5.4	TEG
B	26	97.4	1.86	17.6 ± 3.5	18.8	3.30	3.56	93.8	5.2	TEG
C	53	21.1	0.363	14.9 ± 2.1	18.2	0.680	3.36	85.1	3.5	TEG
D	34	25.1	0.478	16.0 ± 2.8	17.5	0.813	3.41	92.0	9.0	Silica
E	54	35.3	0.672	17.5 ± 3.1	19.5	1.341	3.99	82.8	6.5	Silica
F	53	47.4	0.904	14.6 ± 2.6	16.9	1.68	3.71	84.2	3.8	Silica

a. Diameters was measured with Image J for >100 nanoparticles and averaged on the volume basis with standard deviation.

4.3 CONCLUSIONS

Monodisperse superparamagnetic magnetite nanoparticles were synthesized via thermal decomposition of iron(II) acetate in TEG. The nanoparticles formed stable aqueous colloidal dispersions with primary particle sizes in the range of 12-17 nm and average cluster hydrodynamic diameters below 50 nm. The magnetic cores were coated with a thin shell of silica to make them amenable for further functionalization and colloidal stability. XRD and electron microscopy revealed highly crystalline IONPs with little amorphous structure on the surface. Mössbauer spectroscopy further confirmed that these particles possess the crystalline magnetite phase. These structural features contributed to a high

saturation magnetization approaching that of bulk magnetite. The controlled primary particle size and cluster size result in ultra-high initial magnetic susceptibilities at extremely low fields, 6 times exceeding their commercial counterpart. The synthesis is highly reproducible and scalable to large quantities, opening up the possibility of using these IONPs for industrial low magnetic field applications, like remote sensing and sub-surface imaging.

4.4 EXPERIMENTAL

4.4.1 Materials

Iron (II) acetate [$Fe(CO_2CH_3)_2$] was purchased from Alpha Aesar. TEG ($C_6H_{14}O_4$) and tetraethyl orthosilicate (TEOS) [$Si(OC_2H_6)_4$] were purchased from Sigma Aldrich, USA, and used without further purification.

4.4.2 Synthesis of TEG-coated iron oxide nanoclusters

IONP syntheses were carried out by modifying the procedure reported by Gunay et al.[48] IONPs were prepared by the thermal decomposition of iron(II) acetate (light brown powder) in the presence of TEG at 210 °C in an inert argon atmosphere while the stirring was carried out using an overhead mechanical stirrer. In a typical synthesis, 5 grams (28.8 mM) of iron (II) acetate were mixed with 50 mL (333 mM) TEG in a 250 mL three-neck round bottom flask equipped with condenser, mechanical stirrer and a heating mantle. The mixture was purged with argon gas for at least 20 min before ramping up to 210 °C in 20 min, and then refluxed at 210 °C for two hours. Heating was then removed and the reaction mixture was cooled to room temperature. The synthesized IONPs were purified by copious washing with a mixture of ethanol and DI water and ethyl acetate if needed to facilitate separation before centrifuging at 10,000 rpm for 10 minutes. The procedure was repeated at least three times to remove excess TEG. The obtained pellets were redispersed in 1wt%

nitric acid and immediately precipitated by adding ethyl acetate and centrifuging. The loosely agglomerated pellets were redispersed with DI water to form a stable colloidal dispersion at a final concentration around 10 mg/mL and pH of 3.5.

4.4.3 Silica coating of IONPs

The silica coating was applied by modifying the procedure of Kralj et al.[35] TEG coated IONPs were dispersed in an alkaline media of pH 12 at a concentration of 0.1 wt%. TEOS was diluted with ethanol at volumetric ratio of 1 : 9 and the mixture was added to the IONPs dispersion over 3.5 hours by a syringe pump while vigorously stirring. The mass ratio of IONPs to TEOS was 0.05. The particles were collected with a strong magnet and washed with copious amounts of DI water. The aqueous dispersion was sonicated using a 400W probe sonicator (Branson, Digital Sonifier 450) at 30% amplitude and centrifuged at 3500 rpm to remove big aggregates. The dispersion was finally concentrated by centrifugal filtration with Amicon Ultracel-10K regenerated cellulose centrifugal filters.

4.4.4 Characterization

4.4.4.1Flame atomic absorption spectroscopy (FAAS)

The concentration of Fe in the dispersion was measured on a GBC 908AA flame atomic absorption spectrometer (GBC Scientific Equipment Pty Ltd). All measurements were conducted at 242.8 nm using an air-acetylene flame. 100 μL of IONP dispersion (20mg/mL) was digested in 900 μL of 12 M HCl overnight; the volume ratio of HCl : nanoparticle dispersion was 9:1. After digestion, the samples were then diluted with 1 wt% HNO_3 to a concentration between 1 and 5 ppm of Fe. Nanoparticles that were coated with silica or polymer were filtered through a 20 nm pore size syringe filter (Whatman ANOTOP 25). The FAAS was calibrated with ferric nitrate nonahydrate solutions in 1% nitric acid at concentrations from 1 to 5 ppm of Fe. The calibration was repeated every

10 samples. The concentration of the original suspension was calculated in the units of mg/mL Fe_3O_4 based upon the measured Fe content.

4.4.4.2 Dynamic light scattering (DLS)

Hydrodynamic sizes (D_H) of aqueous dispersions of the as-prepared iron oxide clusters were measured with a Brookhaven ZetaPALS instrument with the ZetaPlus option at a 90^o scattering angle. The collected auto-correlation function curves were fit with the CONTIN routine to give volume-averaged size distributions. All measurements were made over a period of 2 min and at least three measurements were performed on each sample. The concentration of IONPs for DLS samples were adjusted to obtain a count rate of ~500 kcps. The hydrodynamic diameter reported here is the peak value of the main peak that accounts for >70% of cluster volume.

4.4.4.3 Zeta potential measurements

Electrophoretic mobility of different types of clusters was measured with a Brookhaven Zeta PALS instrument at a 15^o scattering angle at room temperature in 10 mM KCl solution (Debye length = 3 nm). 10 measurements with 30 electrode cycles for each run were performed and data were averaged. Zeta potential was obtained from the electrophoretic mobility using the Smoluchowski model.

4.4.4.4 X-ray diffraction (XRD)

X-ray diffraction was obtained on a Rigaku R-Axis Spider diffractometer with an image plate detector using Cu Kα radiation (λ = 1.54 Å). Samples were prepared on nylon loops and scanned for 10 min rotated at a rate of 10 ^{o}/min.

4.4.4.5 Transmission electron microscopy (TEM)

TEM images were acquired on a FEI Tecnai Spirit Bio Twin TEM operated at 80 kV. The samples were prepared by drop casting a dilute aqueous suspension of IONPs onto 400 mesh Formvar coated copper grids. The average diameter was obtained with Image J in which at least 100 primary particles at various spots of the grid were measured.

High-resolution transmission microscopy (HR-TEM) and HAADF-STEM images were obtained on a field emission JEOL 2010F TEM operated at 200 kV. Scanning transmission electron microscopy Energy dispersive X-ray spectroscopy (STEM-EDX) mapping was done on a JEOL 2010F equipped with an Oxford X-MaxN 80TLE solid state detector. The STEM probe size was ~1 nm and drift correction was performed during the mapping using AutoLock in Oxford's Aztec software while the EDS maps were obtained with acquisition times of more than 1 min. The microscope was operated at 200 KeV accelerating voltage.

4.4.4.6 Vibrating sample magnetometer (VSM)

The initial susceptibility of magnetic fluid samples was measured with a VSM (Microsense model EZ7 and EV7) under a magnetic field with intensity swept between -3 to +3 Oe at a rate of 0.15 Oe/s. Saturation magnetization was measured under a -10 kOe to +10 kOe range swept at a rate of 250 Oe/s. All the magnetic fluid samples are measured at 300 K at a DC field with vibration frequency of 75 Hz.

4.4.4.7 Mössbauer spectroscopy

The Mössbauer spectroscopy measurements were performed at room temperature in transmission geometry with a ^{57}Co source in Rh matrix mounted on a constant acceleration drive. The spectrometer was calibrated using an iron foil. A VORTEX detector with 150 eV resolution was used to discriminate the 14.4 keV radiation. IONPs are dried

and the sample powder were placed between Kapton tapes. Data analysis was performed using in-house software. All isomer shifts are given with respect to metallic α-Fe at room temperature.

4.5 REFERENCES

(1) Daily, W.; Owen, E. Cross-borehole Resistivity Tomography. *Geophysics* **1991**, *56*, 1228–1235.

(2) Al-Ali, Z.; H. Al-Buali, M.; AlRuwaili, S.; Ma, S. M.; Marsala, A. F.; Hulme, C.; Wilt, M. Looking Deep into the Reservoir. *Oilf. Rev. Summer* **2009**, *21*, 38–47.

(3) Na, H. Bin; Song, I. C.; Hyeon, T. Inorganic Nanoparticles for MRI Contrast Agents. *Adv. Mater.* **2009**, *21*, 2133–2148.

(4) Sulek, S.; Mammadov, B.; Mahcicek, D. I.; Sozeri, H.; Atalar, E.; Tekinay, A. B.; Guler, M. O. Peptide Functionalized Superparamagnetic Iron Oxide Nanoparticles as MRI Contrast Agents. *J. Mater. Chem.* **2011**, *21*, 15157.

(5) Schladt, T. D.; Schneider, K.; Schild, H.; Tremel, W. Synthesis and Bio-Functionalization of Magnetic Nanoparticles for Medical Diagnosis and Treatment. *Dalt. Trans.* **2011**, *40*, 6315.

(6) Sun, C.; Lee, J.; Zhang, M. Magnetic Nanoparticles in MR Imaging and Drug Delivery☆. *Adv. Drug Deliv. Rev.* **2008**, *60*, 1252–1265.

(7) Maier-Hauff, K.; Rothe, R.; Scholz, R.; Gneveckow, U.; Wust, P.; Thiesen, B.; Feussner, A.; von Deimling, A.; Waldoefner, N.; Felix, R.; *et al.* Intracranial Thermotherapy Using Magnetic Nanoparticles Combined with External Beam Radiotherapy: Results of a Feasibility Study on Patients with Glioblastoma Multiforme. *J. Neurooncol.* **2007**, *81*, 53–60.

(8) Jordan, A.; Scholz, R.; Wust, P.; Fähling, H.; Roland Felix. Magnetic Fluid Hyperthermia (MFH): Cancer Treatment with AC Magnetic Field Induced Excitation of Biocompatible Superparamagnetic Nanoparticles. *J. Magn. Magn. Mater.* **1999**, *201*, 413–419.

(9) Yavuz, C. T.; Mayo, J. T.; Yu, W. W.; Prakash, A.; Falkner, J. C.; Yean, S.; Cong, L.; Shipley, H. J.; Kan, A.; Tomson, M.; *et al.* Low-Field Magnetic Separation of Monodisperse Fe3O4 Nanocrystals. *Science.* **2006**, *314*, 964–967.

(10) Sun, S. Monodisperse FePt Nanoparticles and Ferromagnetic FePt Nanocrystal Superlattices. *Science.* **2000**, *287*, 1989–1992.

(11) Desvaux, C.; Amiens, C.; Fejes, P.; Renaud, P.; Respaud, M.; Lecante, P.; Snoeck, E.; Chaudret, B. Multimillimetre-Large Superlattices of Air-Stable Iron–cobalt Nanoparticles. *Nat. Mater.* **2005**, *4*, 750–753.

(12) Reiss, G.; Hütten, A. Magnetic Nanoparticles: Applications beyond Data Storage. *Nat. Mater.* **2005**, *4*, 725–726.

(13) Sun, S.; Zeng, H. Size-Controlled Synthesis of Magnetite Nanoparticles. *J. Am. Chem. Soc.* **2002**, *124*, 8204–8205.

(14) Ewijk, G. a Van; Vroege, G. J.; Philipse, A. P. Susceptibility Measurements on a Fractionated Aggregate-Free Ferrofluid. *J. Phys. Condens. Matter* **2002**, *14*, 4915–4925.

(15) Jeong, B. U.; Teng, X.; Wang, Y.; Yang, H.; Xia, Y.; Jeong, U.; Teng, X.; Wang, Y.; Yang, H.; Xia, Y. Superparamagnetic Colloids: Controlled Synthesis and Niche Applications. *Adv. Mater.* **2007**, *19*, 33–60.

(16) Rosensweig, R. E. *Ferrohydrodynamics*; Cambridge ; New York : Cambridge University Press, 1985.

(17) Chantrell, R.; Popplewell, J.; Charles, S. Measurements of Particle Size Distribution Parameters in Ferrofluids. *IEEE Trans. Magn.* **1978**, *14*, 975–977.

(18) Ditsch, A.; Lindenmann, S.; Laibinis, P. E.; Wang, D. I. C.; Hatton, T. A. High-Gradient Magnetic Separation of Magnetic Nanoclusters. *Ind. Eng. Chem. Res.* **2005**, *44*, 6824–6836.

(19) Ge, J.; Hu, Y.; Biasini, M.; Dong, C.; Guo, J.; Beyermann, W. P.; Yin, Y. One-Step Synthesis of Highly Water-Soluble Magnetite Colloidal Nanocrystals. *Chemistry* **2007**, *13*, 7153–7161.

(20) Yoon, K. Y.; Xue, Z.; Fei, Y.; Lee, J. H.; Cheng, V.; Bagaria, H. G.; Huh, C.; Bryant, S. L.; Kong, S. D.; Ngo, V. W.; *et al.* Control of Magnetite Primary Particle Size in Aqueous Dispersions of Nanoclusters for High Magnetic Susceptibilities. *J. Colloid Interface Sci.* **2016**, *462*, 359–367.

(21) Rasa, M. Magnetic Properties and Magneto-Birefringence of Magnetic Fluids. *Eur. Phys. J. E* **2000**, *2*, 265–275.

(22) Huang, W.; Wu, J.; Guo, W.; Li, R.; Cui, L. Study on the Synthesis of ε-Fe3N-Based Magnetic Fluid. *J. Magn. Magn. Mater.* **2006**, *307*, 198–204.

(23) Huang, W.; Wu, J.; Guo, W.; Li, R.; Cui, L. Initial Susceptibility and Viscosity Properties of Low Concentration ε-Fe3 N Based Magnetic Fluid. *Nanoscale Res. Lett.* **2007**, *2*, 155–160.

(24) Massart, R. Preparation of Aqueous Magnetic Liquids in Alkaline and Acidic Media. *IEEE Trans. Magn.* **1981**, *17*, 1247–1248.

(25) Lyon, J. L.; Fleming, D. a.; Stone, M. B.; Schiffer, P.; Williams, M. E.; Park, U. V; Pennsyl, V. Synthesis of Fe Oxide Core/Au Shell Nanoparticles by Iterative Hydroxylamine Seeding. *Nano Lett.* **2004**, *4*, 719–723.

(26) Ditsch, A.; Laibinis, P. E.; Wang, D. I. C.; Hatton, T. A. Controlled Clustering and Enhanced Stability of Polymer-Coated Magnetic Nanoparticles. *Langmuir* **2005**, *21*, 6006–6018.

(27) Sahoo, Y.; Goodarzi, A.; Swihart, M. T.; Ohulchanskyy, T. Y.; Kaur, N.; Furlani, E. P.; Prasad, P. N. Aqueous Ferrofluid of Magnetite Nanoparticles: Fluorescence Labeling and Magnetophoretic Control. *J. Phys. Chem. B* **2005**, *109*, 3879–3885.

(28) Wan, J.; Cai, W.; Meng, X.; Liu, E. Monodisperse Water-Soluble Magnetite Nanoparticles Prepared by Polyol Process for High-Performance Magnetic Resonance Imaging. *Chem. Commun. (Camb).* **2007**, *4*, 5004–5006.

(29) Das, M.; Dhak, P.; Gupta, S.; Mishra, D.; Maiti, T. K.; Basak, A.; Pramanik, P. Highly Biocompatible and Water-Dispersible, Amine Functionalized Magnetite Nanoparticles, Prepared by a Low Temperature, Air-Assisted Polyol Process: A New Platform for Bio-Separation and Diagnostics. *Nanotechnology* **2010**, *21*, 125103.

(30) Feldmann, C.; Jungk, H. O. Polyol-Mediated Preparation of Nanoscale Oxide Particles. *Angew. Chemie - Int. Ed.* **2001**, *40*, 359–362.

(31) Park, J.; Joo, J.; Soon, G. K.; Jang, Y.; Hyeon, T. Synthesis of Monodisperse Spherical Nanocrystals. *Angew. Chemie - Int. Ed.* **2007**, *46*, 4630–4660.

(32) Miguel-Sancho, N.; Bomati-Miguel, O.; Roca, A. G.; Martinez, G.; Arruebo, M.; Santamaria, J. Synthesis of Magnetic Nanocrystals by Thermal Decomposition in Glycol Media: Effect of Process Variables and Mechanistic Study. *Ind. Eng. Chem. Res.* **2012**, *51*, 8348–8357.

(33) Redl, F. X.; Black, C. T.; Papaefthymiou, G. C.; Sandstrom, R. L.; Yin, M.; Zeng, H.; Murray, C. B.; O'Brien, S. P. Magnetic, Electronic, and Structural Characterization of Nonstoichiometric Iron Oxides at the Nanoscale. *J. Am. Chem. Soc.* **2004**, *126*, 14583–14599.

(34) Yin, M.; O'Brien, S. Synthesis of Monodisperse Nanocrystals of Manganese Oxides. *J. Am. Chem. Soc.* **2003**, *125*, 10180–10181.

(35) Kralj, S.; Makovec, D.; Čampelj, S.; Drofenik, M. Producing Ultra-Thin Silica Coatings on Iron-Oxide Nanoparticles to Improve Their Surface Reactivity. *J. Magn. Magn. Mater.* **2010**, *322*, 1847–1853.

(36) Starowicz, M.; Starowicz, P.; Żukrowski, J.; Przewoźnik, J.; Lemański, A.; Kapusta, C.; Banaś, J. Electrochemical Synthesis of Magnetic Iron Oxide Nanoparticles with Controlled Size. *J. Nanoparticle Res.* **2011**, *13*, 7167–7176.

(37) Thanh, N. T. K. *Magnetic Nanoparticles: From Fabrication to Clinical Applications*; 1st ed.; CRC Press, 2012.

(38) R.M. Cornell, U. S. *The Iron Oxides: Structure, Properties, Reactions, Occurrences and Uses*; WILE-VCH: Weinheim, Cambridge, 1996.

(39) Vandenberghe, R. E.; Barrero, C. A.; da Costa, G. M.; Van San, E.; De Grave, E. Mössbauer Characterization of Iron Oxides and (Oxy)hydroxides: The Present State of the Art. *Hyperfine Interact.* **2000**, *126*, 247–259.

(40) Lukashova, N. V.; Savchenko, A. G.; Yagodkin, Y. D.; Muradova, A. G.; Yurtov, E. V. Structure and Magnetic Properties of Iron Oxide Nanopowders. *Met. Sci. Heat Treat.* **2013**, *54*, 550–554.

(41) Roca, A. G.; Marco, J. F.; Morales, M. del P.; Serna, C. J. Effect of Nature and Particle Size on Properties of Uniform Magnetite and Maghemite Nanoparticles. *J. Phys. Chem. C* **2007**, *111*, 18577–18584.

(42) Eom, Y.; Abbas, M.; Noh, H.; Kim, C. Morphology-Controlled Synthesis of Highly Crystalline Fe3O4 and CoFe2O4 Nanoparticles Using a Facile Thermal Decomposition Method. *RSC Adv.* **2016**, *6*, 15861–15867.

(43) Hui, C.; Shen, C.; Tian, J.; Bao, L.; Ding, H.; Li, C.; Tian, Y.; Shi, X.; Gao, H.-J. Core-Shell Fe3O4@SiO2 Nanoparticles Synthesized with Well-Dispersed Hydrophilic Fe 3 O 4 Seeds. *Nanoscale* **2011**, *3*, 701–705.

(44) Abbas, M.; Torati, S. R.; Kim, C. A Novel Approach for the Synthesis of Ultrathin Silica-Coated Iron Oxide Nanocubes Decorated with Silver Nanodots (Fe 3 O 4 /SiO 2 /Ag) and Their Superior Catalytic Reduction of 4-Nitroaniline. *Nanoscale* **2015**, *7*, 12192–12204.

(45) Ge, J.; Hu, Y.; Biasini, M.; Beyermann, W. P.; Yin, Y. Superparamagnetic Magnetite Colloidal Nanocrystal Clusters. *Angew. Chemie Int. Ed.* **2007**, *46*, 4342–4345.

(46) Qiu, P.; Jensen, C.; Charity, N.; Towner, R.; Mao, C. Oil Phase Evaporation-Induced Self-Assembly of Hydrophobic Nanoparticles into Spherical Clusters with Controlled Surface Chemistry in an Oil-in-Water Dispersion and Comparison of Behaviors of Individual and Clustered Iron Oxide Nanoparticles. *J. Am. Chem. Soc.* **2010**, *132*, 17724–17732.

(47) Misra, S. K.; Li, L.; Mukherjee, S.; Ghosh, G. Anisotropic Magnetic Field Observed at 300 K in Citrate-Coated Iron Oxide Nanoparticles: Effect of Counterions. *J. Nanoparticle Res.* **2015**, *17*, 487.

(48) Günay, M.; Baykal, A.; Sözeri, H. Structural and Magnetic Properties of Triethylene Glycol Stabilized Monodisperse Fe3O4 Nanoparticles. *J. Supercond. Nov. Magn.* **2012**, *25*, 2415–2420.

Chapter 5. Effect of Synthesis Conditions on Morphological, Colloidal and Magnetic Behavior of Iron Oxide Nanoparticles

The control of various parameters including the size, shape, colloidal stability, and oxidation state of nanoparticles is historically nontrivial for many nanoparticle synthesis procedures. This challenge becomes more formidable for large scale syntheses, where the colloidal size is usually more difficult to control and the polydispersity of the particles typically increases, both of which can impact the final properties significantly. In the previous chapter, we demonstrated a novel procedure to synthesize magnetic iron oxide nanoparticles (IONPs) as contrast agents for the target application of cross-well electromagnetic imaging. The reaction conditions in that study were optimized for obtaining superparamagnetic IONPs with a high initial magnetic susceptibility with the application of a low strength external field. In this chapter, we will focus on the effects of two different stirring methods on particle size/morphology and finish with a discussion of an alternate colloidal stabilization route.

5.1 The Effect of Agitation Method on the Size and Shape of IONPs

5.1.1 Magnetic stirring

For mass production of magnetic nanoparticles used in ferrofluid applications, the bulk properties of the ferrofluid are strongly affected by the polydispersity of nanoparticles, as well as the colloidal dispersion state. Yet synthesizing magnetic nanoparticles with controlled size and morphology is non-trivial especially given the magnetic nature of the particles. Magnetic stirring plates and stir bars are commonly used for lab scale synthesis, but not surprisingly, this equipment will apply an external magnetic field on the reaction solution, possibly causing inhomogeneous mixing. In our studies, we have observed a correlation between the homogeneity of the reaction solution and the resulting size and

morphology of the nanoparticles. More specifically, by adjusting the stirring conditions for the reaction solution during IONP synthesis, we were able to obtain magnetic IONPs with various morphologies.

In the previous chapter, we demonstrated the successful synthesis of spherical nanoparticles in >50 mL reaction scales using mechanical stirring. However, large agglomerations occurred when the same synthesis (50 ml of reaction solution in a 250 ml round bottom flask) was conducted with magnetic stirring, even though we could still obtain particles with similar magnetic properties to the ones presented in the previous chapter. Furthermore, these aggregates were difficult to stabilize throughout the purification procedure described in the previous chapter and usually precipitated out of solution very easily. This phenomenon was also observed to correlate with the reaction scale. For example, when the reaction was scaled down by a factor of 10, i.e., 5 mL of reaction solution in a 50 mL round bottom flask, the aggregation caused the majority of the particles to precipitate out of solution, yielding only a small amount of colloidally stable IONPs.

We attributed the aggregating behavior to the application of an external magnetic field from the magnetic stir plate and stir bar on the growing magnetic nanoparticles in solution. This caused a concentration gradient in the vertical direction, as is illustrated in **Figure 5.1**. First, an external magnetic field can induce a magnetic moment on the IONPs, resulting in stronger particle-particle interactions in the solution during the nanoparticle growth. This interaction becomes stronger as the size of the primary particles (or nanoclusters/aggregates of several particles) increases, leading to bigger aggregates in the final product. Thus, even though the spinning speed of the stir bar was high enough to macroscopically agitate the entire solution, the particles were inevitably attracted to the bottom of the solution which eventually led to more severe aggregation compared to the

solution near the top. This effect was exacerbated for smaller scale reactions, since the magnetic attraction became stronger for the solution closest to the magnet.

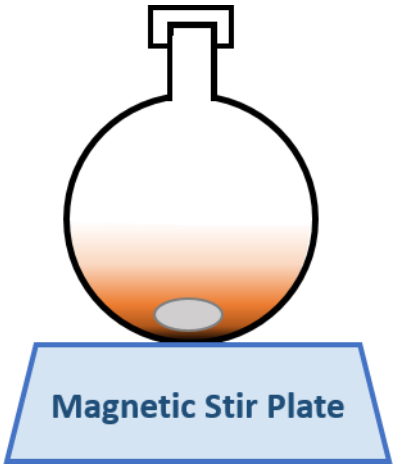

Figure 5.1: Concentration gradient in a reaction solution where magnetic nanoparticles are being formed/grown, which resulted from the use of a magnetic stir plate.

Interestingly, transmission electron microscopy (TEM) images (**Figure 5.2**) of the particles after purification revealed that the sample contained ~50nm spherical nanoclusters composed of a number of smaller primary nanoparticles.

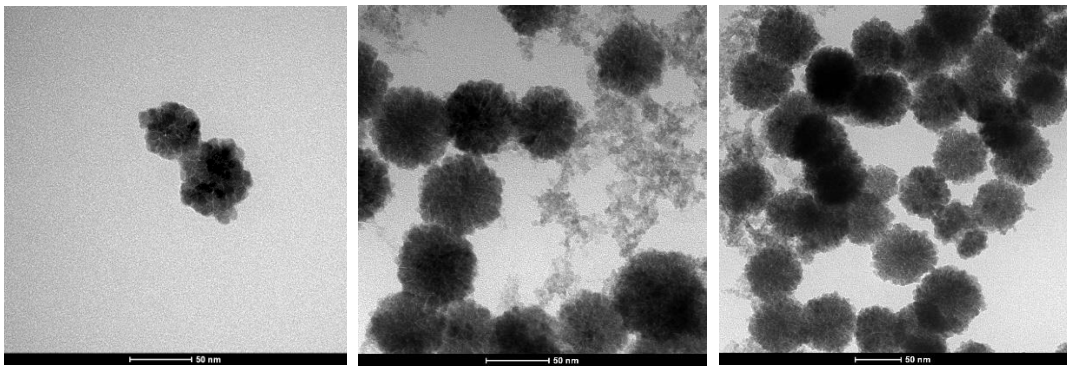

Figure 5.2: TEM images of nanoclusters produced with magnetic stirring. White scale bars are 50 nm.

This morphology was previously observed by Ge et al. In that study, the size of the nanoclusters was controlled by using different amounts of NaOH to accelerate the aggregations of nanoparticles during co-precipitation (**Figure 5.3**).[1] Aggregation/nanoparticle clustering is not uncommon in nanoparticle syntheses and it often occurs during the second stage of nanoparticle growth, after the precursors have decomposed to form nuclei during the first stage of nanoparticle growth following the classic La Mer mechanism.[2,3] However, in our study, the presence of the small primary grain size suggests that the typical second stage particle growth has been interrupted by early stage aggregation. One possible solution is to electrostatically or sterically stabilize the particles with a surface ligand,[4] but these ligands often interfere with magnetic properties (which will be discussed later in this Chapter).

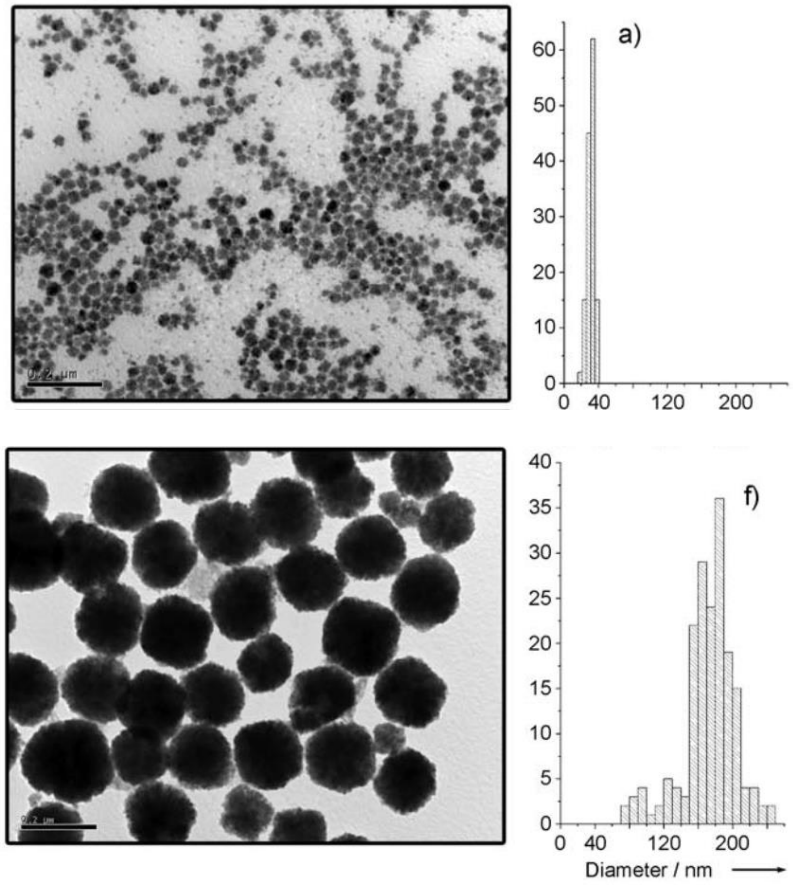

Figure 5.3: TEM images and size distributions of colloidal nanoclusters of different sizes from Ge et al. Scale bars are 200 nm. Reproduced with permission from ref.[1] Copyright © 2007 WILEY-VCH Verlag GmbH & Co. KGaA, Weinheim.

5.1.2 Mechanical stirring

With the goal of achieving a homogeneous particle dispersion, we moved to mechanical agitation in order to eliminate the impact of the external magnetic field from magnetic stirring.

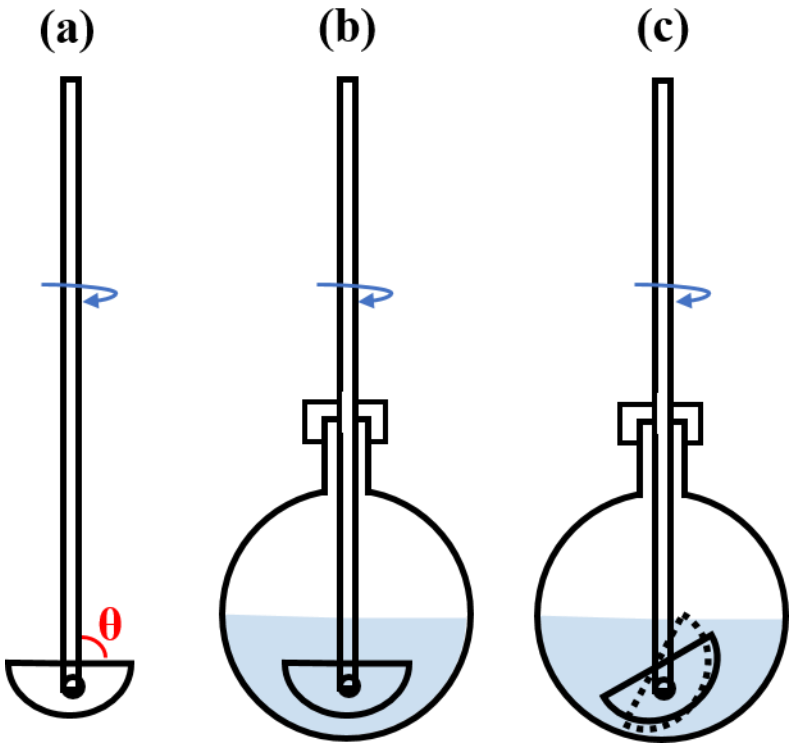

Figure 5.4: Illustrations of the reaction flask equipped with a mechanical stirrer.

During the reaction, the stirring blade was fixed at an angle of θ to the stirring shaft (**Figure 5.4a**). We found that the stirring conditions affected the process of nanoparticle growth to a large extent. When the stirring blade was aligned perpendicular to the stirring shaft (i.e. θ=90°, **Figure 5.4b**), we could reproducibly obtain ~14 nm spherical particles (**Figure 5.5a**) with high yield (>80wt%) as described in the previous chapter. When the stirring blade was tilted, however, we began to observe a combination of morphologies including both spherical and elongated particles (**Figure 5.5b**). At the maximum tilt (θ ca. 0°, **Figure 5.4c**), the synthesized particles were elongated in shape (~50 nm in length and ~5 nm in width). As is shown in **Figure 5.5c**, about every 3-5 nanorods aggregated along

the longitudinal surface to form a bundle. These bundles were randomly oriented while alignment in each bundle was obvious.

Though many prior studies have produced anisotropic magnetic nanoparticles using a variety of techniques, including using lecithin assembly as a template,[5,6] synthesizing particles in a multiphase reaction,[7] and using sonochemistry under an external magnetic field,[8] the mechanism behind this formation is not well understood. In our work, we suspect the position of the stirring blade generates different shear fields in the reaction solution, which controls the nucleation and aggregation of nanoparticles during the reaction. Here, our conclusion is based on two particular studies. One is from Li et al., which discusses the impact of mechanical agitation on the nanoparticle growth leading to different sizes and shapes of the final product.[9] The other study focuses on how the positioning of a stirrer in a reactor, as well as the geometry of the stirrer, can affect the shear field of the reaction solution.[10] Though the results from those two studies cannot be directly applied to our system due to the disparity in chemical and specific flow conditions, our synthesis results did corroborate that the stirring conditions greatly impact the particle morphology.

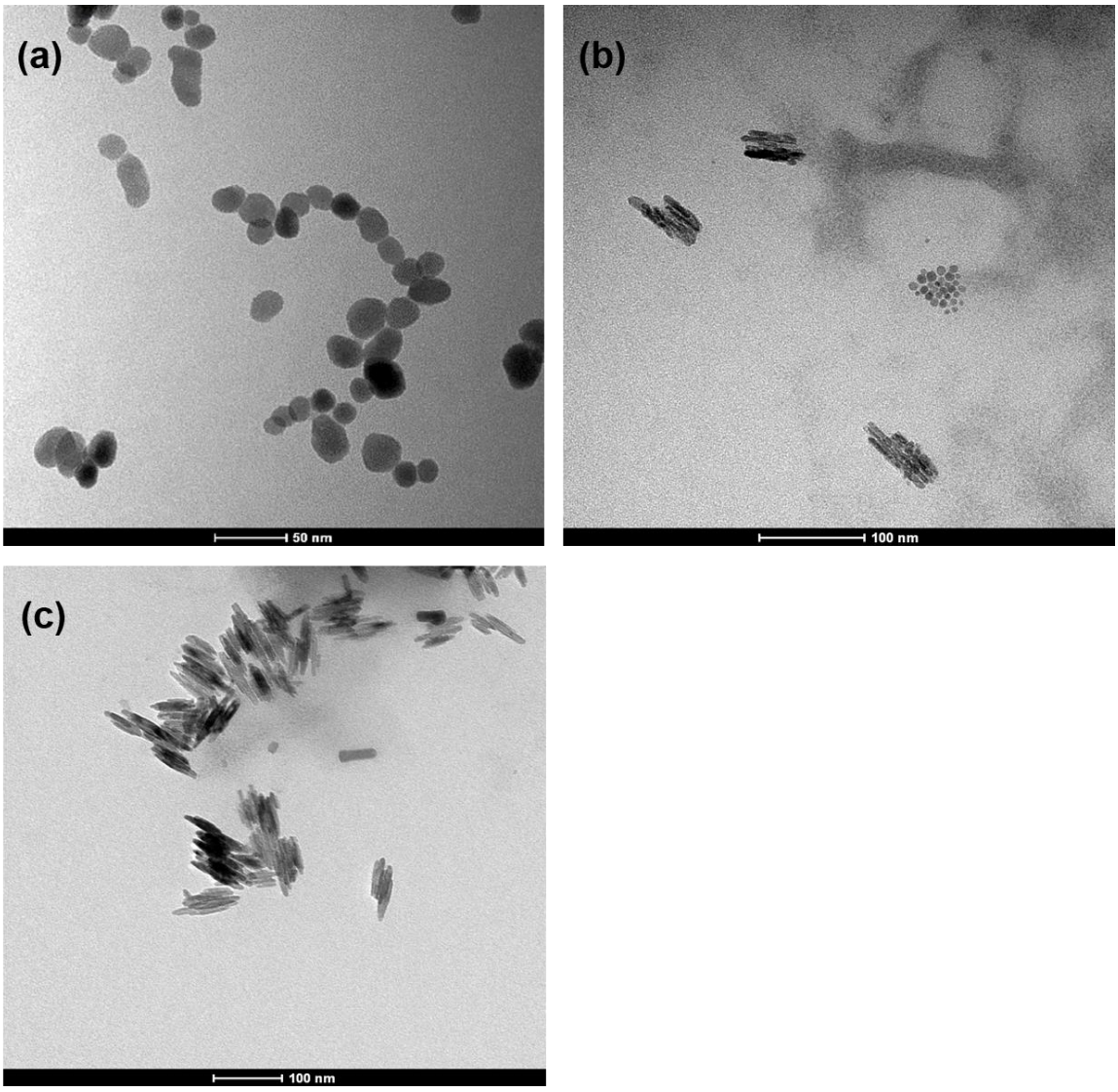

Figure 5.5: TEM images of IONPs of different morphologies synthesized with mechanical stirring when (a) θ~90°, (b) 0°<θ<90°, (c) θ~0°.

In addition to TEM analysis, the corresponding magnetic properties of the particles were measured by vibrating sample magnetometer (VSM). For the largest change in shape (**Figure 5.5c**), the elongated particles had a high initial susceptibility of 2.96 (SI units) at 2 vol% after exposure to a magnetic field (strength up to 3 Oe, **Figure 5.6a**), which is

comparable to our spherical IONPs (3.4 at 2 vol%) from the previous chapter. They also had a high saturation magnetization of 83.2 emu/g Fe_3O_4 (Saturation magnetization of bulk magnetite is 92.8 emu/g Fe_3O_4.) with negligible hysteresis (**Figure 5.6b**).

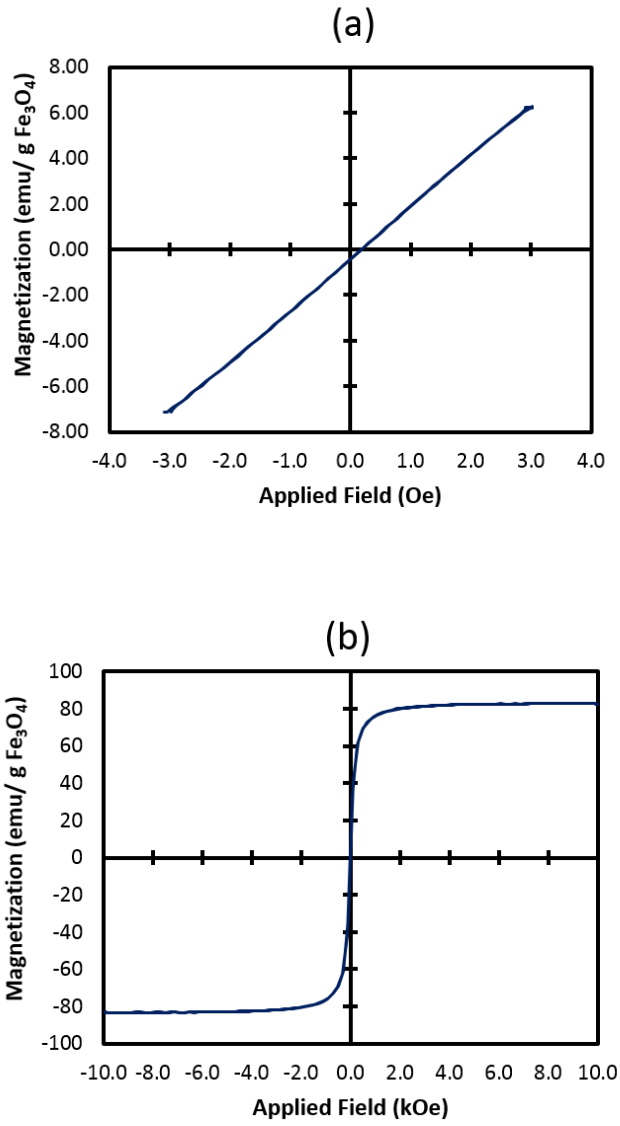

Figure 5.6: Magnetization loops of elongated IONPs synthesized with mechanical stirring (a) up to a 3 Oe external field and (b) up to a 10 kOe external field.

Shape anisotropy or morphology can impact magnetic properties, one of these being coercivity, or the resistance of a magnetic material to changes in magnetization. For example, Huber et al.[11] demonstrated a large increase in coercivity for acicular magnetic particles, a property which has been utilized in the recording industry leading to the largest commercial application of iron nanoparticles.[12,13] This high coercivity, derived from the high-aspect-ratio of the particles, increases the energy required to reverse magnetization, thus minimizing the chance of accidental changes in magnetization which is desired for safe data storage. However, the elongated nanoparticles in our results showed negligible coercivity under an external magnetic field at 300K. We suspect larger sizes or higher aspect ratios of the particles could eventually lead to higher coercivity.[11,14]

In this section, we have demonstrated that different stirring methods have a clear impact on the final morphology of the particles. Magnetic stirring is generally not recommended for synthesizing magnetic nanoparticles due to the resulting inhomogeneity of the solution. Mechanical stirring is preferred with the caution of careful positioning/control of the stirrer relative to the reactor. Our preliminary results additionally show that there are ways to control particle morphologies by adjusting stirring characteristics. The rod-like particles could also be used in an application which could benefit from a high surface area, such as a use which requires subsequent grating reactions and/or self-assembly of nanoparticles.

5.2 Effect of Surface Ligands on the Colloidal Dispersion of IONPs and the Corresponding Magnetic Properties

Electrostatic repulsion can be used to stabilize colloidal nanoparticles. In the case of commercial ferrofluids, the surface properties of the magnetic particles often determine the colloidal stability.[14] In the previous chapter, we coated IONPs with a shell of silica to provide stability through electrostatic repulsion and to enhance surface functionality, while

keeping the silica shell thin enough so as not to diminish the magnetic properties of the core. Here, we instead used a surfactant, trisodium citrate (**Figure 5.7**), as an alternative method to remove IONP aggregations in solution. Trisodium citrate was chosen because, as a water soluble ligand, it is easily adsorbed onto the cationic surface of IONPs and can stabilize the surface with excess negative charge, rendering the IONPs water dispersible. By gradually increasing the concentration of the ligand in the IONP dispersion, we observed the IONP aggregates separating into smaller clusters and, eventually, individual nanoparticles as demonstrated in TEM images (**Figure 5.8a, b**).

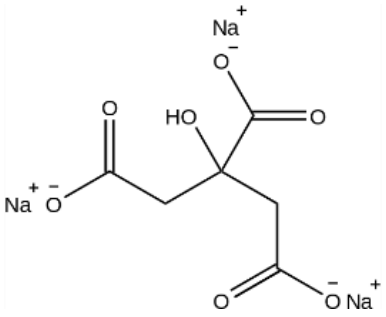

Figure 5.7: Chemical structure of trisodium citrate.

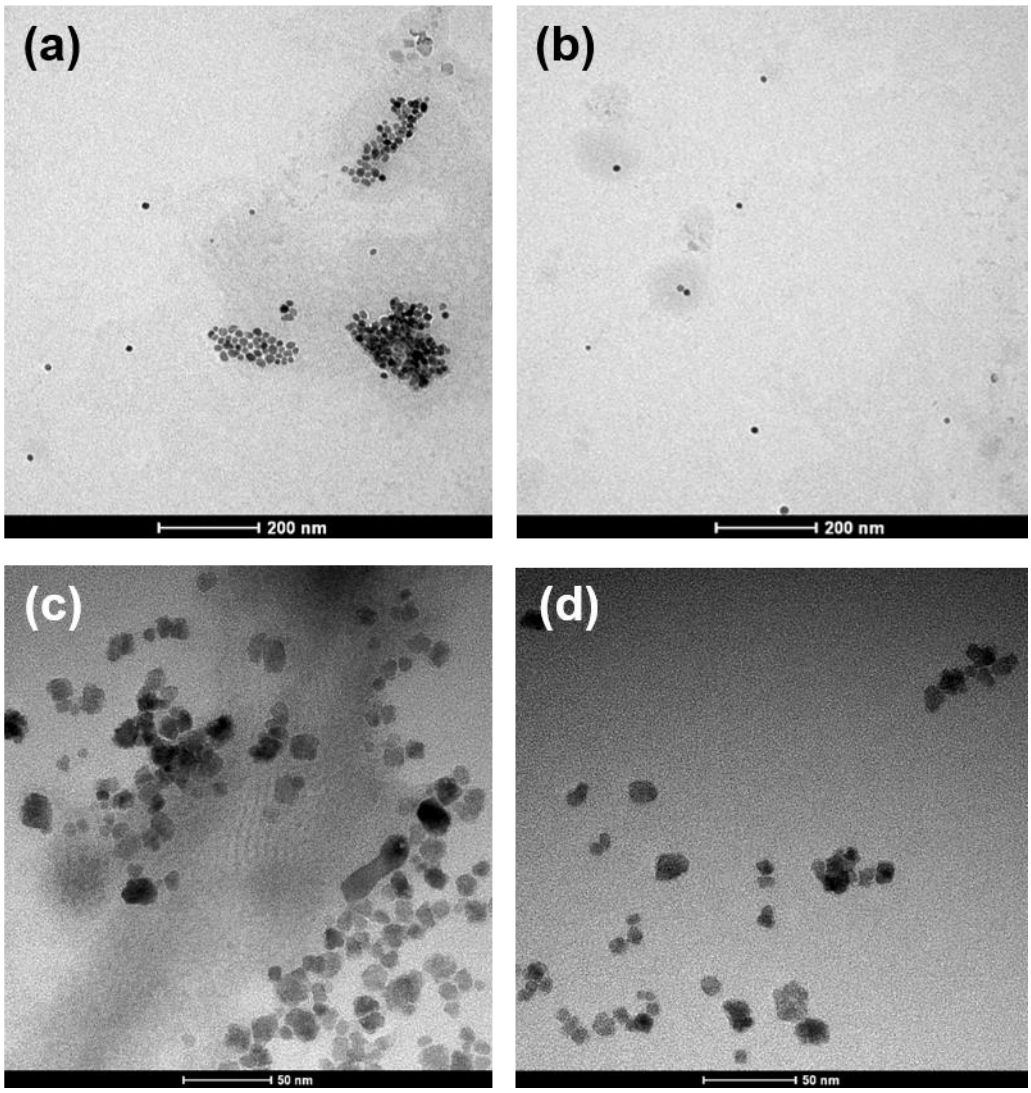

Figure 5.8: TEM images of IONPs. (a) IONPs dispersed in 0.2 wt% trisodium citrate solution, (b) IONPs dispersed in 1 wt% trisodium citrate solution. (c), (d) commercial Ferrotec ferrofluid.

Previous studies have shown that surface coating can actually decrease the magnetization of nanoparticles, and this effect becomes more prominent for smaller particles due to the large surface area/volume ratio.[14,15] This reduction has been associated with surface spin canting, or the existence of a spin-glass-like behaviour of the surface spins.[16] Similarly in our work, while trisodium citrate does offer a more convenient

approach to stablize particles, the magnetic susceptibility was compromised. In contrast, magnetically inert silica coatings are a relatively well studied coating material, and such coatings preserve magnetic properties due to the prevention of dipolar coupling between neighboring particles. The magnetic properties obtained using a silica coating (discussed in the previous chapter) are compared with the current technique using trisodium citrate in **Table 5.1**. We found that while the magnetic susceptibility of trisodium citrate coated IONPs was reduced to 30% of that from particles with a silica shell, the ligand did not significantly impact the saturation mangetization under high field. Unfortunately, not many researchers have quantified the effects of various surface ligands on magnetic properties. In one very recent work, Misra et al. showed citrate ligands, as well as the counterion Na^+, can both have an impact on the mangetic intreactions of coated nanoparticles.[17] Still, more detailed and quatitative work needs to be conducted in order to fully understand the mehcanism behind our experimental results.

Table 5.1: Comparsion of mangetic properties of different IONP colloids

Sample	Initial susceptibility (SI)	Saturation Magnetization (emu/g Fe_3O_4)	Hydrodynamic Diameter by Dynamic Light Scattering (DLS) (nm)
Triethylene glycol (TEG) coated IONP	3.36	85.1	53
Silica coated IONP	3.40	92.9	34
TEG coated IONP + 1 wt% Trisodium Citrate	1.00	87.4	32
Ferrotec Ferrofluid	0.540	88.0	49

5.3 EXPERIMENTAL

5.3.1 Materials

Iron (II) acetate [$Fe(CO_2CH_3)_2$] was purchased from Alpha Aesar. Triethylene Glycol (TEG) ($C_6H_{14}O_4$), tetraethyl orthosilicate (TEOS) [$Si(OC_2H_6)_4$], trisodium citrate dihydrate ($HOC(COONa)(CH_2COONa)_2 \cdot 2H_2O$) were purchased from Sigma Aldrich, USA, and used without further purification.

5.3.2 Synthesis of TEG-coated iron oxide nanoclusters

IONP syntheses were carried out by modifying the procedure reported by Günay et al.[18] IONPs were prepared by the thermal decomposition of iron(II) acetate (light brown powder) in the presence of TEG at 210 °C in an inert argon atmosphere while the stirring was carried out using an overhead mechanical stirrer. In a typical synthesis, 5 grams (28.8 mM) of iron (II) acetate were mixed with 50 mL (333 mM) TEG in a 250 mL three-neck round bottom flask equipped with condenser, mechanical stirrer and a heating mantle. The mixture was purged with argon gas for at least 20 min before ramping up to 210 °C in 20 min, and then refluxed at 210 °C for two hours. Heating was then removed and the reaction was cooled to room temperature. The synthesized IONPs were purified by copious washing with a mixture of ethanol and DI water and ethyl acetate (~2:1:1 by volume) to facilitate separation before centrifuging at 10,000 rpm for 10 minutes. The procedure was repeated at least three times to remove excess TEG. The obtained pellets were redispersed in 1wt% nitric acid and immediately precipitated by adding ethyl acetate followed by centrifugation. The loosely agglomerated pellets were redispersed with DI water to form a stable colloidal dispersion at a final concentration around 10 mg/mL and pH of 3.5.

5.3.3 Silica coating of IONPs

The silica coating was performed by modifying the procedure of Kralj et al.[19] TEG coated IONPs were dispersed in an alkaline media of pH 12 at a concentration of 0.1 wt%. TEOS was diluted with ethanol at a volumetric ratio of 1 : 9 and the mixture was added to the IONPs dispersion over 3.5 hours by a syringe pump during vigorous stirring. The mass ratio of IONPs to TEOS was 0.05. The particles were collected with a strong magnet and washed with copious amounts of DI water. The aqueous dispersion was sonicated using a 400W probe sonicator (Branson, Digital Sonifier 450) at 30% amplitude and centrifuged at 3500 rpm to remove big aggregates. The dispersion was finally concentrated by centrifugal filtration with Amicon Ultracel-10K regenerated cellulose centrifugal filters.

5.3.4 Characterization

5.3.4.1 Flame atomic absorption spectroscopy (FAAS)

The concentration of Fe in the dispersion was measured on a GBC 908AA flame atomic absorption spectrometer (GBC Scientific Equipment Pty Ltd). All measurements were conducted at 242.8 nm using an air-acetylene flame. 100 µL of IONP dispersion (20mg/mL) was digested in 900 µL of 12 M HCl overnight; the volume ratio of HCl: nanoparticle dispersion was 9:1. After digestion, the samples were then diluted with 1 wt% HNO_3 to a concentration between 1 and 5 ppm of Fe. Nanoparticles that were coated with silica or polymer were filtered through a 20 nm pore size syringe filter (Whatman ANOTOP 25). The FAAS was calibrated with ferric nitrate nonahydrate solutions in 1% nitric acid at concentrations from 1 to 5 ppm of Fe. The calibration was repeated every 10 samples. The concentration of the original suspension was calculated in the unit of mg/mL Fe_3O_4 based upon the measured Fe content measurements.

5.3.4.2 Dynamic light scattering (DLS)

Hydrodynamic sizes (D_H) of aqueous dispersions of the as-prepared iron oxide clusters were measured with a Brookhaven ZetaPALS instrument with the ZetaPlus option at a 90^o scattering angle. The collected auto-correlation function curves were fit with the CONTIN routine to give volume-averaged size distributions. All measurements were made over a period of 2 min and at least three measurements were performed on each sample. The concentration of IONPs for DLS samples were adjusted to obtain a count rate of ~500 kcps. The hydrodynamic diameter reported here is the peak value of the main peak that accounts for >70% of cluster volume.

5.3.4.3 Transmission electron microscopy (TEM)

TEM images were acquired on a FEI Tecnai Spirit Bio Twin TEM operated at 80 kV. The samples were prepared by drop casting a dilute aqueous suspension of IONPs onto 400 mesh Formvar coated copper grids. The average diameter was obtained with Image J in which at least 100 primary particles at various spots of the grid were measured.

5.3.4.4 Vibrating sample magnetometer (VSM)

The initial susceptibility of magnetic fluid samples was measured with a VSM (Microsense model EZ7 and EV7) under a magnetic field with intensity swept between -3 to +3 Oe at a rate of 0.15 Oe/s. Saturation magnetization was measured under a -10 kOe to +10 kOe range swept at a rate of 250 Oe/s. All the magnetic fluid samples are measured at 300 K at a DC field with vibration frequency of 75 Hz.

5.4 REFERENCES

(1) Ge, J.; Hu, Y.; Biasini, M.; Beyermann, W. P.; Yin, Y. Superparamagnetic Magnetite Colloidal Nanocrystal Clusters. *Angew. Chemie Int. Ed.* **2007**, *46*, 4342–4345.

(2) LaMer, V. K.; Dinegar, R. H. Theory, Production and Mechanism of Formation of Monodispersed Hydrosols. *J. Am. Chem. Soc.* **1950**, *72*, 4847.

(3) Murray, C. B.; Kagan, C. R.; Bawendi, M. G. Synthesis and Characterization of Monodisperse Nanocrystals and Close-Packed Nanocrystal Assemblies. *Annu. Rev. Mater. Sci.* **2000**, *30*, 545–610.

(4) Mahmoudi, M.; Sant, S.; Wang, B.; Laurent, S.; Sen, T. Superparamagnetic Iron Oxide Nanoparticles (SPIONs): Development, Surface Modification and Applications in Chemotherapy. *Adv. Drug Deliv. Rev.* **2011**, *63*, 24–46.

(5) Cain, J. L.; Nikles, D. E. Preparation of Acicular α-Fe Nanoparticles in Tubular Lecithin Colloids. *IEEE Trans. Magn.* **1996**, *32*, 4490–4492.

(6) Cain, J. L.; Nikles, D. E. Preparation of Acicular Iron Nanoparticles by the Reduction of Ferrous Salt in the Presence of Tubular Lecithin Assemblies. *J. Appl. Phys.* **1996**, *79*, 4860.

(7) Gubin, S. P.; Koksharov, Y. a; Khomutov, G. B.; Yurkov, G. Y. Magnetic Nanoparticles: Preparation, Structure and Properties. *Russ. Chem. Rev.* **2005**, *74*, 489–520.

(8) Prozorov, T.; Prozorov, R.; Koltypin, Y.; Felner, I.; Gedanken, A. Sonochemistry under an Applied Magnetic Field: Determining the Shape of a Magnetic Particle. *J. Phys. Chem. B* **1998**, *102*, 10165–10168.

(9) Li, D.; Kaner, R. B. Shape and Aggregation Control of Nanoparticles: Not Shaken, Not Stirred. *J. Am. Chem. Soc.* **2006**, *128*, 968–975.

(10) Alvarez, M. M.; Zalc, J. M.; Shinbrot, T.; Arratia, P. E.; Muzzio, F. J. Mechanisms of Mixing and Creation of Structure in Laminar Stirred Tanks. *AIChE J.* **2002**, *48*, 2135–2148.

(11) Huber, D. L. Synthesis, Properties, and Applications of Iron Nanoparticles. *Small* **2005**, *1*, 482–501.

(12) Veitch, R. .; Ilmer, A.; Lenz, W.; Richter, V. MP Technology for a New Generation of Magnetic Tapes. *J. Magn. Magn. Mater.* **1999**, *193*, 279–283.

(13) Vereda, F.; de Vicente, J.; Hidalgo-Alvarez, R. Physical Properties of Elongated Magnetic Particles: Magnetization and Friction Coefficient Anisotropies. *Chemphyschem* **2009**, *10*, 1165–1179.

(14) Lu, A.-H.; Salabas, E. L.; Schüth, F. Magnetic Nanoparticles: Synthesis, Protection, Functionalization, and Application. *Angew. Chemie Int. Ed.* **2007**, *46*, 1222–1244.

(15) Batlle, X.; Labarta, A. Finite-Size Effects in Fine Particles: Magnetic and Transport Properties. *J. Phys. D. Appl. Phys.* **2002**, *35*, R15–R42.

(16) Kodama, R. . Magnetic Nanoparticles. *J. Magn. Magn. Mater.* **1999**, *200*, 359–372.

(17) Misra, S. K.; Li, L.; Mukherjee, S.; Ghosh, G. Anisotropic Magnetic Field Observed at 300 K in Citrate-Coated Iron Oxide Nanoparticles: Effect of Counterions. *J. Nanoparticle Res.* **2015**, *17*, 487.

(18) Günay, M.; Baykal, A.; Sözeri, H. Structural and Magnetic Properties of Triethylene Glycol Stabilized Monodisperse Fe3O4 Nanoparticles. *J. Supercond. Nov. Magn.* **2012**, *25*, 2415–2420.

(19) Kralj, S.; Makovec, D.; Čampelj, S.; Drofenik, M. Producing Ultra-Thin Silica Coatings on Iron-Oxide Nanoparticles to Improve Their Surface Reactivity. *J. Magn. Magn. Mater.* **2010**, *322*, 1847–1853.

Chapter 6. Polyelectrolyte Coating of Iron Oxide Nanoparticle Clusters for Enhanced Transport Mobility in High Salinity High Temperature Oil Reservoir Environments

6.1 Introduction

As was described in Chapter 4, the advantageous magnetic properties of iron oxide nanoparticles (IONPs) have made them promising candidates for contrast agents to address current challenges in subsurface electromagnetic imaging. Ideally, when a highly mobile contrast agent is injected into subsurface flow channels, it can reveal fluid movement, composition of the fluid, and the distribution of oil wells located at distances hundreds of meters away underground as long as the contrast agent can be transported through the oil reservoir.[1] However, bare IONPs cannot survive in a typical oil reservoir environment given the high salinities (>1M), elevated temperatures, and the presence of various mineral surfaces.[2,3] The high salinity and high temperatures can accelerate the aggregation of nanoparticles (NPs), while anionic mineral surfaces can cause adsorption of positively charged species; both can lead to severe loss of nanoparticle transport / mobility.[4,5]

At high ionic strength, the electrical double layer on the particle surface becomes thinner and provides weaker electrostatic repulsion between particles. Recently, polymer functionalized IONPs have received significant attention given the greater range of steric repulsion in addition to electrostatic repulsion at high salinity.[6,7] In general, an important prerequisite for polymer coatings to be able to stabilize nanoparticles is that the polymer by itself should be soluble in the same media and not undergo phase separation.[8] A variety of polymers have been studied previously for their solvation status in high salinity aqueous solutions. Nonionic polymeric stabilizers such as polyethylene glycol (PEG), polyacrylamide (PAM), and polyvinyl pyrrolidone (PVP) have been widely used as stabilizers.[9] However, PAM and PVP stabilized nanoparticles tend to aggregate under

physiological (0.15 M NaCl) as well as moderate saline (0.9 M NaCl) conditions, where the Debye lengths become smaller than 1 nm.[10–12] Additionally, PAM and PVP chains collapse leading to agglomeration in the presence of NaCl; thus they do not remain extended when grafted on nanoparticle surfaces.[12] In contrast, ionic polymers, i.e. polyelectrolytes, are more stable (i.e., solubility stability) in water at elevated temperatures compared to nonionic polymers. For example, weakly acidic polyelectrolytes such as polyacrylic acid (PAA) remain soluble in 1 M NaCl at ambient temperatures. However, PAA suffers from easy agglomeration in the presence of divalent cations, (e.g., Ca^{2+}, Mg^{2+}) which are commonly present in oil reservoirs.[13,14] In contrast, sulfonated polymers with low divalent cation binding affinities tend to remain solvated at high salinities and temperatures.[15,16]

Another challenge faced in oil reservoir environments is the broad presence of anionic mineral surfaces. In aqueous environments, there is a strong thermodynamic driving force for cationic species (NP surfaces or polymer coatings) to adsorb onto the often negatively charged mineral surfaces.[17–19] For example, physically adsorbed PAA coating layers on nanoparticles undergo desorption from the nanoparticle surface when exposed to other charged mineral surfaces.[20] In order to prevent desorption of the polymer coating from nanoparticle surfaces, covalently grafted polymers are required in the harsh oil reservoir environment.

Recently, collaborative efforts at UT Austin demonstrated electrosteric stabilization of IONPs in very high salinity American Petroleum Institute (API) brine (8 wt% NaCl and 2 wt% $CaCl_2$) at elevated temperatures (up to 90^oC) using a series of sulfonated random and block copolymers.[21–25] Poly(2-acrylamido-2-methylpropanesulfonate-*co*-acrylic acid) (poly(AMPS-*co*-AA)) random copolymers were found to be effective stabilizers for ~150 nm IONP dispersions at 90 °C for up to 30 days.

Lab scale batch adsorption tests using model silica spheres and crushed berea sandstone provided some insight towards how the particles interact with anionic media in brine. In order to achieve sufficient transport mobility of the INOPs in a dynamic reservoir-mimicking flow environment, optimization of the nanoparticle stabilization and polymer grafting procedure is required.

Herein, following the IONP synthesis protocol presented in Chapter 4, we present an improved approach to synthesize and purify IONPs grafted with the random copolymer poly(AMPS-*co*-AA). These nanoparticles are colloidally stable in API brine at 120 °C and the cluster sizes are smaller than 100 nm, which is about two fold smaller than previous work.[23–25] The polymer chains were grafted onto IONPs via a 1-ethyl-3-(3-(dimethylamino)propyl)- carbondiimidecarbondiimide (EDC) catalyzed amidation reaction. The IONPs were extensively characterized at various stages by thermogravimetric analysis (TGA) to determine organic content, zeta potential measurements to determine the surface charge, and dynamic light scattering (DLS) to determine the hydrodynamic diameter. The improved grafting method, as well as purification by tangential flow filtration (TFF), rather than magnetic separation and centrifugation as used previously,[23,25] reduced the degree of aggregation producing hydrodynamic diameters smaller than 100 nm in API brine. These particles remained colloidally stable even after storage in brine at 120 °C for up to 30 days. In contrast, the nanoparticle diameters were ~150-200 nm in previous studies.[24–26] With smaller, more stable particles and more uniform grafting, the nanoparticle adsorption in crushed Berea sandstone decreased markedly by a factor of 3 compared to our previous work. The ability to decrease nanoparticle adsorption is very important for subsurface applications given the large surface areas in the formations and large quantities of nanoparticles required. When flowing through a consolidated Berea sandstone core, the mass breakthrough increased from 8.7% to 79% corresponding to a

reduction in adsorption/retention from 432 to 266 µg/g respectively. Furthermore, to the best of our knowledge, this is the first study to demonstrate stability of IONPs at 120 °C in API brine using poly(AMPS-*co*-AA).

6.2 Results and Discussion

6.2.1 Synthesis and characterization of IONPs

To covalently attach polymer chains onto nanoparticle surfaces, we chose the 'graft-to' route. Compared to other options such as 'graft-from' and 'graft-through', the 'graft-to' approach has the advantages of a predefined length and composition of the polymer chains, eliminating the need for an uneconomical catalyst and an inert atmosphere, which are often required with surface-initiated polymerization.[27–32] The 'graft-to' approach enabled control of both the initial surface modification and the subsequent polymer synthesis, which is advantageous for scaling up syntheses.[33]

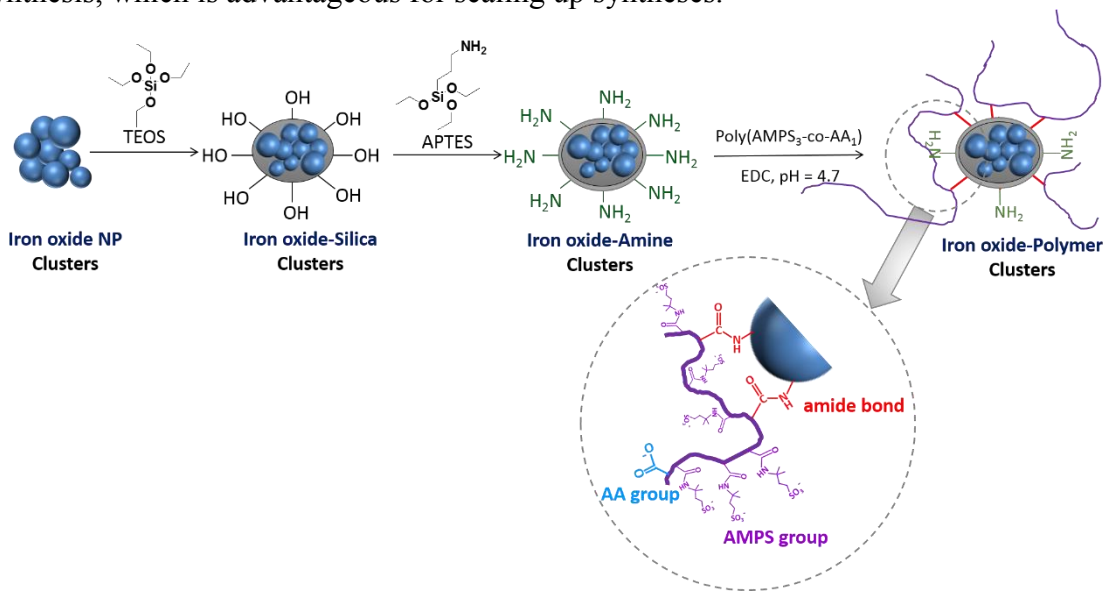

Figure 6.1: Schematic of the surface functionalization and polymer grafting procedure used on the IONPs.

A schematic of the 4-step procedure used to prepare polymer grafted IONPs is shown in **Figure 6.1**. The particle synthesis and silica coating steps are described in detail in chapter 4. In order to graft polyelectrolyte onto the silica coated IONPs, the particles were first coated with a layer of amine groups via reacting with (3-aminopropyl)-triethoxysilane (APTES). In the polymer grafting step, the amine groups were then reacted with carboxylic acid groups in the random copolymer of poly($AMPS_3$-*co*-AA_1) to form covalent amide bonds. The random copolymers were synthesized by free radical polymerization as in previous studies. It has a number averaged molecular weight M_n of 125 kDa and PDI of 1.4 as determined by gel permeation chromatography (GPC). The molar ratio of AMPS to AA units is 3:1 as determined by proton nuclear magnetic resonance (^{1}H NMR).

Table 6.1: Hydrodynamic diameters of 3 batches of IONPs in DI water during various stages of functionalization

Sample #	Hydrodynamic Diameter, nm (Mean, %V)			
	TEG coated IONPs	**Silica coated IONPs**	**Amine coated IONPs**	**Polymer coated IONPs (in API Brine)**
1	34.1	39.6	43.5	61.6
2	24.6	28.9	37.9	46.8
3	27.8	31.3	38.6	52.5

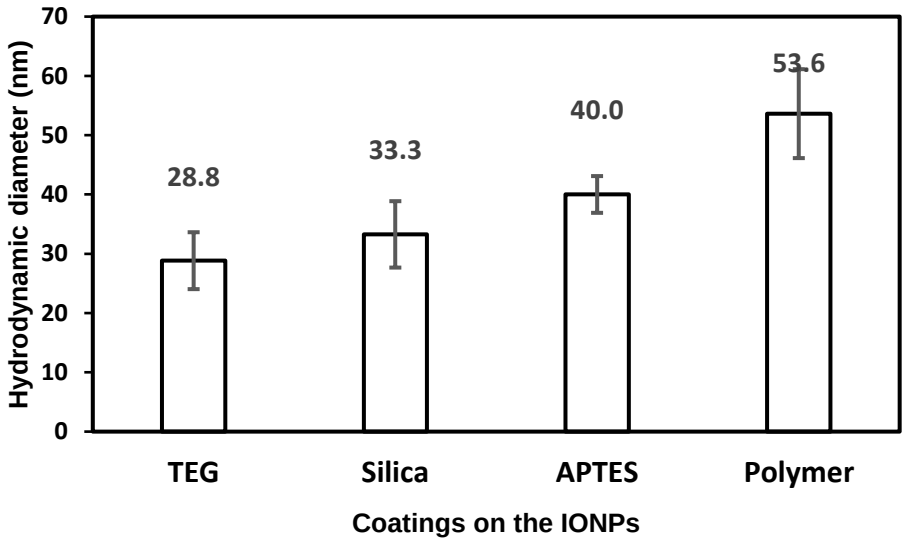

Figure 6.2: Averaged hydrodynamic diameters of the IONPs (**Table 6.1**) in DI water after each coating step as measured by DLS.

The colloidal IONPs were characterized by DLS, zeta-potential measurements and TGA after each coating step. The hydrodynamic volume of the nanoparticle clusters was characterized by DLS (**Table 6.1** and **Figure 6.2**). The hydrodynamic diameters of the clusters in the aqueous phase grew from ~29nm for bare IONPs to ~54nm after polymer grafting (**Table 6.2**), indicating minor aggregation (~2-3 times that of the primary particle size).

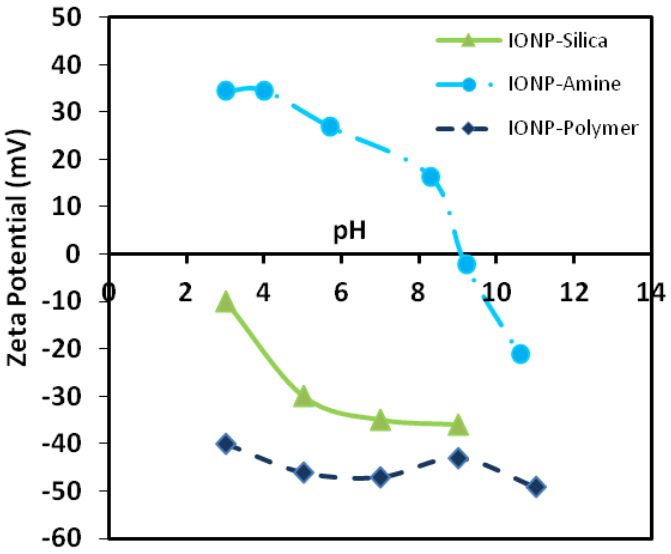

Figure 6.3: Zeta potential of IONPs during various stages of synthesis; after silica coating, APTES functionalization (denoted amine) and polymer grafting. The samples were prepared in 10mM KCl.

Zeta-potential measurements of the particle solution were performed after each coating step in order to evaluate the colloidal stability of the clusters. For silica-coated particles, deprotonation of the acidic silanol (Si-OH) groups led to a zeta potential lower than -30 mV from pH 4 to 12 and an isoelectric point near pH=2, indicating good silica coverage (**Figure 6.3**). We have also examined that the silica coated colloidal IONPs could remain stable in DI water at room temperature for more than 12 months. After the APTES coating, the zeta potential increased to a maximum of +30 mV at ~ pH 5 due to protonation of the amine groups and the isoelectric point is around pH 9. Solutions required probe sonication (at pH~5) in order to ensure the colloidal dispersion remained stable during storage. After polymer grafting, the colloids (with a D_H of ~53 nm) maintain a zeta-potential lower than -40mV from pH of 2 to pH over 10, indicating significant electrostatic repulsion was provided by negatively charged polyelectrolytes. Monitoring the evolution of the electrostatic repulsion of bulk colloids provided useful information regarding proper

storage of the particles as well as indicating the proper reaction pH for the nanoparticles at different coating stages.

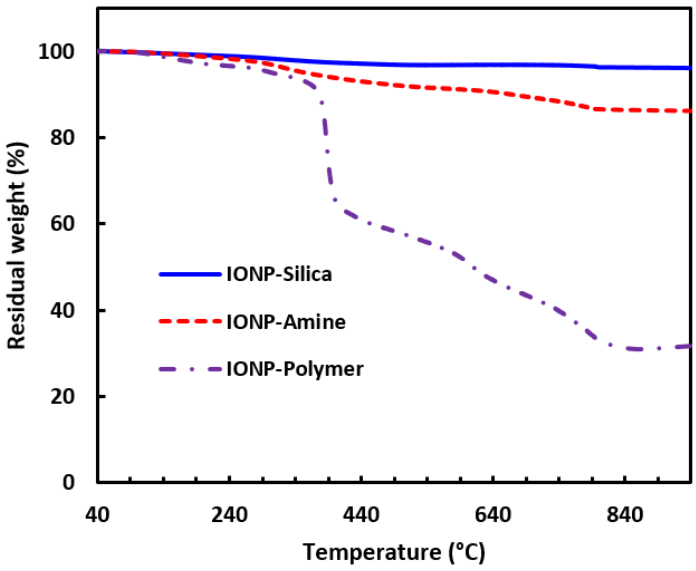

Figure 6.4: TGA of IONPs during various stages of functionalization: silica, APTES and after polymer grafting.

TGA experiments were performed under nitrogen to evaluate the mass ratio of surface coating or polymer grafting on the IONPs (**Figure 6.4**). All samples were purified with a copious washing process to remove unreacted small molecules and dried under vacuum prior to the test. For silica coated IONPs, there is a weight loss of 6.4 ± 0.7%, which was attributed to strongly adsorbed water on the silica layer. Upon APTES addition, the total weight loss was 13.2 ± 1.0% arising from the release of water and degradation of aminopropyl groups in the surface coating. After the polymer grafting step, the net weight loss from polymer, water, and propylamines was 43.3 ± 3.5%, corresponding to 32 wt% of polymer content.

Numerous efforts have been devoted to the development and optimization of the multi-step coating procedure, which is available in the following publications.[23,25,34] The main goal is always enhancement of the colloidal properties to obtain high particle mobility in high salinity, high temperature applications. In the current batch (shown in **Figures 6.3 and 6.4**), for each coating step, adjustments were made to ascertain optimal pH conditions, choice of catalyst, and concentration of each reactant in solution.

Table 6.2: A comparison of typical hydrodynamic diameters of IONPs synthesized via co precipitation vs TEG IONPs at various steps of synthesis at ambient temperature

Coating status	**Hydrodynamic diameters (nm), (Cumulative, %V)**		
	Batch1 (no silica coating, EDC catalyzed grafting)[23]	**Batch 2 (Silica coating, thermal grafting)[25]**	**Current Batch (Silica coating and EDC catalyzed grafting)**
IONP-TEG	22.9±1.5	22.9±1.5	28.8±4.8
IONP-Silica	N/A	30.0±2.0	33.3±5.6
IONP-Amine	55.0±7.0	97.0±2.0	40.0±3.1
IONP-Polymer (in API Brine)	165±24	156±5	53.6±7.5

Compared with Bagaria's first successful polymer coating on IONPs synthesized by co-precipitation and Urena's thermal grafting procedure (**Table 6.2**), several modifications were made in the current work's 4-step procedure. First, the particles were coated with a layer of silica prior to amine functionalization. This additional step enhanced the amine density by 2.5 times, as revealed by conductometric titration results, compared to the previous 3-step procedure without the silica coating step. The reactivity of TEOS with an iron oxide surface is much higher than that of ATPES molecules.[35] With the aid of

the silica shell, APTES grafting became more efficient, which provided more amine functional groups for subsequent polymer grafting. In this work, we pre-oligomerized the APTES molecules before attaching them onto the IO surface in order to promote the efficiency of amine functionalization. Conductometric titration was used to confirm the surface amine density. The conductivity, which is a function of the concentration of charge carriers (ions) in the solution, of the suspension of IONPs were measured as a dilute IONP solution ($c < 0.05$ mg/mL Fe_3O_4) was being titrated with 0.01N HCl (**Figure 6.5**). As is shown by the conductivity curve, the conductivity first went down as the base (NaOH) was being neutralized, then increased slowly as the HCl was being consumed by reacting with surface amino groups, and eventually started to increase at a faster rate with continuous acid addition after all the surface amino groups had been reacted. By determination of the two points on the curve where the slopes changed, the actual amount of HCl consumed in neutralization of surface amino group can be quantified and calculated to a surface amine density using the surface area of the IONP clusters. The surface amine density of the amino-silica coated particles was 3.56 ±0.5 μmol/mg IONPs, which corresponds to 38 ± 3 μmol/m^2 and 22.8 ± 1.5 amines/nm^2 based on the cluster diameter of 34.2±3.8 nm.

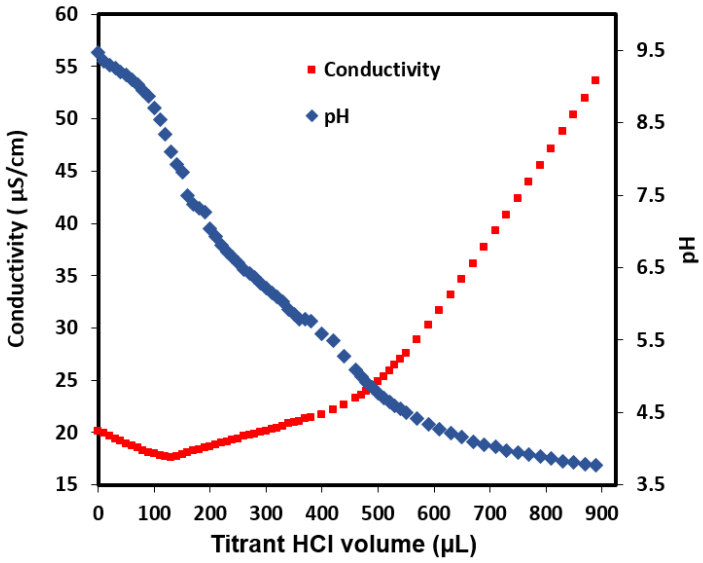

Figure 6.5: Conductometric titration of amine coated IONPs with 0.01N HCl.

Next, for the covalent attachment of poly(AMPS-*co*-AA) onto the IONPs, we focused on both the 'grafting to' approach with the aid of the EDC catalyst to facilitate amide bond formation.[36] In contrast to our previous work using EDC catalyzed polymer grafting onto IONPs, modifications were made to improve the grafting efficiency as follows: (i) the synthesized polymers were purified thoroughly by 3-day dialysis to remove unreacted monomers and small oligomers which could have a huge impact on the total polymer grafting efficiency. The amount of IONP and polymer used for grafting reaction is calculated based on a 1:3 molar ratio of surface amine groups to the available AA groups in poly(AMPS-*co*-AA), (ii) the mixture of polymer solution and amine coated IONPs were bath sonicated prior to the addition of EDC, (iii) A 20wt% NaCl salt solution was added after the addition of EDC (ca. 15 min) in order to reach a total salt concentration of 3wt% in the reaction solution, and (iv) the reaction mixture was bath sonicated again for 90 minutes and then mixed overnight using a magnetic stirrer.

The modification of the coating procedure led to the following improvements in the final polymer coated IONPs. Our previous work has reported a composition of ~9% polymer component in the final particle products (Batch 1: no silica coating, EDC catalyzed polymer grafting).[23] The thermal grafting approach with silica coating (Batch 2) reported 23 wt% polymer in the final particle products.[25] The current batch following the 4-step coating procedure results in 3.5 times higher polymer content than previous Batch 1 and 1.4 times higher than Batch 2. It is hypothesized that the increased polyelectrolyte content is the key contributor to the improved colloidal stability and transport properties, which will be discussed below.

6.2.2 Stability of poly(AMPS-*co*-AA) coated IONPs in API brine

The colloidal stability of poly(AMPS-*co*-AA) grafted IONPs was investigated at room and elevated temperatures in API brine by DLS (**Table 6.3**). The polymer grafted IONPs formed stable and clear dispersions in API brine at room temperature without showing any signs of settling. Furthermore, the IONPs exhibited unprecedented stability at 120 °C without any settling or precipitation for a month, after which the studies were discontinued. This is the first time that long term stability of nanoparticle clusters in API brine at 120 °C was demonstrated.[23,25,37] The stability of the IONPs indicates that the polymer chains remained solvated in brine and provided steric stabilization.

Table 6.3: Stability of polymer grafted IONPs at 120 °C in API Brine as characterized by the volume averaged diameter distribution via DLS

Batch	Hydrodynamic Diameter (nm), (Mean, %V)									
	DI RT	**API RT**	**DI 1 week**	**API 1 week**	**DI 2 week**	**API 2 week**	**DI 3 week**	**API 3 week**	**DI 4 week**	**API 4 week**
1	55.5	48.0	65.8	52.6	67.5	73.5	80.0	92.0	118.2	103.5
2	52.0	40.4	82.0	58.7	63.9	69.7	74.1	87.0	104	98.5

To further investigate whether poly(AMPS-*co*-AA) chains were covalently grafted, or physically adsorbed onto the nanoparticle surfaces, aggressive dilution tests were performed. The IONP dispersion was diluted 20,000 times in DI water and allowed to sit overnight. After dilution, the sample was still stable at 120ºC in API brine with no appreciable change in diameter (**Table 6.4**). In an extremely diluted solution, the polymer chains would likely be forced to desorb from the nanoparticle surface if they were only physically adsorbed. Thus, the observed stability of IONPs after extreme dilution supports covalent grafting of polymer chains onto the IONPs. Direct proof of amide bonding between polymer chains and the nanoparticle surface is difficult to detect due to the existence of large number of amide bonds in the side chains of poly(AMPS-*co*-AA). As a control experiment, poly(acrylic acid) homopolymer was attached to the nanoparticle surface using the same EDC reaction, and amide bond formation was detected by FTIR.[23] Therefore, it is reasonable to conclude that poly(AMPS-*co*-AA) was covalently grafted onto nanoparticle surface in our case. Furthermore, the fact that these nanoparticle clusters were able to remain stable under high temperature and high salinity for a long period of

time suggests that even if the long chain polymers are grafted at more than one point per chain, multi-point grafting is still robust enough to survive the harsh environment.

Table 6.4: Hydrodynamic diameter of IONPs before and after dilution test in API Brine

Sample #	Hydrodynamic Diameter (nm)	
	Before Dilution (in API Brine)	**After Dilution (in API Brine)**
1	52.5	58.6
2	61.6	68.3
3	46.8	53.2

6.2.3 Batch adsorption of poly(AMPS-*co*-AA) grafted IONPs on model silica

In order to evaluate the degree of interaction between our polymer coated IONPs with subsurface reservoir media with charged surfaces, batch adsorption tests were designed and conducted with 8 μm model colloidal silica at room temperature and pH 8 in standard API brine. As shown in **Figure 6.6**, the color of silica remained very light compared to the solution, which is a qualitative indication of low adsorption levels, considering that magnetite is a very strong inorganic pigment. More quantitatively, the specific adsorption of IONPs onto silica was negligible for all IONPs concentrations tested as shown in **Table 6.5**. In lab scale adsorption tests, we have improved the adsorption level by two orders of magnitude from previous batches of IONPs listed in **Table 6.2**.

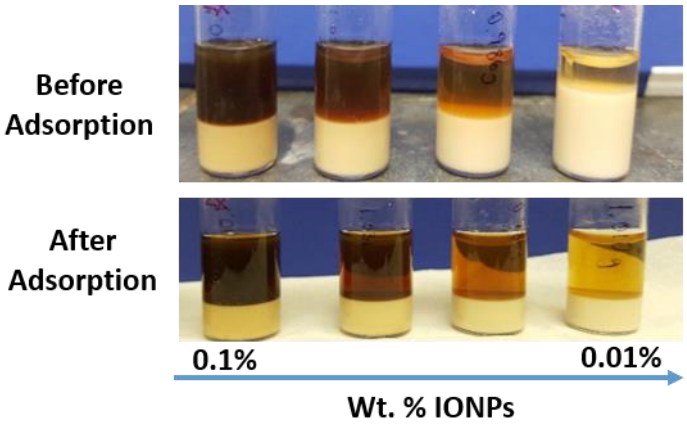

Figure 6.6: Batch silica adsorption test of poly(AMPS-*co*-AA)-grafted IONPs in API brine at pH 8.0 and ambient temperature.

Table 6.5: Batch silica adsorption results for IONPs in API brine at pH 8.0 and ambient temperature

Starting IONP Wt. (%)	% IONP Adsorbed	Mass IONP Adsorbed / Surface Area (mg/m^2)
0.100	<0.01	<0.01
0.050	<0.01	<0.01
0.029	<0.01	<0.01
0.016	<0.01	<0.01

The low adsorption of the nanoparticles on the mineral surfaces is a result of the strong steric repulsion as a consequence of the extension of the polyelectrolyte chains from the surface even in the high salinity brine. It was shown that poly(AMPS-*co*-AA) grafted nanoparticles retain about half of their electrophoretic mobility even with 380 mM Na^+ and 50 mM Ca^{2+}, suggesting the Ca^{2+} did not bind all the sulfonate groups even at high ionic strength.[23] Furthermore, the hydrodynamic diameter of pure polymer electrolyte (tested by DLS) remained ~10nm in either DI water or API brine at both 25 and 90 ^oC, indicating

little chain collapsed Thus, the polymer chains provided a significant degree of electrostatic as well as steric repulsion.

6.2.4 Transport properties of polymer grafted IONPs by dynamic column experiments through unconsolidated porous media

To investigate the mobility of IONPs through porous media in the presence of API brine, a series of column studies were conducted by our collaborators from Dr. Kurt Pennell group at Tufts University using IONPs in crushed Berea sandstone as summarized in **Figure 6.7** and **Table 6.6**. Crushed Berea sandstone is a more retentive media due to presence of liberated clay fines and is thus considered to be a greater challenge than the silica microspheres during batch adsorption tests (e.g., like those in the previous section) or intact rock core experiments. Compared with our earlier batches tested under the same flowrate and substrate conditions, the current particles exhibited lower retention by 2 orders of magnitude.[34] In **Figure 6.7** and **Table 6.6**, the crushed Berea sandstone column study results of the particles made with 3 different methods are compared. The transport mobility of the particles is indicated by retention. Our results reveal that the retention can be greatly reduced by a decreased cluster size and a higher polyelectrolyte coating content. However, it is likely that the latter has a bigger impact, as is indicated by the comparison of Batch 1 and Batch 2 where the polymer content in Batch 2 is 2.6 times higher than Batch 1 with only slightly different cluster size. As was mentioned earlier, without the silica coating step, the amine density in Batch 1 is 2.5 times lower than that in Batch 2, providing much fewer grafting sites for the subsequent polymer attachment. The current batch made via the 4-step coating procedure yielded a great enhancement in the IONP transport mobility in API brine, as is showed by 0.018 mg/m^2 retention in crushed Berea sandstone. Polymers and surfactants have been employed widely in petroleum industries to modify flow viscosity and enhance oil recovery.[26] In order to further improve the mobility of our

polymer coated IONPs, the flow test with our latest batch was also performed by pre-flooding the column with hydroxyethyl cellulose (HEC-10) polymer solution prior to injection of the polymer grafted IONPs (**Table 6.6**). This pre-flood further reduced the retention to 0.007 mg/m^2, and enhanced the total mass breakthrough to 84% from 56% when HEC-10 was not used. The improvement was attributed to the effect of HEC-10 acting as a sacrificial polymer by blocking adsorption sites on the surface of crushed Berea sandstone.[26]

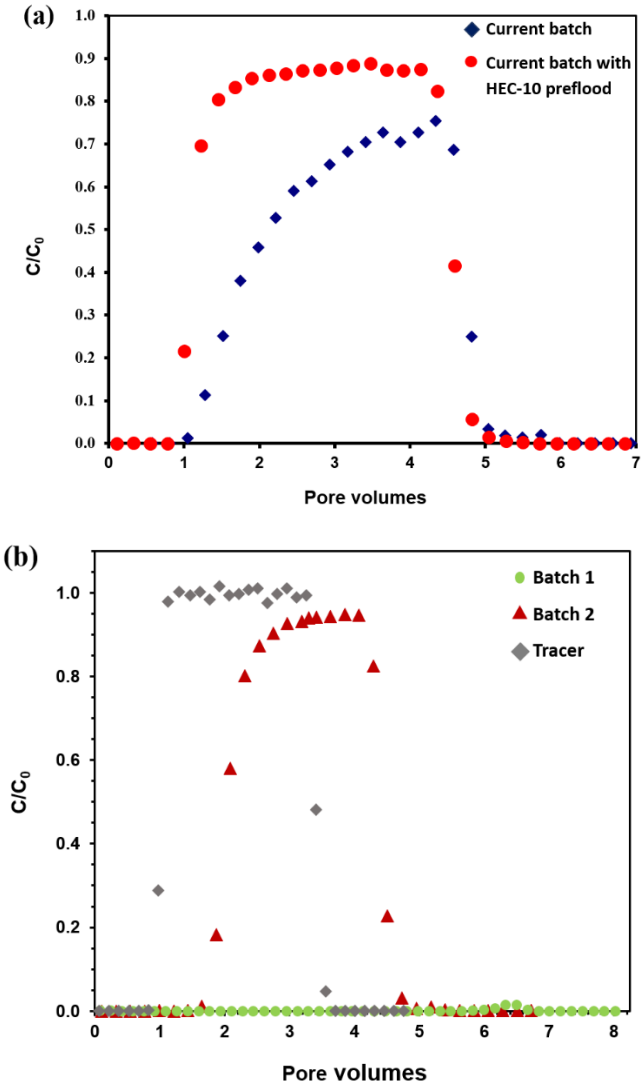

Figure 6.7: Mobility of different batches of poly(AMPS-*co*-AA)-grafted IONPs in columns packed with crushed Berea sandstone (60-170 mesh, unwashed). Mobile phase is API brine at room temperature (23±1°C) and pH 7. Data is plotted as concentration exiting the column relative to the injected concentration as a function of how much mobile phase has gone through the column. Injection occurs at '0' pore volumes. **(a)** Current batch synthesized via 4-step procedure. Input concentration 1,000 mg Fe_3O_4/L. **(b)** Previous Batch 1 and Batch 2. Input concentration 2,500 mg Fe_3O_4/L.

Table 6.6: Dynamic column experimental results of poly(AMPS-*co*-AA) grafted IONPs in unconsolidated porous crushed Berea sandstone media

IONP batch	DLS diameter (nm)	Polyelectrolyte content (wt%)	C_0 IONP (mg Fe_3O_4/L)	HEC-10 pre-flood (mg/L)	Retention (mg/m^2)
Batch 1	165	9	2500	0	0.18
Batch 2	156	23	2500	0	0.05
Current Batch	52	32	1000	0	0.018
Current Batch with HEC-10 pre-flood		32	1000	1000	0.007

Media = Crushed Berea Sandstone (60-170 mesh, unwashed), Specific surface area = 22.54 m^2/g. Injection rate = 1.78 mL/min, pore-water velocity = 13 m/day. Mobile phase is API brine at room temperature.

6.3 CONCLUSIONS

Water dispersible IONPs were synthesized through the thermal decomposition method in TEG then successfully grafted with poly(AMPS-*co*-AA) for enhanced colloidal stability and transport properties. A uniform and enhanced polymer grafting density was achieved by optimizing the surface modification of bare IONPs by first forming a silica shell on the particles then using EDC catalyzed amidation between APTES attached to the silica shell and polymer chains. The improved grafting procedures provided a larger polyelectrolyte content of 32 wt% on the final particles, 3.5 times higher than the previous EDC grafting approach (without silica shell) and 1.4 times higher than the previous thermal grafting approach. The polymer grafted IONPS were colloidally stable with a hydrodynamic diameter smaller than 100 nm for a month in oil reservoir-mimicking conditions, i.e. 120 °C in standard API brine.

Regarding interaction with mineral media present in an oil reservoir, the polymer grafted IONPs exhibited negligible adsorption on model silica in our lab scale batch tests.

The behavior is attributed to efficient covalent grafting of poly (AMPS-*co*-AA) chains on the nanoparticle surfaces which provided electrosteric stabilization between the nanoparticles and weakened interactions of the nanoparticles with anionic silica. This behavior was enabled by the low affinity of Ca^{2+} to the highly acidic AMPS monomers thus enabling strong solvation of the grafted polymer in API brine. In dynamic flow tests through crushed Berea sandstone, polymer grafted IONPs exhibited reduced retention of 0.018 mg/m^2 with a total mass breakthrough of 56%. The mobility can be further enhanced by using a pre-flooded sacrificial polymer HEC-10 (0.1 %v/v) to achieve a lower retention of 0.007 mg/m^2 with a higher mass breakthrough of 84%. Overall, by optimizing the surface modification of bare IONPs and successful grafting of stable polyelectrolytes, we have obtained IONPs with smaller cluster size and a higher polymer content on the surface, resulting in significant improvement in transport mobility in conditions resembling underground oil reservoirs.

6.4 EXPERIMENTAL

6.4.1 Materials

Iron (II) acetate (Fe(C2H3O2)2; MW=173.93), and triethylene glycol (C6H14O4; MW= 150.17) were purchased from Fisher Scientific, USA, and used without further purification. Tetraethyl orthosilicate (TEOS), 3-amniopropyl triethoxy silane (APTES), glacial acetic acid, N-(3-(dimethylamino)propyl)-N′-ethylcarbodiimide hydrochloride(crystalline) (EDC), N-hydroxysuccinimide (98%) (NHS), calcium chloride dihydrate, sodium chloride, hydrochloric acid, sodium hydroxide, acrylic acid, potassium persulfate, and sodium metabisulfite were obtained from Sigma-Aldrich (St. Louis, MO) and Fisher Scientific (Pittsburgh, PA) and used as received. The monomer 2-amino-2-methylpropanesulfonate (AMPS) was a gift from Lubrizol corporation and used as

received. Uniform 8 nm silica microspheres with the trade name Angstrom Sphere Monodispersed Silica Powder (Catalog #SIO2P800-01-1KG) were purchased from Fiber Optic Inc. (New Bedford, MA), and were washed at least five times with pH 9 water and dried at 80 °C before use.

6.4.2 Synthesis of poly($AMPS_3$-*co*-AA_1)

Synthesis of poly($AMPS_3$-*co*-AA_1). A three-necked round-bottom flask equipped with a magnetic stir bar, a nitrogen inlet and a reflux condenser was charged with 30.9 g (0.135 mol) of AMPS monomer, 4.86 g (0.018 mol) of potassium persulfate and 3.42 g (0.018 mol) of sodium metabisulfite under an atmosphere of argon. The flask was sealed with a rubber septum and 180 mL of deionized water that was previously degassed by bubbling with argon for 30 min was added via a cannula to the reaction flask. With stirring, 3.0 mL (0.044 mol) of acrylic acid was added to the reaction flask via an argon-purged syringe. The total monomer concentration at the start of the reaction was 1.0 M. The flask was placed in an 80 °C oil bath and stirred at that temperature under argon for 16 h. The reaction mixture was then cooled to room temperature then transferred into Fisherbrand regenerated cellulose dialysis tubing (Norminal MWCO=3,500). The dialysis was carried out in DI water bath for 3 days. Fresh DI water was changed every 24 hours. The final solution was dried under reduced pressure to remove water and the final result was in the form of white powder. Aqueous GPC was used to determine molecular weight and polydispersity index. ^{1}H NMR was used to determine the ratio of the two monomer units.

6.4.3 Amine functionalization of silica coated IONPs

Aqueous APTES coating was employed to introduce amine groups on the surface of TEOS coated IONPs (refer to Chapter 4) following our earlier procedure.[25] Briefly, 25 mL APTES was mixed with 250 mL 5 wt. % acetic acid solution and allowed to

oligomerize for 20 min under acid hydrolysis. The pH was raised to 8 with 1N NaOH and then silica coated IONPs were added. The reaction concentration was 5 mg IO/mL. After 12 h heating at 65 °C in a water bath, the reaction mixture was cooled to room temperature and the pH was adjusted to 5.0 with 1N HCl. The sample was bath sonicated for 30 minutes and then purified by using a TFF composed of 30 KDa MWCO PES hollow fibers in diafiltration mode.

6.4.4 Polymer grafting of amine functionalized IONPs

The amine functionalized IONPs were grafted with poly(AMPS-*co*-AA) by using a modified approach from our previously published procedure.[34] The polymer, poly(AMPS-*co*-AA), was first dissolved in DI water to make a 10% solution and the pH was adjusted to 5.0 using 2.5 N NaOH. The concentration of APTES functionalized IONPs to be grafted was maintained close to 5 mg/mL and were bath sonicated in an ice-bath for at least 30 minutes prior to grafting reaction. In a typical synthesis, 1 mL of 10 wt. % poly(AMPS-*co*-AA) was taken in a 5 mL glass vial and placed in a bath sonicator. To the polymer solution, 2 mL of APTES functionalized IONPs were added dropwise over a period of 2 minutes under constant sonication. To this reaction mixture, 27.63 mg (0.14 mmol) of EDC (AA:EDC =1:1 molar ratio) was added and the pH was adjusted to 5.7. After 15 minutes of sonication, 0.5 mL of 20% NaCl (such that the final NaCl concentration in solution is 3 wt. %) was added to lower the electrostatic repulsion between the polymer chains to facilitate grafting. The bath sonication was continued for another 90 minutes after which the reaction vial was transferred to a stir plate and continued stirring for overnight at room temperature. The reaction was scaled up accordingly for synthesis of polymer grafted IONPs while keeping the ratios of polymer to IONPs and EDC the same.

The polymer grafted IONPs at large scale were purified using TFF composed of 300 KDa MWCO PES hollow fibers in diafiltration mode followed by concentration.

6.4.5 Characterization

6.4.5.1 IO concentration measurements

The IO concentration was determined by FAAS. At least 100 μL of IONP dispersion was digested in 12 M HCl overnight; the volume ratio of HCl:IONP was 9:1. After digestion the digested samples were then diluted with 1% HNO_3 to a concentration between 1 and 5 ppm of Fe. Particles that were coated with silica or polymer were filtered through a 20 nm syringe filter (Whatman ANOTOP 25). The FAAS was calibrated with ferric nitrate nonahydrate solutions in 1% nitric acid at concentrations from 1 to 5 ppm of Fe. The calibration was repeated every 10 samples. The concentration of the original suspension was calculated in terms of mg/mL Fe_3O_4 based upon the Fe content measurements.

6.4.5.2 Dynamic light scattering (DLS)

Hydrodynamic sizes (DH) of aqueous dispersions of the as-prepared iron oxide clusters were measured in DI water and API brine with a Brookhaven ZetaPALS instrument with the ZetaPlus option at a 90o scattering angle. The collected auto-correlation function curves were fit with the CONTIN routine to give volume-averaged size distributions. All measurements were made over a period of 2 min and at least three measurements were performed on each sample. The concentration of IONPs for DLS samples were adjusted to obtain a count rate of ~500 kcps. The hydrodynamic diameter reported here is the peak value of the main peak that accounts for >70% of cluster volume.

6.4.5.3 Zeta potential measurements

Electrophoretic mobility of different types of clusters was measured with a Brookhaven Zeta PALS instrument at a 15o scattering angle at room temperature in 10 mM KCl solution (Debye length = 3 nm). 10 measurements with 30 electrode cycles for each run were performed and data were averaged. Zeta potential was obtained from the electrophoretic mobility using the Smoluchowski model.

6.4.5.4 Conductometric amine titration

The amount of surface amines was determined by conductometric titration, following an earlier report.[38] 200 μL of amine coated IONPs were diluted in 50 mL of DI water and the pH adjusted to 10 with 1N NaOH. The conductivity and pH of the suspension was measured as it was titrated with 0.01N HCl. The amine content was calculated from the HCl volume used in the intermediate region of the titration curve.

6.4.5.5 Gel permeation chromatography (GPC)

GPC was used to obtain the polymer molecular weights and polydispersity indicies, using an Agilent 1100 series GPC (Agilent Technologies, USA) equipped with Wyatt-864-TS Light Scattering Detector, Wyatt-1015-TREX Refractive Index Detector, and GPC columns of Jordi Sulfonated Plus 500Å (250 mm x 10mm) and Mixed Bed (250 mm x 10mm) in series. Bovine albumin serum (BSA) was used as calibration standard. The GPC eluent is a mixture of acetonitrile and water (1:3 by volume) with addition of 0.1M sodium acetate to reduce ionic interactions between the samples and columns. A dn/dc of 0.1021 (mL/g) in this eluent was determined experimentally by plotting the integrated refractive index signal for the poly(AMPS-*co*-AA) copolymer peak for various sample concentrations and extracting the slope. The dn/dc value was used to molecular weight calculation of the poly(AMPS-*co*-AA). The flowrate was 1.0 mL/min.

6.4.5.6 Thermogravimetric analysis (TGA)

TGA was used to measure the organic content of the IONPs after APTES functionalization and poly(AMPS-*co*-AA) grafting. All measurements were conducted using a Mettler-Toledo TGA/SDTA851e instrument under N_2 at a heating rate of 10 °C/min from 25 to 900 °C. The percentage loss of weight was reported as the mass fraction of organic coating on the iron oxide.

6.4.5.7 Transmission electron microscopy (TEM)

TEM images were obtained on a FEI TECNAI Spirit Bio Twin operated at 80kV. A dilute aqueous dispersion of the IONPs was deposited onto a 400 mesh Formvar-coated copper TEM grid, and allowed to dry at room temperature overnight prior to imaging.

6.4.6 Dilution test

Polymer grafting was tested by an extreme dilution test, similar to one reported previously. If the polymer was not grafted, it would desorb from the particles upon dilution, resulting in particle aggregation. 150 μL of sample were diluted in 15 mL of DI water and concentrated through a 300 kDa centrifugal filter. The resulting 150 μL IONPs were collected again and diluted in 15 mL of DI water once more; the polymer was allowed to desorb overnight, and then the sample was filtered again.

6.4.7 Batch adsorption test of poly(AMPS-*co*-AA)-grafted IONPs on silica microsphere

Adsorption of IONPs on 8 μm silica microspheres was measured in batch reactors as described in previous studies.[23] The silica drying process was conducted at low temperature (below 200 °C) to avoid dehydroxylation of the silica surface. The concentration of the poly(AMPS-*co*-AA)-grafted IONPs was adjusted to 0.06 to 1 mg/mL in API brine. For silica adsorption, 2.5 mL of the IONPs dispersions was added to 1 g of

the silica microspheres in a 1 dram screw-cap glass vial corresponding to 2.5 g of dispersion/g of rock. The glass vials were then sealed with Teflon tape and agitated horizontally overnight at room temperature on a LW Scientific Model 2100A Lab Rotator at 220 rpm. The mixture was then stood upright and left unperturbed for 24 h to allow the adsorbents to fully sediment, and the supernatant was analyzed by UV-Vis.

6.4.8 Column studies with unconsolidated porous media experiments

Column experiments were performed using a syringe pump (model 22, Harvard Apparatus, Inc., Holliston, MA), a borosilicate glass column (10 cm length × 2.5 cm i.d.; Kontes, Vineland, NJ) and a fraction collector (CF-1, Spectrum Chromatography, Houston, TX). Briefly, unwashed crushed Berea sandstone of 60-170 mesh (Specific surface area = 22.54 m^2/g) was packed into the column in 1 cm increments. Immediately after packing, the column was purged with CO_2 gas for 20 min, followed by the injection of 10 pore volumes (PVs) of background solution (API brine) in an up-flow direction to completely saturate the column media. A nonreactive tracer test (2.0 M NaBr in DI water) was performed after complete saturation to assess water flow and hydrodynamic dispersion. Following the tracer test, approximately 4 PVs of a poly(AMPS-*co*-AA) grafted IONPs suspension (1000 mg/L as Fe_3O_4 in API brine) was adjusted to pH 7 with 1.0 M NaOH and was injected into the column at a flow rate of 1.78 mL/min, which corresponds to a pore-water (seepage) velocity of approximately 12 m/day. The IONP injection was followed by 4 PVs of nanoparticle-free background solution (API brine) at the same flow rate. Quantification of influent and effluent IONPs concentrations was performed using a UV−vis spectrophotometer (UV-1800, Shimadzu Scientific Instruments, Columbia, MD) operated at 600 nm. Accuracy of the UV method was confirmed through analysis of nine duplicate samples that were prepared using a Discover SP-D microwave digester (CEM

Corporation, Matthews, NC) with concentrated nitric acid, followed by quantification of total iron using an Optima 7300 DV inductively coupled plasma-optical emission spectrometer (ICP-OES, Perkin Elmer, Waltham, MA). X-ray diffraction (XRD) analysis of Ottawa sand indicated a silica content of >99%.[39] XRD analysis of the Berea sandstone indicated a quartz content ranging from 83-88% and clay content ranging from 5-7%, including illite, chlorite, and kaolinite.

6.5 REFERENCES

(1) Al-Ali, Z. A.; Al-Buali, M. H.; AlRuwaili, S.; Ma, S. M.; Marsala, A. F.; Alumbaugh, D.; DePavia, L.; Levesque, C.; Nalonnil, A.; Zhang, P.; *et al.* Looking Deep into the Reservoir. *Oilf. Rev.* **2009**, 38–47.

(2) Saleh, N.; Kim, H.; Phenrat, T.; Matyjaszewski, K.; Tilton, R. D.; Lowry, G. V. Ionic Strength and Composition Affect the Mobility of Surface-Modified Fe 0 Nanoparticles in Water-Saturated Sand Columns. *Environ. Sci. Technol.* **2008**, *42*, 3349–3355.

(3) Laurent, S.; Forge, D.; Port, M.; Roch, A.; Robic, C.; Vander Elst, L.; Muller, R. N. Magnetic Iron Oxide Nanoparticles: Synthesis, Stabilization, Vectorization, Physicochemical Characterizations, and Biological Applications. *Chem. Rev.* **2008**, *108*, 2064–2110.

(4) Ryoo, S.; Rahmani, A. R.; Yoon, K. Y.; Prodanović, M.; Kotsmar, C.; Milner, T. E.; Johnston, K. P.; Bryant, S. L.; Huh, C. Theoretical and Experimental Investigation of the Motion of Multiphase Fluids Containing Paramagnetic Nanoparticles in Porous Media. *J. Pet. Sci. Eng.* **2012**, *81*, 129–144.

(5) Berlin, J. M.; Yu, J.; Lu, W.; Walsh, E. E.; Zhang, L.; Zhang, P.; Chen, W.; Kan, A. T.; Wong, M. S.; Tomson, M. B.; *et al.* Engineered Nanoparticles for Hydrocarbon Detection in Oil-Field Rocks. *Energy Environ. Sci.* **2011**, *4*, 505–509.

(6) Lee, H.; Shin, T.-H.; Cheon, J.; Weissleder, R. Recent Developments in Magnetic Diagnostic Systems. *Chem. Rev.* **2015**, *115*, 10690–10724.

(7) Wu, W.; He, Q.; Jiang, C. Magnetic Iron Oxide Nanoparticles: Synthesis and Surface Functionalization Strategies. *Nanoscale Res. Lett.* **2008**, *3*, 397–415.

(8) Dunn, A. S. Polymeric Stabilization of Colloidal Dispersions. By D. H. Napper, Academic Press, London, 1984. Pp. Xviii + 428, Price £39.50, $65.00. ISBN 0-12-513980-2. *Br. Polym. J.* **1986**, *18*, 278–278.

(9) Arjunan Vasantha, V.; Junhui, C.; Ying, T. B.; Parthiban, A. Salt-Responsive Polysulfabetaines from Acrylate and Acrylamide Precursors: Robust Stabilization

of Metal Nanoparticles in Hyposalinity and Hypersalinity. *Langmuir* **2015**, *31*, 11124–11134.

(10) Kowalczuk, A.; Trzcinska, R.; Trzebicka, B.; Müller, A. H. E.; Dworak, A.; Tsvetanov, C. B. Loading of Polymer Nanocarriers: Factors, Mechanisms and Applications. *Prog. Polym. Sci.* **2014**, *39*, 43–86.

(11) Li, X.; Lenhart, J. J.; Walker, H. W. Dissolution-Accompanied Aggregation Kinetics of Silver Nanoparticles. *Langmuir* **2010**, *26*, 16690–16698.

(12) Huynh, K. A.; Chen, K. L. Aggregation Kinetics of Citrate and Polyvinylpyrrolidone Coated Silver Nanoparticles in Monovalent and Divalent Electrolyte Solutions. *Environ. Sci. Technol.* **2011**, *45*, 5564–5571.

(13) Sinn, C. G.; Dimova, R.; Antonietti, M. Isothermal Titration Calorimetry of the Polyelectrolyte/Water Interaction and Binding of Ca 2+ : Effects Determining the Quality of Polymeric Scale Inhibitors. *Macromolecules* **2004**, *37*, 3444–3450.

(14) Lages, S.; Lindner, P.; Sinha, P.; Kiriy, A.; Stamm, M.; Huber, K. Formation of Ca 2+ -Induced Intermediate Necklace Structures of Polyacrylate Chains. *Macromolecules* **2009**, *42*, 4288–4299.

(15) Newman, J. K.; Mccormick, C. L. Water-Soluble Copolymers. 52. Sodium-23 NMR Studies. **1994**, 5114–5122.

(16) Newman, J. K.; McCormick, C. L. Water-Soluble Copolymers. 52. Sodium-23 NMR Studies of Ion-Binding to Anionic Polyelectrolytes: Poly(sodium 2-Acrylamido-2-Methylpropanesulfonate), Poly(sodium 3-Acrylamido-3-Methylbutanoate), Poly(sodium Acrylate), and Poly(sodium Galacturonate). *Macromolecules* **1994**, *27*, 5114–5122.

(17) Ditsch, A.; Laibinis, P. E.; Wang, D. I. C.; Hatton, T. A. Controlled Clustering and Enhanced Stability of Polymer-Coated Magnetic Nanoparticles Controlled Clustering and Enhanced Stability of Polymer-Coated Magnetic Nanoparticles. **2005**.

(18) Yoon, K. Y.; Kotsmar, C.; Ingram, D. R.; Huh, C.; Bryant, S. L.; Milner, T. E.; Johnston, K. P. Stabilization of Superparamagnetic Iron Oxide Nanoclusters in Concentrated Brine with Cross-Linked Polymer Shells. *Langmuir* **2011**, *27*, 10962–10969.

(19) Ge, J.; Hu, Y.; Biasini, M.; Dong, C.; Guo, J.; Beyermann, W. P.; Yin, Y. One-Step Synthesis of Highly Water-Soluble Magnetite Colloidal Nanocrystals. *Chemistry* **2007**, *13*, 7153–7161.

(20) Ersenkal, D. A.; Ziylan, A.; Ince, N. H.; Acar, H. Y.; Demirer, M.; Copty, N. K. Impact of Dilution on the Transport of Poly(acrylic Acid) Supported Magnetite Nanoparticles in Porous Media. *J. Contam. Hydrol.* **2011**, *126*, 248–257.

(21) Bagaria, H. G.; Neilson, B. M.; Worthen, A. J.; Xue, Z.; Yoon, K. Y.; Cheng, V.; Lee, J. H.; Velagala, S.; Huh, C.; Bryant, S. L.; *et al.* Adsorption of Iron Oxide Nanoclusters Stabilized with Sulfonated Copolymers on Silica in Concentrated NaCl and CaCl2 Brine. *J. Colloid Interface Sci.* **2013**, *398*, 217–226.

(22) Bagaria, H. G.; Yoon, K. Y.; Neilson, B. M.; Cheng, V.; Lee, J. H.; Worthen, A. J.; Xue, Z.; Huh, C.; Bryant, S. L.; Bielawski, C. W.; *et al.* Stabilization of Iron Oxide Nanoparticles in High Sodium and Calcium Brine at High Temperatures with Adsorbed Sulfonated Copolymers. *Langmuir* **2013**, *29*, 3195–3206.

(23) Bagaria, H. G.; Xue, Z.; Neilson, B. M.; Worthen, A. J.; Yoon, K. Y.; Nayak, S.; Cheng, V.; Lee, J. H.; Bielawski, C. W.; Johnston, K. P. Iron Oxide Nanoparticles Grafted with Sulfonated Copolymers Are Stable in Concentrated Brine at Elevated Temperatures and Weakly Adsorb on Silica. *ACS Appl. Mater. Interfaces* **2013**, *5*, 3329–3339.

(24) Xue, Z.; Foster, E.; Wang, Y.; Nayak, S.; Cheng, V.; Ngo, V. W.; Pennell, K. D.; Bielawski, C. W.; Johnston, K. P. Effect of Grafted Copolymer Composition on Iron Oxide Nanoparticle Stability and Transport in Porous Media at High Salinity. *Energy & Fuels* **2014**, *28*, 3655–3665.

(25) Ureña-Benavides, E. E.; Lin, E. L.; Foster, E. L.; Xue, Z.; Ortiz, M. R.; Fei, Y.; Larsen, E. S.; Kmetz, A. A.; Lyon, B. A.; Moaseri, E.; *et al.* Low Adsorption of Magnetite Nanoparticles with Uniform Polyelectrolyte Coatings in Concentrated Brine on Model Silica and Sandstone. *Ind. Eng. Chem. Res.* **2016**, *55*, 1522–1532.

(26) Kmetz, A. a.; Becker, M. D.; Lyon, B. a.; Foster, E.; Xue, Z.; Johnston, K. P.; Abriola, L. M.; Pennell, K. D. Improved Mobility of Magnetite Nanoparticles at High Salinity with Polymers and Surfactants. *Energy & Fuels* **2016**, *30*, 1915–1926.

(27) Zhang, L.; Xue, H.; Gao, C.; Carr, L.; Wang, J.; Chu, B.; Jiang, S. Imaging and Cell Targeting Characteristics of Magnetic Nanoparticles Modified by a Functionalizable Zwitterionic Polymer with Adhesive 3,4-Dihydroxyphenyl-L-Alanine Linkages. *Biomaterials* **2010**, *31*, 6582–6588.

(28) Chanteau, B.; Fresnais, J.; Berret, J.-F. Electrosteric Enhanced Stability of Functional Sub-10 Nm Cerium and Iron Oxide Particles in Cell Culture Medium. *Langmuir* **2009**, *25*, 9064–9070.

(29) Barrera, C.; Herrera, A. P.; Bezares, N.; Fachini, E.; Olayo-Valles, R.; Hinestroza, J. P.; Rinaldi, C. Effect of Poly(ethylene Oxide)-Silane Graft Molecular Weight on the Colloidal Properties of Iron Oxide Nanoparticles for Biomedical Applications. *J. Colloid Interface Sci.* **2012**, *377*, 40–50.

(30) Amstad, E.; Textor, M.; Reimhult, E. Stabilization and Functionalization of Iron Oxide Nanoparticles for Biomedical Applications. *Nanoscale* **2011**, *3*, 2819.

(31) Lattuada, M.; Hatton, T. A. Functionalization of Monodisperse Magnetic Nanoparticles. *Langmuir* **2007**, *23*, 2158–2168.

(32) Peng, J.; Liu, Q.; Xu, Z.; Masliyah, J. Synthesis of Interfacially Active and Magnetically Responsive Nanoparticles for Multiphase Separation Applications. *Adv. Funct. Mater.* **2012**, *22*, 1732–1740.

(33) López-Cruz, A.; Barrera, C.; Calero-DdelC, V. L.; Rinaldi, C. Water Dispersible Iron Oxide Nanoparticles Coated with Covalently Linked Chitosan. *J. Mater. Chem.* **2009**, *19*, 6870.

(34) Xue, Z.; Foster, E.; Wang, Y.; Nayak, S.; Cheng, V.; Ngo, V. W.; Pennell, K. D.; Bielawski, C. W.; Johnston, K. P. Effect of Grafted Copolymer Composition on Iron Oxide Nanoparticle Stability and Transport in Porous Media at High Salinity. *Energy & Fuels* **2014**, *28*, 3655–3665.

(35) Kralj, S.; Makovec, D.; Čampelj, S.; Drofenik, M. Producing Ultra-Thin Silica Coatings on Iron-Oxide Nanoparticles to Improve Their Surface Reactivity. *J. Magn. Magn. Mater.* **2010**, *322*, 1847–1853.

(36) Wang, C.; Yan, Q.; Liu, H. B.; Zhou, X. H.; Xiao, S. J. Different EDC/NHS Activation Mechanisms between PAA and PMAA Brushes and the Following Amidation Reactions. *Langmuir* **2011**, *27*, 12058–12068.

(37) Ranka, M.; Brown, P.; Hatton, T. A. Responsive Stabilization of Nanoparticles for Extreme Salinity and High-Temperature Reservoir Applications. *ACS Appl. Mater. Interfaces* **2015**, *7*, 19651–19658.

(38) Čampelj, S.; Makovec, D.; Drofenik, M. Functionalization of Magnetic Nanoparticles with 3-Aminopropyl Silane. *J. Magn. Magn. Mater.* **2009**, *321*, 1346–1350.

(39) Wang, Y.; Li, Y.; Costanza, J.; Abriola, L. M.; Pennell, K. D. Enhanced Mobility of Fullerene (C 60) Nanoparticles in the Presence of Stabilizing Agents. *Environ. Sci. Technol.* **2012**, *46*, 11761–11769.

Chapter 7. Future Work for Polymer Grafted Magnetic Nanoparticles

In Chapters 4-6, the synthesis of highly magnetic iron oxide nanoparticles (IONPs) and a robust coating procedure was demonstrated to make them suitable for applications in gas and oil reservoirs. Three topics that could be further expanded upon include magnetic core synthesis, colloidal properties and polymer grafting methods. Here I will address these three areas as future work for this project.

7.1 Study of Magnetic Properties

Magnetic susceptibility of synthesized IONPs is discussed in Chapters 4 and 5. A subsequent study should be carried out to understand how the susceptibility changes with temperature, as oil reservoirs are often at elevated temperatures.[1] As is indicated by the Langevin equation, magnetic susceptibility (χ) is inversely proportional to temperature.

$$\chi = \left(\frac{\mathrm{dM}}{\mathrm{dH}}\right)_{\mathrm{H}\to 0} = \frac{\Theta \mu_0 \pi {M_d}^2 {D_p}^3}{18 k_{\mathrm{B}} \mathrm{T}}$$

where μ_0 is the magnetic permeability in vacuum, M_d is the bulk (solid) saturation magnetization, D_p is the magnetic diameter of the particle, Θ is the particle volume fraction, k_{B} is Boltzmann constant, and T is the absolute temperature. For example, at 120 °C (393 K), χ is expected to drop by ~1.3 times compared to the value at room temperature (298 K). Furthermore, when colloidal IONPs are dispersed in solution and form clusters, the susceptibility-temperature relationship may deviate or be more complicated than that expressed by the Langevin equation. The actual relationship should be carefully examined by vibrating sample magnetometer (VSM) at various temperatures to include factors such as changes in cluster size, surface coating morphologies, and potential changes in oxidation state incurred by temperature change and other environmental factors such as pH, pressure, etc.

Another important parameter for magnetic susceptibility is the cluster size of the IONP dispersion. As the previous studies have showed, the magnetic interactions among crystallites within a colloidal nanocrystal cluster can lead to a non-linear increase in magnetization for the cluster.[2] The situation can be further convoluted by the density of surface grafting material and/or the interaction between the IONPs and the coating material. Given the complexity of the variety of parameters that could affect the susceptibility, it may not be feasible to draw a quantitative trend for IONP dispersion in general, but case-specific measurements can be done to characterize the cluster size dependence of susceptibility for our synthesized IONPs in aqueous solution.

With regard to the downhole application of colloidal IONPs as a contrast agent for electromagnetic imaging, it would be helpful to perform more detailed simulation studies to guide experimental performance targets on the application side. For example, it would be helpful to further illuminate the threshold susceptibility for a specific gas and oil reservoir at a given temperature, pressure, distance, transmitter frequency and flow conditions, etc. Such a model could also help define the variability in threshold susceptibility from reservoir to reservoir.

7.2 Surface Coating of IONPs

Due to the non-toxic nature of iron oxide, superparamagnetic magnetite nanoparticles with high susceptibility are also good candidates for various biosensor and biomedical applications.[3–6] The work in Chapter 4 describes a fairly simple preparation method of magnetite nanoparticles with ultra-high magnetic sensitivity at room temperature. Furthermore, these IONPs are easily coated by a variety of materials, in addition to the silica coating demonstrated in Chapter 4, depending on the end-use of the material. Due to the strong tendency of iron oxide particle surfaces to form coordination

bonds, the surface properties of the IONP colloids can be adjusted by ligands or polymers in order to tune the solvation state, or to form core-shell structures with chemically reactive surfaces.[7–9]

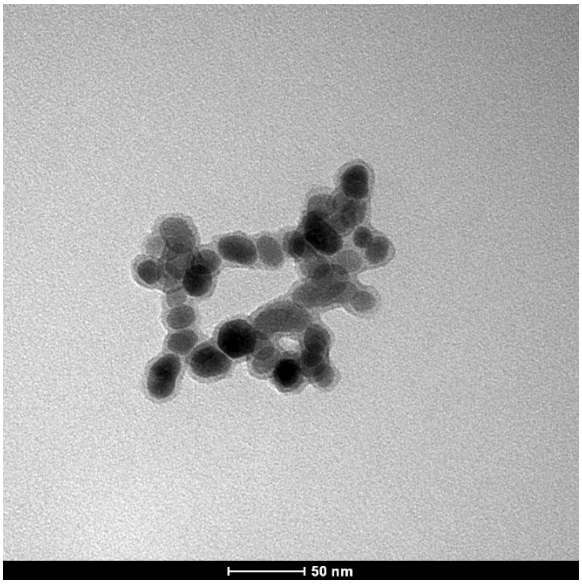

Figure 7.1: TEM images of IONPs with 2-3 nm thick polydopamine coating.

As is shown in **Figure 7.1**, we have successfully coated a thin polydopamine surface layer onto IONPs synthesized by thermal decomposition of iron acetate (as described in Chapter 4). The coating process was performed in an aqueous phase with a concentration of 1 mg/mL Fe_3O_4 and 2 mg/mL of dopamine hydrochloride. The coating process was conducted at pH 8.5 for one hour with vigorous stirring. This preliminary result is just one example of many possible surface modifications that can be assembled onto the abovementioned highly magnetic core material, rendering the particles stable in solutions. In particular, a polydopamine coating is useful in biomedical applications, where the surface functionality aids in dispersion with other biological matter, and the high magnetic susceptibility of these particles is ideal for low field strength and low concentrations (which are often desirable for sensing in living subjects).

7.3 POLYMER GRAFTING OF IONPS

In Chapter 6, we described the process of grafting a random copolymer of poly(acrylic acid-*co*-2-acrylamido-2-methylpropanesulfonate) (poly(AA-*co*-AMPS)) onto the surface of amine-functionalized IONPs. More specifically, amide bonds were formed between the AA group, distributed on the polymer chain, and the amine group anchored on the IONP surface. However, due to the random distribution of the AA groups on the polymer chain, it is impossible to accurately target a singular grafting site. After the grafting reaction, there remains an excess amount of unreacted AA groups on the surface of the nanoparticles, which are known to interact with various ionic media surfaces present in the oil reservoir environment, which could lead to a loss of nanoparticle mobility.[10,11]

To further improve the transport properties of the IONPs in a high salinity reservoir environment, more precise control of the surface functional groups on the IONPs should be targeted. Research efforts should be focused on the synthesis of a polyelectrolyte with controlled molecular weight and monomer composition. The composition and the location of different monomer units on the copolymer chain could have a significant impact on the solvation and morphology of copolymer chains in solution.[12] Therefore, instead of using a random copolymer of poly(AA-*co*-AMPS), for the 'graft-to' approach, a block copolymer of poly(AA-b-AMPS) could be synthesized via reversible addition-fragmentation chain transfer (RAFT) polymerization where a small portion of the repeat units are AA and the rest of the chain is composed of AMPS monomer. The minimum amount of AA required for grafting can be calculated and incorporated in order to achieve multi-point grafting, but a larger percentage of highly solvated AMPS block extending into the high salinity aqueous phase and providing electrosteric stabilization. The molecular weight of the polymer chains as well as the specific parameters in the grafting procedure can be also optimized for ideal grafting density.

7.4 REFERENCES

(1) Al-Ali, Z.; H. Al-Buali, M.; AlRuwaili, S.; Ma, S. M.; Marsala, A. F.; Hulme, C.; Wilt, M. Looking Deep into the Reservoir. *Oilf. Rev. Summer* **2009**, *21*, 38–47.

(2) Ge, J.; Hu, Y.; Biasini, M.; Beyermann, W. P.; Yin, Y. Superparamagnetic Magnetite Colloidal Nanocrystal Clusters. *Angew. Chemie Int. Ed.* **2007**, *46*, 4342–4345.

(3) Sun, C.; Lee, J.; Zhang, M. Magnetic Nanoparticles in MR Imaging and Drug Delivery. *Adv. Drug Deliv. Rev.* **2008**, *60*, 1252–1265.

(4) Que, E. L.; Chang, C. J. Responsive Magnetic Resonance Imaging Contrast Agents as Chemical Sensors for Metals in Biology and Medicine. *Chem. Soc. Rev.* **2010**, *39*, 51–60.

(5) Somaskandan, K.; Veres, T.; Niewczas, M.; Simard, B. Surface Protected and Modified Iron Based Core-Shell Nanoparticles for Biological Applications. *New J. Chem.* **2008**, *32*, 201.

(6) Ma, Y.; Zhang, X.; Zeng, T.; Cao, D.; Zhou, Z.; Li, W.; Niu, H.; Cai, Y. Polydopamine-Coated Magnetic Nanoparticles for Enrichment and Direct Detection of Small Molecule Pollutants Coupled with MALDI-TOF-MS. *ACS Appl. Mater. Interfaces* **2013**, *5*, 1024–1030.

(7) Lu, A.-H.; Salabas, E. L.; Schüth, F. Magnetic Nanoparticles: Synthesis, Protection, Functionalization, and Application. *Angew. Chemie Int. Ed.* **2007**, *46*, 1222–1244.

(8) Jeong, B. U.; Teng, X.; Wang, Y.; Yang, H.; Xia, Y.; Jeong, U.; Teng, X.; Wang, Y.; Yang, H.; Xia, Y. Superparamagnetic Colloids: Controlled Synthesis and Niche Applications. *Adv. Mater.* **2007**, *19*, 33–60.

(9) Lattuada, M.; Hatton, T. A. Functionalization of Monodisperse Magnetic Nanoparticles. *Langmuir* **2007**, *23*, 2158–2168.

(10) Bagaria, H. G.; Yoon, K. Y.; Neilson, B. M.; Cheng, V.; Lee, J. H.; Worthen, A. J.; Xue, Z.; Huh, C.; Bryant, S. L.; Bielawski, C. W.; *et al.* Stabilization of Iron Oxide Nanoparticles in High Sodium and Calcium Brine at High Temperatures with Adsorbed Sulfonated Copolymers. *Langmuir* **2013**, *29*, 3195–3206.

(11) Bagaria, H. G.; Xue, Z.; Neilson, B. M.; Worthen, A. J.; Yoon, K. Y.; Nayak, S.; Cheng, V.; Lee, J. H.; Bielawski, C. W.; Johnston, K. P. Iron Oxide Nanoparticles Grafted with Sulfonated Copolymers Are Stable in Concentrated Brine at Elevated Temperatures and Weakly Adsorb on Silica. *ACS Appl. Mater. Interfaces* **2013**, *5*, 3329–3339.

(12) Ranka, M.; Brown, P.; Hatton, T. A. Responsive Stabilization of Nanoparticles for Extreme Salinity and High-Temperature Reservoir Applications. *ACS Appl. Mater. Interfaces* **2015**, *7*, 19651–19658.

Appendix

APPENDIX A: WATER DISPERSIBLE MAGNETITE NANOPARTICLES WITH ULTRA-HIGH MAGNETIC SUSCEPTIBILITY FOR LOW FIELD APPLICATIONS

A.1 CHARACTERIZATION RESULTS OF SYNTHESIZED IONPS

Table A.1: Summary of different precursor-to-TEG ratios and the measured properties of IONPs

Sample	Molar ratio $[Fe(Ac)_2]$:[TEG]	DLS size (nm)	TEM size (nm)	Calculated Magnetic Diameter (nm)	Concentration of Fe_3O_4		Measured susceptibility on VSM (SI)	2 vol.% susceptibility (SI)	Saturation magnetization (emu/g Fe_3O_4)	Surface coating
					(mg/mL)	Vol. %				
1	1:11	34	15.8± 1.5	17.5	25.1	0.48	0.813	3.41	92.0	Silica
2	1:22	57	10.8± 1.6	7.3	11.47	0.22	0.112	1.03	58.7	Silica
3	1:33	54	10.8± 1.6	8.4	9.60	0.18	0.0225	0.25	46.4	Silica

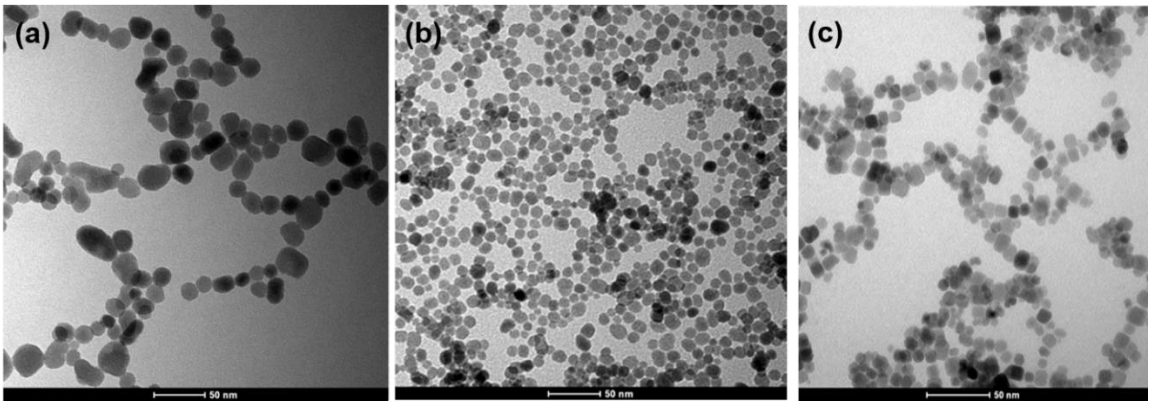

Figure A.1: Primary IONPs with different precursor ratios (a) 11 (b) 22 and (c) 33.

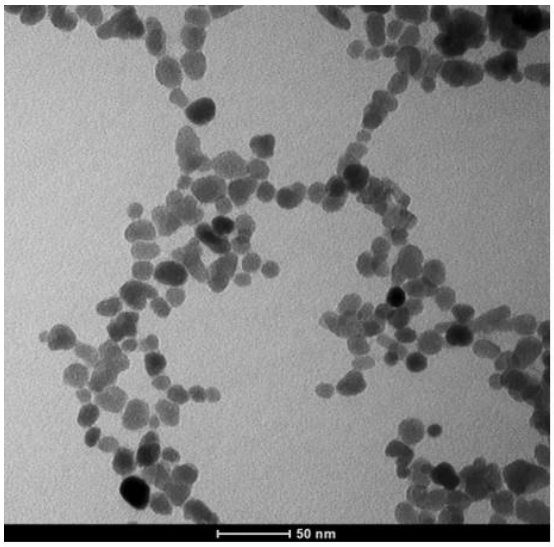
50 nm

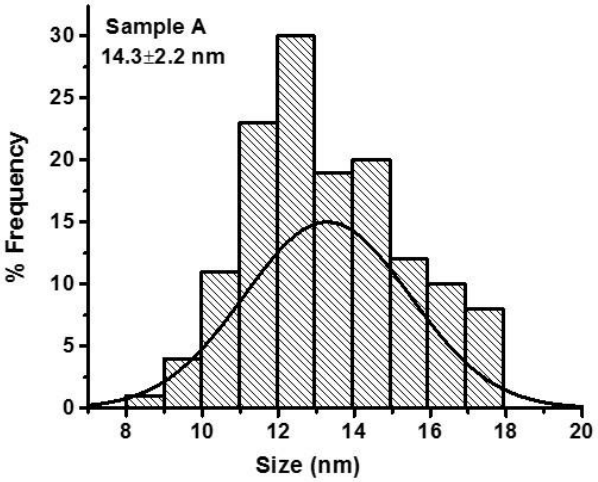
Sample A
14.3±2.2 nm
% Frequency
Size (nm)
0
5
10
15
20
25
30
8
10
12
14
16
18
20

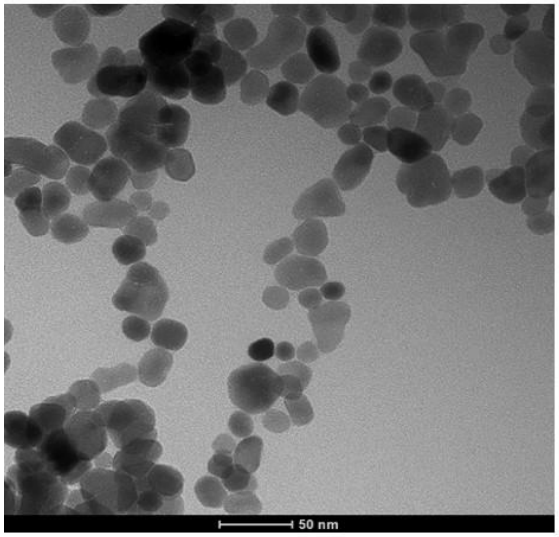
50 nm

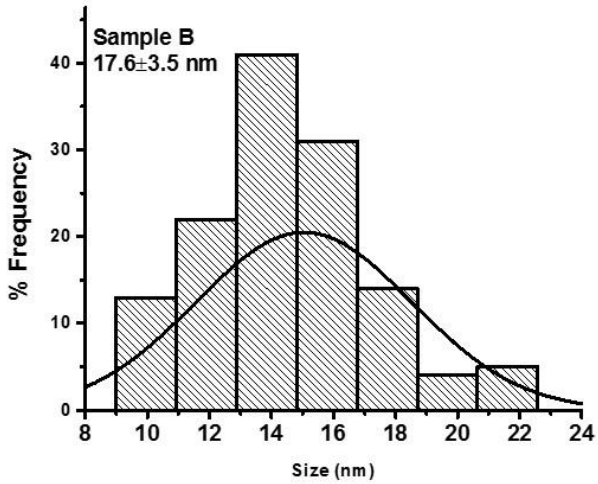
Sample B
17.6±3.5 nm
% Frequency
Size (nm)
0
10
20
30
40
8
10
12
14
16
18
20
22
24

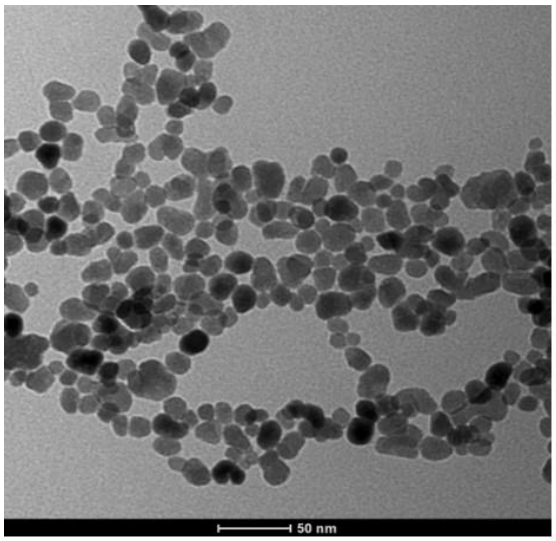
50 nm

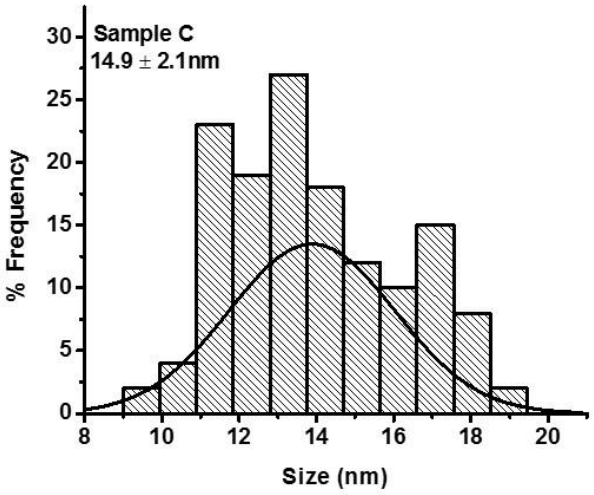
Sample C
14.9 ± 2.1nm
% Frequency
Size (nm)
0
5
10
15
20
25
30
8
10
12
14
16
18
20

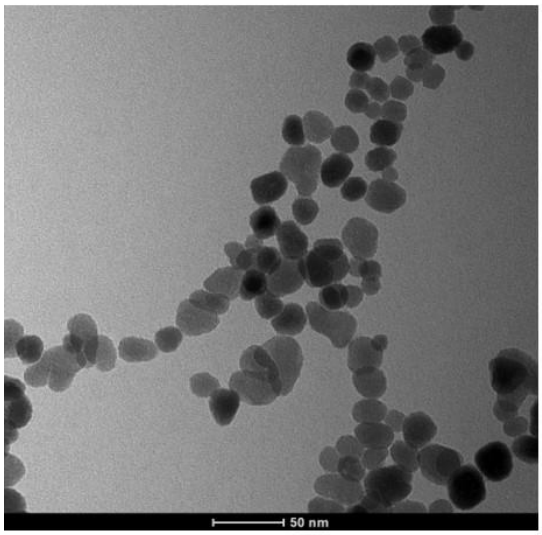
50 nm

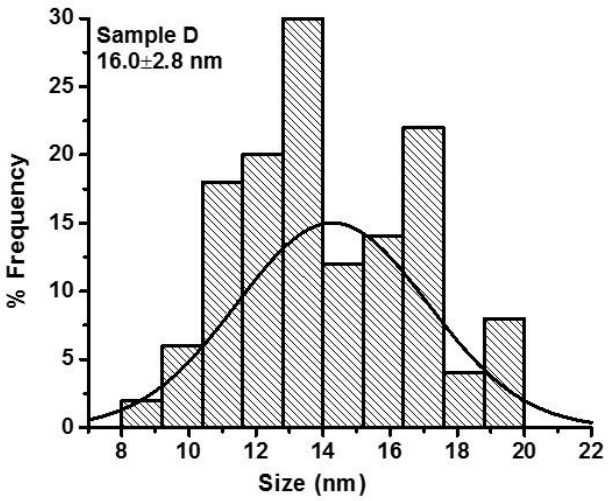
Sample D
16.0±2.8 nm
% Frequency
Size (nm)
0
5
10
15
20
25
30
8
10
12
14
16
18
20
22

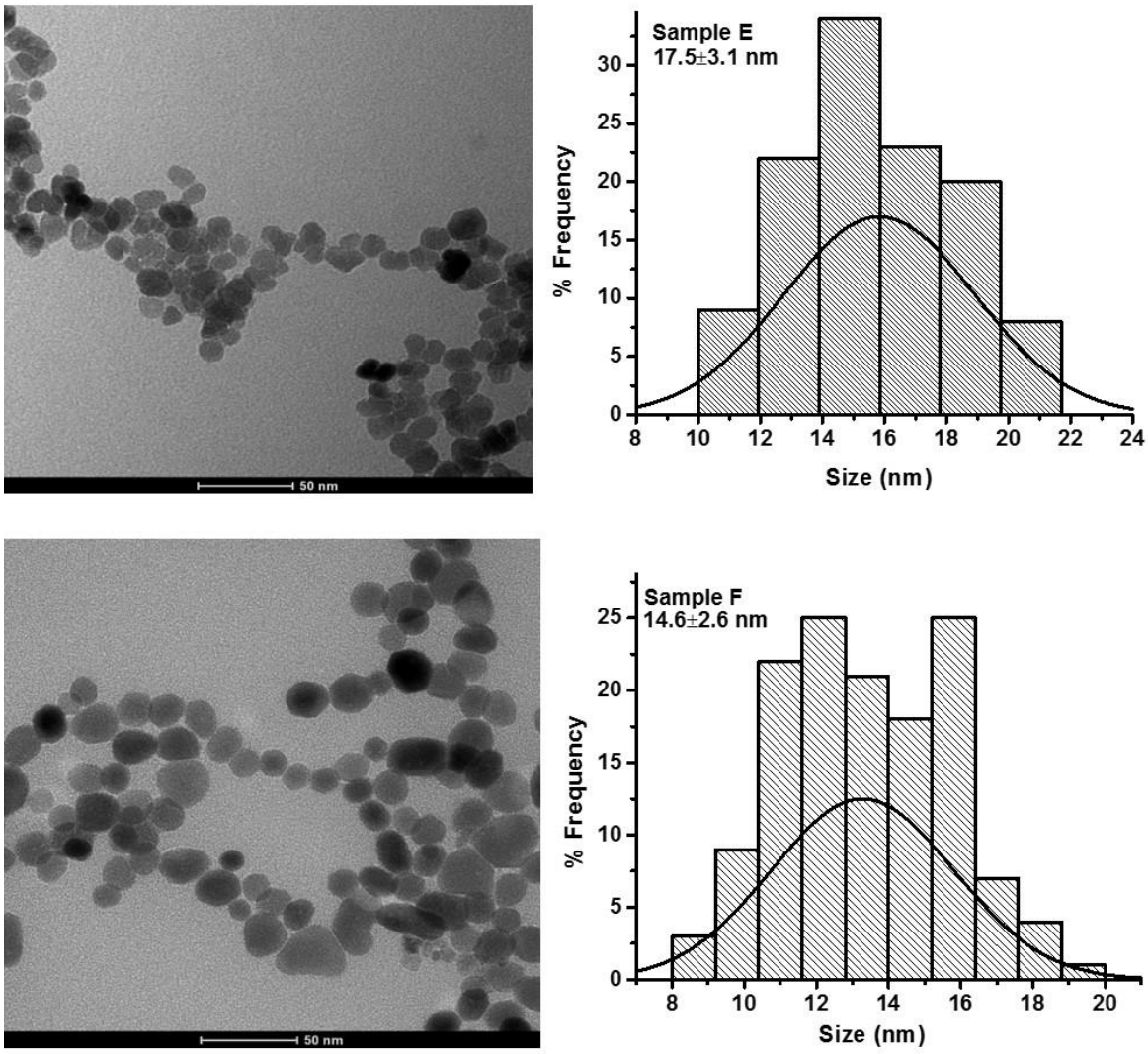

Figure A.2: Primary particle sizes of samples in **Table 4.4**.

A.2 CALCULATION OF MAGNETIC DIAMETERS OF THE SYNTHESIZED IO NPS

The magnetic diameters of clusters #1-4 were calculated based on Chantrell et al.[1] A log-normal size distribution and Langevin function for non-interacting particles were assumed.

If the particles are monodisperse, the magnetic behavior is described by the Langevin function

$$L(\alpha) = \coth \alpha - \ 1/\alpha$$

where

$\alpha = \ \mu H/k_B T.$

For polydisperse particles, the magnetization is given by the sum of the contributions from each particle diameter and weighted by the particle size distribution function

$$M \ = M_p \int_0^\infty L(\alpha) f(y)\, dy$$

At low field, the Langevin function may be written as

$$L(\alpha) = \ M_d V H/k_B T$$

Hence the magnetization becomes

$$M \ = \frac{M_p M_d H}{3k_B T} \int_0^\infty V f(y)\, dy$$

where V is the particle volume

$$V = \ \frac{\pi D_p^3 y^3}{6}$$

and consequently

$$M \ = \frac{\epsilon M_d^2 H \pi D_p^3}{18 k_B T} \int_0^\infty y^3 f(y)\, dy\,.$$

The magnetic susceptibility is given by

$$\chi_i = \ \left(\frac{dM}{dH}\right)_{H\to\infty} = \ \frac{\epsilon M_d^2 \pi D_p^3}{18 k_B T} \int_0^\infty y^3 f(y)\, dy.$$

At high field, the Langevin function may be written as

$$L(\alpha) = 1 - \ \frac{1}{\alpha} = 1 - \ \ \frac{6k_B T}{M_d H \pi D_p^3 y^3}$$

Thus,

$$M = M_p \int_0^\infty \left(1 - \frac{6k_BT}{M_d H \pi D_p^3 y^3}\right) f(y)\, dy = \left(1 - \frac{6k_BT}{M_d H \pi D_p^3}\right) \int_0^\infty y^{-3} f(y)\, dy.$$

Since the distribution function follows the normalization condition

$$\int_0^\infty f(y) dy = 1$$

the relationship between M_d and H' is given by

$$1 = \frac{6k_BTH'}{M_d H \pi D_p^3} \int_0^\infty y^{-3} f(y)\, dy$$

The log-normal size distribution is given by

$$f(y) = \frac{1}{y\sigma\sqrt{2\pi}} \exp\left(-\frac{(\ln y)^2}{2\sigma^2}\right)$$

For this distribution, the integrals in the magnetic susceptibility χ_i and M_d versus H' relationship can be written as

$$\int_0^\infty y^n f(y)\, dy = \int_0^\infty \frac{y^n}{y\sigma\sqrt{2\pi}} \exp\left(-\frac{(\ln y)^2}{2\sigma^2}\right) dy$$

With the definition

$$z = \frac{\ln y}{\sigma} - n\sigma$$

and substitution into $\int_0^\infty y^n f(y)\, dy$, the result is

$$\int_0^\infty y^n f(y)\, dy = \exp\left(\frac{n^2\sigma^2}{2}\right) \int_0^\infty \frac{1}{\sqrt{2\pi}} \exp\left(-\frac{z^2}{2}\right) dz = \exp\left(\frac{n^2\sigma^2}{2}\right)$$

Substitution of this integral into the above relationship for magnetic susceptibility χ_i and into the M_d versus H' relationship gives the final result:

$$D_p = \left(\frac{18k_BT}{\pi M_d}\left[\frac{\chi_i}{3\epsilon M_d H'}\right]^{1/2}\right)^{1/3}$$

$$\sigma = \frac{1}{3}\left(\ln\left(\frac{3\chi_i H'}{\epsilon M_d}\right)\right)^{1/2}$$

Nomenclature

σ: standard deviation

μ: magnetic moment of a particle, given by $\mu = M_d V$

χ_i: initial magnetic susceptibility on a volume basis

ϵ: volume fraction of particles

D: particle diameter

D_p: median diameter of particles

$f(y)$: particle size distribution function, where y is the reduced diameter, given by $y = D/D_p$

H: magnetic field strength

H': the $M = 0$ intercept of a graph of M versus $1/H$ at high applied fields

k_B: Boltzmann constant

M: magnetization

M_d: saturation magnetization of the bulk on a volume basis

M_p: saturation magnetization of the magnetic fluids, i.e. the intercept at $1/H = 0$ of a plot of M versus $1/H$

T: temperature on a Kelvin scale

V: particle volume

A.3 REFERENCES

(1) Chantrell, R. W.; Popplewell, J.; Charles, S. W. *IEEE Trans. Magn.* **1978**, *14*, 975-977.

References

(1) Balazs, A. C.; Emrick, T.; Russell, T. P. Nanoparticle Polymer Composites: Where Two Small Worlds Meet. *Science* **2006**, *314*, 1107–1110.

(2) Paul, D. R.; Robeson, L. M. Polymer Nanotechnology: Nanocomposites. *Polymer (Guildf).* **2008**, *49*, 3187–3204.

(3) Kumar, S. K.; Jouault, N.; Benicewicz, B.; Neely, T. Nanocomposites with Polymer Grafted Nanoparticles. *Macromolecules* **2013**, *46*, 3199–3214.

(4) Krishnamoorti, R. Strategies for Dispersing Nanoparticles in Polymers. *MRS Bull.* **2007**, *32*, 341–347.

(5) Krishnamoorti, R.; Vaia, R. A. Polymer Nanocomposites. *J. Polym. Sci. Part B Polym. Phys.* **2007**, *45*, 3252–3256.

(6) LeBaron, P.; Wang, Z.; Pinnavaia, T. Polymer-Layered Silicate Nanocomposites: An Overview. *Appl. Clay Sci.* **1999**, *15*, 11–29.

(7) Gilman, J. W.; Kashiwagi, T.; Lichtenhan, J. D. Nanocomposites: A Revolutionary New Flame Retardant Approach. *Sampe Journal*, 1997, *33*, 40–46.

(8) Bourgeat-Lami, E. Organic–Inorganic Nanostructured Colloids. *J. Nanosci. Nanotechnol.* **2002**, *2*, 1–24.

(9) Althues, H.; Henle, J.; Kaskel, S. Functional Inorganic Nanofillers for Transparent Polymers. *Chem. Soc. Rev.* **2007**, *36*, 1454.

(10) Kojima, Y.; Usuki, A.; Kawasumi, M.; Okada, A.; Kurauchi, T.; Kamigaito, O. Synthesis of Nylon 6–clay Hybrid by Montmorillonite Intercalated with ε-Caprolactam. *J. Polym. Sci. Part A Polym. Chem.* **1993**, *31*, 983–986.

(11) Kojima, Y.; Usuki, A.; Kawasumi, M.; Okada, A.; Fukushima, Y.; Kurauchi, T.; Kamigaito, O. Mechanical Properties of Nylon 6-Clay Hybrid. *J. Mater. Res.* **1993**, *8*, 1185–1189.

(12) Bockstaller, M. R.; Mickiewicz, R. a.; Thomas, E. L. Block Copolymer Nanocomposites: Perspectives for Tailored Functional Materials. *Adv. Mater.* **2005**, *17*, 1331–1349.

(13) Liff, S. M.; Kumar, N.; McKinley, G. H. High-Performance Elastomeric Nanocomposites via Solvent-Exchange Processing. *Nat. Mater.* **2007**, *6*, 76–83.

(14) Fredrickson, G. H.; Bicerano, J. Barrier Properties of Oriented Disk Composites. *J. Chem. Phys.* **1999**, *110*, 2181.

(15) Lin, Y.; Böker, A.; He, J.; Sill, K.; Xiang, H.; Abetz, C.; Li, X.; Wang, J.; Emrick, T.; Long, S.; *et al.* Self-Directed Self-Assembly of Nanoparticle/copolymer Mixtures. *Nature* **2005**, *434*, 55–59.

(16) Oberdisse, J. Aggregation of Colloidal Nanoparticles in Polymer Matrices. *Soft Matter* **2006**, *2*, 29–36.

(17) Payne, A. R. Effect of Dispersion on Dynamic Properties of Filler-Loaded Rubbers. *Rubber Chem. Technol.* **1966**, *39*, 365–374.

(18) Zhu, Z.; Thompson, T.; Wang, S.; von Meerwall, E. D.; Halasa, A. Investigating Linear and Nonlinear Viscoelastic Behavior Using Model Silica-Particle-Filled Polybutadiene. *Macromolecules* **2005**, *38*, 8816–8824.

(19) Bartholmai, M.; Schartel, B. Layered Silicate Polymer Nanocomposites: New Approach or Illusion for Fire Retardancy? Investigations of the Potentials and the Tasks Using a Model System. *Polym. Adv. Technol.* **2004**, *15*, 355–364.

(20) Moniruzzaman, M.; Winey, K. I. Polymer Nanocomposites Containing Carbon Nanotubes. *Macromolecules* **2006**, *39*, 5194–5205.

(21) Yoo, B. M.; Shin, H. J.; Yoon, H. W.; Park, H. B. Graphene and Graphene Oxide and Their Uses in Barrier Polymers. *J. Appl. Polym. Sci.* **2014**, *131*, 1–23.

(22) Li, X.; Zhu, Y.; Cai, W.; Borysiak, M.; Han, B.; Chen, D.; Piner, R. D.; Colombo, L.; Ruoff, R. S. Transfer of Large-Area Graphene Films for High-Performance Transparent Conductive Electrodes. *Nano Lett.* **2009**, *9*, 4359–4363.

(23) Peng, E.; Wang, F.; Xue, J. M. Nanostructured Magnetic Nanocomposites as MRI Contrast Agents. *J. Mater. Chem. B* **2015**, *3*, 2241–2276.

(24) Kumar, S. K.; Jouault, N.; Benicewicz, B.; Neely, T. Nanocomposites with Polymer Grafted Nanoparticles. *Macromolecules* **2013**, *46*, 3199–3214.

(25) Mackay, M. E. General Strategies for Nanoparticle Dispersion. *Science.* **2006**, *311*, 1740–1743.

(26) Fischer, H. Polymer Nanocomposites: From Fundamental Research to Specific Applications. *Mater. Sci. Eng. C* **2003**, *23*, 763–772.

(27) Jancar, J.; Douglas, J. F.; Starr, F. W.; Kumar, S. K.; Cassagnau, P.; Lesser, a. J.; Sternstein, S. S.; Buehler, M. J. Current Issues in Research on Structure–property Relationships in Polymer Nanocomposites. *Polymer (Guildf).* **2010**, *51*, 3321–3343.

(28) Bates, F. S.; Fredrickson, G. H. Block Copolymers—Designer Soft Materials. *Phys. Today* **1999**, *52*, 32.

(29) Vaia, R. A.; Wagner, H. D. Framework for Nanocomposites. *Mater. Today* **2004**, *7*, 32–37.

(30) Srivastava, S.; Agarwal, P.; Archer, L. A. Tethered Nanoparticle–Polymer Composites: Phase Stability and Curvature. *Langmuir* **2012**, *28*, 6276–6281.

(31) Tao, P.; Viswanath, A.; Schadler, L. S.; Benicewicz, B. C.; Siegel, R. W. Preparation and Optical Properties of Indium Tin Oxide/Epoxy Nanocomposites

with Polyglycidyl Methacrylate Grafted Nanoparticles. *ACS Appl. Mater. Interfaces* **2011**, *3*, 3638–3645.

(32) Behling, R. E.; Kalluru, S. H.; Cochran, E. W. Morphological and Mechanical Behavior of Montmorillonite Grafted Block Copolymer Brushes. *J. Polym. Sci. Part B Polym. Phys.* **2016**, *54*, 353–361.

(33) Behling, R. E.; Wolf, L. M.; Cochran, E. W. Hierarchically Ordered Montmorillonite Block Copolymer Brushes. *Macromolecules* **2010**, *43*, 2111–2114.

(34) Ha, Y.; Kwon, Y.; Breiner, T.; Chan, E. P.; Tzianetopoulou, T.; Cohen, R. E.; Boyce, M. C.; Thomas, E. L. An Orientationally Ordered Hierarchical Exfoliated Clay−Block Copolymer Nanocomposite. *Macromolecules* **2005**, *38*, 5170–5179.

(35) Gam, S.; Meth, J. S.; Zane, S. G.; Chi, C.; Wood, B. A.; Seitz, M. E.; Winey, K. I.; Clarke, N.; Composto, R. J. Macromolecular Diffusion in a Crowded Polymer Nanocomposite. *Macromolecules* **2011**, *44*, 3494–3501.

(36) Vaia, R. A.; Giannelis, E. P. Lattice Model of Polymer Melt Intercalation in Organically-Modified Layered Silicates. *Macromolecules* **1997**, *30*, 7990–7999.

(37) Vaia, R. a; Giannelis, E. P. Polymer Melt Intercalation in Organically-Modified Layered Silicates: Model Predictions and Experiment. *Macromolecules* **1997**, *30*, 8000–8009.

(38) Zhou, Q.; Fan, X.; Xia, C.; Mays, J.; Advincula, R. Living Anionic Surface Initiated Polymerization (SIP) of Styrene from Clay Surfaces. *Chem. Mater.* **2001**, *13*, 2465–2467.

(39) Matyjaszewski, K.; Jakubowski, W.; Min, K.; Tang, W.; Huang, J.; Braunecker, W. A.; Tsarevsky, N. V. Diminishing Catalyst Concentration in Atom Transfer Radical Polymerization with Reducing Agents. *Proc. Natl. Acad. Sci.* **2006**, *103*, 15309–15314.

(40) Wang, J.; Matyjaszewski, K. Controlled/“living” radical Polymerization. Atom Transfer Radical Polymerization in the Presence of Transition-Metal Complexes. *J. Am. Chem. Soc.* **1995**, *117*, 5614–5615.

(41) Qin, S.; Matyjaszewski, K.; Xu, H.; Sheiko, S. S. Synthesis and Visualization of Densely Grafted Molecular Brushes with Crystallizable Poly(octadecyl Methacrylate) Block Segments. *Macromolecules* **2003**, *36*, 605–612.

(42) Jakubowski, W.; Min, K.; Matyjaszewski, K. Activators Regenerated by Electron Transfer for Atom Transfer Radical Polymerization of Styrene. *Macromolecules* **2006**, *39*, 39–45.

(43) Matyjaszewski, K.; Tsarevsky, N. V. Macromolecular Engineering by Atom Transfer Radical Polymerization. *J. Am. Chem. Soc.* **2014**, *136*, 6513–6533.

(44) Jakubowski, W.; Matyjaszewski, K. Activator Generated by Electron Transfer for Atom Transfer Radical Polymerization. *Macromolecules* **2005**, *38*, 4139–4146.

(45) Min, K.; Gao, H.; Matyjaszewski, K. Preparation of Homopolymers and Block Copolymers in Miniemulsion by ATRP Using Activators Generated by Electron Transfer (AGET). *J. Am. Chem. Soc.* **2005**, *127*, 3825–3830.

(46) Jakubowski, W.; Matyjaszewski, K. Activators Regenerated by Electron Transfer for Atom-Transfer Radical Polymerization of (Meth)acrylates and Related Block Copolymers. *Angew. Chemie - Int. Ed.* **2006**, *45*, 4482–4486.

(47) Chong, B. Y. K.; Le, T. P. T.; Moad, G.; Rizzardo, E.; Thang, S. H. A More Versatile Route to Block Copolymers and Other Polymers of Complex Architecture by Living Radical Polymerization: The RAFT Process. *Macromolecules* **1999**, *32*, 2071–2074.

(48) Chiefari, J.; Chong, Y. K. B.; Ercole, F.; Krstina, J.; Jeffery, J.; Le, T. P. T.; Mayadunne, R. T. A.; Meijs, G. F.; Moad, C. L.; Moad, G.; *et al.* Living Free-Radical Polymerization by Reversible Addition−Fragmentation Chain Transfer: The RAFT Process. *Macromolecules* **1998**, *31*, 5559–5562.

(49) Yoon, P. J.; Fornes, T. D.; Paul, D. R. Thermal Expansion Behavior of Nylon 6 Nanocomposites. *Polymer (Guildf).* **2002**, *43*, 6727–6741.

(50) Ebina, T.; Mizukami, F. Flexible Transparent Clay Films with Heat-Resistant and High Gas-Barrier Properties. *Adv. Mater.* **2007**, *19*, 2450–2453.

(51) Grunlan, J. C.; Grigorian, A.; Hamilton, C. B.; Mehrabi, A. R. Effect of Clay Concentration on the Oxygen Permeability and Optical Properties of a Modified Poly(vinyl Alcohol). *J. Appl. Polym. Sci.* **2004**, *93*, 1102–1109.

(52) Priolo, M. a.; Gamboa, D.; Holder, K. M.; Grunlan, J. C. Super Gas Barrier of Transparent Polymer-Clay Multilayer Ultrathin Films. *Nano Lett.* **2010**, *10*, 4970–4974.

(53) Bréchet, Y.; Cavaillé, J.-Y.; Chabert, E.; Chazeau, L.; Dendievel, R.; Flandin, L.; Gauthier, C. Polymer Based Nanocomposites: Effect of Filler-Filler and Filler-Matrix Interactions. *Adv. Eng. Mater.* **2001**, *3*, 571.

(54) Jagadish, R. S.; Raj, B.; Asha, M. R. Blending of Low-Density Polyethylene with Vanillin for Improved Barrier and Aroma-Releasing Properties in Food Packaging. *J. Appl. Polym. Sci.* **2009**, *113*, 3732–3741.

(55) Dong, T.; Yun, X.; Li, M.; Sun, W.; Duan, Y.; Jin, Y. Biodegradable High Oxygen Barrier Membrane for Chilled Meat Packaging. *J. Appl. Polym. Sci.* **2015**, *132*, 41871.

(56) Duncan, T. V. Applications of Nanotechnology in Food Packaging and Food Safety: Barrier Materials, Antimicrobials and Sensors. *J. Colloid Interface Sci.* **2011**, *363*, 1–24.

(57) Di, L.; Kerns, E. H.; Fan, K.; McConnell, O. J.; Carter, G. T. High Throughput Artificial Membrane Permeability Assay for Blood–brain Barrier. *Eur. J. Med. Chem.* **2003**, *38*, 223–232.

(58) Reichel, A.; Begley, D. J. Potential of Immobilized Artificial Membranes for Predicting Drug Penetration Across the Blood-Brain Barrier. *Pharm. Res.* **1998**, *15*, 1270–1274.

(59) Chatham, H. Oxygen Diffusion Barrier Properties of Transparent Oxide Coatings on Polymeric Substrates. *Surf. Coatings Technol.* **1996**, *78*, 1–9.

(60) Lange, J.; Wyser, Y. Recent Innovations in Barrier Technologies for Plastic Packaging?a Review. *Packag. Technol. Sci.* **2003**, *16*, 149–158.

(61) Nielsen, L. E. Models for the Permeability of Filled Polymer Systems. *J. Macromol. Sci. Part A - Chem.* **1967**, *1*, 929–942.

(62) Giannelis, E. P.; Krishnamoorti, R.; Manias, E. Polymer-Silicate Nanocomposites: Model Systems for Confined Polymers and Polymer Brushes. In *ADVANCES IN POLYMER SCIENCE*; 1999; Vol. 138, pp. 107–147.

(63) Vaia, R. A.; Teukolsky, R. K.; Giannelis, E. P. Interlayer Structure and Molecular Environment of Alkylammonium Layered Silicates. *Chem. Mater.* **1994**, *6*, 1017–1022.

(64) Heinz, H.; Vaia, R. a; Farmer, B. L. Interaction Energy and Surface Reconstruction between Sheets of Layered Silicates. *J. Chem. Phys.* **2006**, *124*, 224713.

(65) Giannelis, E. P. Polymer Layered Silicate Nanocomposites. *Adv. Mater.* **1996**, *8*, 29–35.

(66) Sinha Ray, S.; Okamoto, M. Polymer/layered Silicate Nanocomposites: A Review from Preparation to Processing. *Prog. Polym. Sci.* **2003**, *28*, 1539–1641.

(67) Hussain, F. Review Article: Polymer-Matrix Nanocomposites, Processing, Manufacturing, and Application: An Overview. *J. Compos. Mater.* **2006**, *40*, 1511–1575.

(68) Biasci, L.; Aglietto, M.; Ruggeri, G.; Ciardelli, F. Functionalization of Montmorillonite by Methyl Methacrylate Polymers Containing Side-Chain Ammonium Cations. *Polymer (Guildf).* **1994**, *35*, 3296–3304.

(69) Huang, X.; Lewis, S.; Brittain, W. J.; Vaia, R. A. Synthesis of Polycarbonate-Layered Silicate Nanocomposites via Cyclic Oligomers. *Macromolecules* **2000**, *33*, 2000–2004.

(70) Kalluru, S. H.; Cochran, E. W. Synthesis of Polyolefin/Layered Silicate Nanocomposites via Surface-Initiated Ring-Opening Metathesis Polymerization. *Macromolecules* **2013**, *46*, 9324–9332.

(71) Fan, X.; Xia, C.; Advincula, R. C. On the Formation of Narrowly Polydispersed PMMA by Surface Initiated Polymerization (SIP) from AIBN-Coated/intercalated Clay Nanoparticle Platelets. *Langmuir* **2005**, *21*, 2537–2544.

(72) Datta, H.; Bhowmick, A. K.; Singha, N. K. Tailor-Made Hybrid Nanostructure of Poly (Ethyl Acrylate)/ Clay by Surface-Initiated Atom Transfer Radical Polymerization. **2008**, 5014–5027.

(73) Bassett, D. C. *Principles of Polymer Morphology (Cambridge Solid State Series)*; Cambridge University Press: Cambridge, England, 1981.

(74) Wang, H.; Keum, J. K.; Hiltner, A.; Baer, E.; Freeman, B.; Rozanski, A.; Galeski, A. Confined Crystallization of Polyethylene Oxide in Nanolayer Assemblies. *Science.* **2009**, *323*, 757–760.

(75) Cochran, E. W.; Morse, D. C.; Bates, F. S. Design of ABC Triblock Copolymers near the ODT with the Random Phase Approximation. *Macromolecules* **2003**, *36*, 782–792.

(76) Matyjaszewski, K.; Tsarevsky, N. V. Nanostructured Functional Materials Prepared by Atom Transfer Radical Polymerization. *Nat. Chem.* **2009**, *1*, 276–288.

(77) Mogri, Z.; Paul, D. . Gas Sorption and Transport in Side-Chain Crystalline and Molten Poly(octadecyl Acrylate). *Polymer (Guildf).* **2001**, *42*, 2531–2542.

(78) Fox, T. G.; Flory, P. J. Second-Order Transition Temperatures and Related Properties of Polystyrene. I. Influence of Molecular Weight. *J. Appl. Phys.* **1950**, *21*, 581–591.

(79) Jordan, E. F. Side-Chain Crystallinity. III. Influence of Side-Chain Crystallinity on the Glass Transition Temperatures of Selected Copolymers Incorporating N-Octadecyl Acrylate or Vinyl Stearate. *J. Polym. Sci. Part A-1 Polym. Chem.* **1971**, *9*, 3367–3378.

(80) Zhao, H.; Shipp, D. a. Preparation of Poly(styrene- Block -Butyl Acrylate) Block Copolymer−Silicate Nanocomposites. *Chem. Mater.* **2003**, *15*, 2693–2695.

(81) Hang, P. T. Methylene Blue Absorption by Clay Minerals. Determination of Surface Areas and Cation Exchange Capacities (Clay-Organic Studies XVIII). *Clays Clay Miner.* **1970**, *18*, 203–212.

(82) Behling, R. E.; Williams, B. a.; Staade, B. L.; Wolf, L. M.; Cochran, E. W. Influence of Graft Density on Kinetics of Surface-Initiated ATRP of Polystyrene from Montmorillonite. *Macromolecules* **2009**, *42*, 1867–1872.

(83) Shen, Y.-H. Estimation of Surface Area of Montmorillonite by Ethylene Oxide Chain Adsorption. *Chemosphere* **2002**, *48*, 1075–1079.

(84) Jordan, R.; Ulman, a; Kang, J. F.; Rafailovich, M. H.; Sokolov, J. Surface-Initiated Anionic Polymerization of Styrene by Means of Self-Assembled Monolayers. *J. Am. Chem. Soc.* **1999**, *121*, 1016–1022.

(85) Yamamoto, S.; Ejaz, M.; Tsujii, Y.; Fukuda, T. Surface Interaction Forces of Well-Defined, High-Density Polymer Brushes Studied by Atomic Force Microscopy. 2. Effect of Graft Density. *Macromolecules* **2000**, *33*, 5608–5612.

(86) Kawasumi, M.; Hasegawa, N.; Kato, M.; Usuki, A.; Okada, A. Preparation and Mechanical Properties of Polypropylene−Clay Hybrids. *Macromolecules* **1997**, *30*, 6333–6338.

(87) Hasegawa, N.; Kawasumi, M.; Kato, M.; Usuki, A.; Okada, A. Preparation and Mechanical Properties of Polypropylene-Clay Hybrids Using a Maleic Anhydride-Modified Polypropylene Oligomer. *J. Appl. Polym. Sci.* **1998**, *67*, 87–92.

(88) Zhang, Q.; Fu, Q.; Jiang, L.; Lei, Y. Preparation and Properties of Polypropylene/montmorillonite Layered Nanocomposites. *Polym. Int.* **2000**, *49*, 1561–1564.

(89) Broadhurst, M. G. An Analysis of the Solid Phase Behavior of the Normal Paraffins. *J. Res. Natl. Bur. Stand. Sect. A Phys. Chem.* **1962**, *66A*, 241.

(90) Bharadwaj, R. K.; Mehrabi, a. R.; Hamilton, C.; Trujillo, C.; Murga, M.; Fan, R.; Chavira, a.; Thompson, a. K. Structure–property Relationships in Cross-Linked Polyester–clay Nanocomposites. *Polymer (Guildf).* **2002**, *43*, 3699–3705.

(91) Zhao, H.; Farrell, B. P.; Shipp, D. a. Nanopatterns of Poly(styrene-Block-Butyl Acrylate) Block Copolymer Brushes on the Surfaces of Exfoliated and Intercalated Clay Layers. *Polymer (Guildf).* **2004**, *45*, 4473–4481.

(92) Beiner, M.; Huth, H. Nanophase Separation and Hindered Glass Transition in Side-Chain Polymers. *Nat. Mater.* **2003**, *2*, 595–599.

(93) Jordan, E. F.; Feldeisen, D. W.; Wrigley, A. N. Side-Chain Crystallinity. I. Heats of Fusion and Melting Transitions on Selected Homopolymers Having Long Side Chains. *J. Polym. Sci. Part A-1 Polym. Chem.* **1971**, *9*, 1835–1851.

(94) Beers, K.; Matyjaszewski, K. The Atom Transfer Radical Polymerization of Lauryl Acrylate. *J. Macromol. Sci. Part A* **2001**, *38*, 731–739.

(95) Michaels, A. S.; Bixler, H. J. Flow of Gases through Polyethylene. *J. Polym. Sci.* **1961**, *50*, 413–439.

(96) Choi, W. J.; Kim, H. J.; Yoon, K. H.; Kwon, O. H.; Hwang, C. I. Preparation and Barrier Property of Poly(ethylene Terephthalate)/clay Nanocomposite Using Clay-Supported Catalyst. *J. Appl. Polym. Sci.* **2006**, *100*, 4875–4879.

(97) Daily, W.; Owen, E. Cross-borehole Resistivity Tomography. *Geophysics* **1991**, *56*, 1228–1235.

(98) Al-Ali, Z.; H. Al-Buali, M.; AlRuwaili, S.; Ma, S. M.; Marsala, A. F.; Hulme, C.; Wilt, M. Looking Deep into the Reservoir. *Oilf. Rev. Summer* **2009**, *21*, 38–47.

(99) Na, H. Bin; Song, I. C.; Hyeon, T. Inorganic Nanoparticles for MRI Contrast Agents. *Adv. Mater.* **2009**, *21*, 2133–2148.

(100) Sulek, S.; Mammadov, B.; Mahcicek, D. I.; Sozeri, H.; Atalar, E.; Tekinay, A. B.; Guler, M. O. Peptide Functionalized Superparamagnetic Iron Oxide Nanoparticles as MRI Contrast Agents. *J. Mater. Chem.* **2011**, *21*, 15157.

(101) Schladt, T. D.; Schneider, K.; Schild, H.; Tremel, W. Synthesis and Bio-Functionalization of Magnetic Nanoparticles for Medical Diagnosis and Treatment. *Dalt. Trans.* **2011**, *40*, 6315.

(102) Sun, C.; Lee, J.; Zhang, M. Magnetic Nanoparticles in MR Imaging and Drug Delivery☆. *Adv. Drug Deliv. Rev.* **2008**, *60*, 1252–1265.

(103) Maier-Hauff, K.; Rothe, R.; Scholz, R.; Gneveckow, U.; Wust, P.; Thiesen, B.; Feussner, A.; von Deimling, A.; Waldoefner, N.; Felix, R.; *et al.* Intracranial Thermotherapy Using Magnetic Nanoparticles Combined with External Beam Radiotherapy: Results of a Feasibility Study on Patients with Glioblastoma Multiforme. *J. Neurooncol.* **2007**, *81*, 53–60.

(104) Jordan, A.; Scholz, R.; Wust, P.; Fähling, H.; Roland Felix. Magnetic Fluid Hyperthermia (MFH): Cancer Treatment with AC Magnetic Field Induced Excitation of Biocompatible Superparamagnetic Nanoparticles. *J. Magn. Magn. Mater.* **1999**, *201*, 413–419.

(105) Yavuz, C. T.; Mayo, J. T.; Yu, W. W.; Prakash, A.; Falkner, J. C.; Yean, S.; Cong, L.; Shipley, H. J.; Kan, A.; Tomson, M.; *et al.* Low-Field Magnetic Separation of Monodisperse Fe3O4 Nanocrystals. *Science.* **2006**, *314*, 964–967.

(106) Sun, S. Monodisperse FePt Nanoparticles and Ferromagnetic FePt Nanocrystal Superlattices. *Science.* **2000**, *287*, 1989–1992.

(107) Desvaux, C.; Amiens, C.; Fejes, P.; Renaud, P.; Respaud, M.; Lecante, P.; Snoeck, E.; Chaudret, B. Multimillimetre-Large Superlattices of Air-Stable Iron–cobalt Nanoparticles. *Nat. Mater.* **2005**, *4*, 750–753.

(108) Reiss, G.; Hütten, A. Magnetic Nanoparticles: Applications beyond Data Storage. *Nat. Mater.* **2005**, *4*, 725–726.

(109) Sun, S.; Zeng, H. Size-Controlled Synthesis of Magnetite Nanoparticles. *J. Am. Chem. Soc.* **2002**, *124*, 8204–8205.

(110) Ewijk, G. a Van; Vroege, G. J.; Philipse, A. P. Susceptibility Measurements on a Fractionated Aggregate-Free Ferrofluid. *J. Phys. Condens. Matter* **2002**, *14*, 4915–4925.

(111) Jeong, B. U.; Teng, X.; Wang, Y.; Yang, H.; Xia, Y.; Jeong, U.; Teng, X.; Wang, Y.; Yang, H.; Xia, Y. Superparamagnetic Colloids: Controlled Synthesis and Niche Applications. *Adv. Mater.* **2007**, *19*, 33–60.

(112) Rosensweig, R. E. *Ferrohydrodynamics*; Cambridge ; New York : Cambridge University Press, 1985.

(113) Chantrell, R.; Popplewell, J.; Charles, S. Measurements of Particle Size Distribution Parameters in Ferrofluids. *IEEE Trans. Magn.* **1978**, *14*, 975–977.

(114) Ditsch, A.; Lindenmann, S.; Laibinis, P. E.; Wang, D. I. C.; Hatton, T. A. High-Gradient Magnetic Separation of Magnetic Nanoclusters. *Ind. Eng. Chem. Res.* **2005**, *44*, 6824–6836.

(115) Ge, J.; Hu, Y.; Biasini, M.; Dong, C.; Guo, J.; Beyermann, W. P.; Yin, Y. One-Step Synthesis of Highly Water-Soluble Magnetite Colloidal Nanocrystals. *Chemistry* **2007**, *13*, 7153–7161.

(116) Yoon, K. Y.; Xue, Z.; Fei, Y.; Lee, J. H.; Cheng, V.; Bagaria, H. G.; Huh, C.; Bryant, S. L.; Kong, S. D.; Ngo, V. W.; *et al.* Control of Magnetite Primary Particle Size in Aqueous Dispersions of Nanoclusters for High Magnetic Susceptibilities. *J. Colloid Interface Sci.* **2016**, *462*, 359–367.

(117) Rasa, M. Magnetic Properties and Magneto-Birefringence of Magnetic Fluids. *Eur. Phys. J. E* **2000**, *2*, 265–275.

(118) Huang, W.; Wu, J.; Guo, W.; Li, R.; Cui, L. Study on the Synthesis of ε-Fe3N-Based Magnetic Fluid. *J. Magn. Magn. Mater.* **2006**, *307*, 198–204.

(119) Huang, W.; Wu, J.; Guo, W.; Li, R.; Cui, L. Initial Susceptibility and Viscosity Properties of Low Concentration ε-Fe3 N Based Magnetic Fluid. *Nanoscale Res. Lett.* **2007**, *2*, 155–160.

(120) Massart, R. Preparation of Aqueous Magnetic Liquids in Alkaline and Acidic Media. *IEEE Trans. Magn.* **1981**, *17*, 1247–1248.

(121) Lyon, J. L.; Fleming, D. a.; Stone, M. B.; Schiffer, P.; Williams, M. E.; Park, U. V; Pennsyl, V. Synthesis of Fe Oxide Core/Au Shell Nanoparticles by Iterative Hydroxylamine Seeding. *Nano Lett.* **2004**, *4*, 719–723.

(122) Ditsch, A.; Laibinis, P. E.; Wang, D. I. C.; Hatton, T. A. Controlled Clustering and Enhanced Stability of Polymer-Coated Magnetic Nanoparticles. *Langmuir* **2005**, *21*, 6006–6018.

(123) Sahoo, Y.; Goodarzi, A.; Swihart, M. T.; Ohulchanskyy, T. Y.; Kaur, N.; Furlani, E. P.; Prasad, P. N. Aqueous Ferrofluid of Magnetite Nanoparticles: Fluorescence Labeling and Magnetophoretic Control. *J. Phys. Chem. B* **2005**, *109*, 3879–3885.

(124) Wan, J.; Cai, W.; Meng, X.; Liu, E. Monodisperse Water-Soluble Magnetite Nanoparticles Prepared by Polyol Process for High-Performance Magnetic Resonance Imaging. *Chem. Commun. (Camb).* **2007**, *4*, 5004–5006.

(125) Das, M.; Dhak, P.; Gupta, S.; Mishra, D.; Maiti, T. K.; Basak, A.; Pramanik, P. Highly Biocompatible and Water-Dispersible, Amine Functionalized Magnetite Nanoparticles, Prepared by a Low Temperature, Air-Assisted Polyol Process: A New Platform for Bio-Separation and Diagnostics. *Nanotechnology* **2010**, *21*, 125103.

(126) Feldmann, C.; Jungk, H. O. Polyol-Mediated Preparation of Nanoscale Oxide Particles. *Angew. Chemie - Int. Ed.* **2001**, *40*, 359–362.

(127) Park, J.; Joo, J.; Soon, G. K.; Jang, Y.; Hyeon, T. Synthesis of Monodisperse Spherical Nanocrystals. *Angew. Chemie - Int. Ed.* **2007**, *46*, 4630–4660.

(128) Miguel-Sancho, N.; Bomati-Miguel, O.; Roca, A. G.; Martinez, G.; Arruebo, M.; Santamaria, J. Synthesis of Magnetic Nanocrystals by Thermal Decomposition in Glycol Media: Effect of Process Variables and Mechanistic Study. *Ind. Eng. Chem. Res.* **2012**, *51*, 8348–8357.

(129) Redl, F. X.; Black, C. T.; Papaefthymiou, G. C.; Sandstrom, R. L.; Yin, M.; Zeng, H.; Murray, C. B.; O'Brien, S. P. Magnetic, Electronic, and Structural Characterization of Nonstoichiometric Iron Oxides at the Nanoscale. *J. Am. Chem. Soc.* **2004**, *126*, 14583–14599.

(130) Yin, M.; O'Brien, S. Synthesis of Monodisperse Nanocrystals of Manganese Oxides. *J. Am. Chem. Soc.* **2003**, *125*, 10180–10181.

(131) Kralj, S.; Makovec, D.; Čampelj, S.; Drofenik, M. Producing Ultra-Thin Silica Coatings on Iron-Oxide Nanoparticles to Improve Their Surface Reactivity. *J. Magn. Magn. Mater.* **2010**, *322*, 1847–1853.

(132) Starowicz, M.; Starowicz, P.; Żukrowski, J.; Przewoźnik, J.; Lemański, A.; Kapusta, C.; Banaś, J. Electrochemical Synthesis of Magnetic Iron Oxide Nanoparticles with Controlled Size. *J. Nanoparticle Res.* **2011**, *13*, 7167–7176.

(133) Thanh, N. T. K. *Magnetic Nanoparticles: From Fabrication to Clinical Applications*; 1st ed.; CRC Press, 2012.

(134) R.M. Cornell, U. S. *The Iron Oxides: Structure, Properties, Reactions, Occurrences and Uses*; WILE-VCH: Weinheim, Cambridge, 1996.

(135) Vandenberghe, R. E.; Barrero, C. A.; da Costa, G. M.; Van San, E.; De Grave, E. Mössbauer Characterization of Iron Oxides and (Oxy)hydroxides: The Present State of the Art. *Hyperfine Interact.* **2000**, *126*, 247–259.

(136) Lukashova, N. V.; Savchenko, A. G.; Yagodkin, Y. D.; Muradova, A. G.; Yurtov, E. V. Structure and Magnetic Properties of Iron Oxide Nanopowders. *Met. Sci. Heat Treat.* **2013**, *54*, 550–554.

(137) Roca, A. G.; Marco, J. F.; Morales, M. del P.; Serna, C. J. Effect of Nature and Particle Size on Properties of Uniform Magnetite and Maghemite Nanoparticles. *J. Phys. Chem. C* **2007**, *111*, 18577–18584.

(138) Eom, Y.; Abbas, M.; Noh, H.; Kim, C. Morphology-Controlled Synthesis of Highly Crystalline Fe3O4 and CoFe2O4 Nanoparticles Using a Facile Thermal Decomposition Method. *RSC Adv.* **2016**, *6*, 15861–15867.

(139) Hui, C.; Shen, C.; Tian, J.; Bao, L.; Ding, H.; Li, C.; Tian, Y.; Shi, X.; Gao, H.-J. Core-Shell Fe3O4@SiO2 Nanoparticles Synthesized with Well-Dispersed Hydrophilic Fe 3 O 4 Seeds. *Nanoscale* **2011**, *3*, 701–705.

(140) Abbas, M.; Torati, S. R.; Kim, C. A Novel Approach for the Synthesis of Ultrathin Silica-Coated Iron Oxide Nanocubes Decorated with Silver Nanodots (Fe 3 O 4 /SiO 2 /Ag) and Their Superior Catalytic Reduction of 4-Nitroaniline. *Nanoscale* **2015**, *7*, 12192–12204.

(141) Ge, J.; Hu, Y.; Biasini, M.; Beyermann, W. P.; Yin, Y. Superparamagnetic Magnetite Colloidal Nanocrystal Clusters. *Angew. Chemie Int. Ed.* **2007**, *46*, 4342–4345.

(142) Qiu, P.; Jensen, C.; Charity, N.; Towner, R.; Mao, C. Oil Phase Evaporation-Induced Self-Assembly of Hydrophobic Nanoparticles into Spherical Clusters with Controlled Surface Chemistry in an Oil-in-Water Dispersion and Comparison of Behaviors of Individual and Clustered Iron Oxide Nanoparticles. *J. Am. Chem. Soc.* **2010**, *132*, 17724–17732.

(143) Misra, S. K.; Li, L.; Mukherjee, S.; Ghosh, G. Anisotropic Magnetic Field Observed at 300 K in Citrate-Coated Iron Oxide Nanoparticles: Effect of Counterions. *J. Nanoparticle Res.* **2015**, *17*, 487.

(144) Günay, M.; Baykal, A.; Sözeri, H. Structural and Magnetic Properties of Triethylene Glycol Stabilized Monodisperse Fe3O4 Nanoparticles. *J. Supercond. Nov. Magn.* **2012**, *25*, 2415–2420.

(145) Ge, J.; Hu, Y.; Biasini, M.; Beyermann, W. P.; Yin, Y. Superparamagnetic Magnetite Colloidal Nanocrystal Clusters. *Angew. Chemie Int. Ed.* **2007**, *46*, 4342–4345.

(146) LaMer, V. K.; Dinegar, R. H. Theory, Production and Mechanism of Formation of Monodispersed Hydrosols. *J. Am. Chem. Soc.* **1950**, *72*, 4847.

(147) Murray, C. B.; Kagan, C. R.; Bawendi, M. G. Synthesis and Characterization of Monodisperse Nanocrystals and Close-Packed Nanocrystal Assemblies. *Annu. Rev. Mater. Sci.* **2000**, *30*, 545–610.

(148) Mahmoudi, M.; Sant, S.; Wang, B.; Laurent, S.; Sen, T. Superparamagnetic Iron Oxide Nanoparticles (SPIONs): Development, Surface Modification and Applications in Chemotherapy. *Adv. Drug Deliv. Rev.* **2011**, *63*, 24–46.

(149) Cain, J. L.; Nikles, D. E. Preparation of Acicular α-Fe Nanoparticles in Tubular Lecithin Colloids. *IEEE Trans. Magn.* **1996**, *32*, 4490–4492.

(150) Cain, J. L.; Nikles, D. E. Preparation of Acicular Iron Nanoparticles by the Reduction of Ferrous Salt in the Presence of Tubular Lecithin Assemblies. *J. Appl. Phys.* **1996**, *79*, 4860.

(151) Gubin, S. P.; Koksharov, Y. a; Khomutov, G. B.; Yurkov, G. Y. Magnetic Nanoparticles: Preparation, Structure and Properties. *Russ. Chem. Rev.* **2005**, *74*, 489–520.

(152) Prozorov, T.; Prozorov, R.; Koltypin, Y.; Felner, I.; Gedanken, A. Sonochemistry under an Applied Magnetic Field: Determining the Shape of a Magnetic Particle. *J. Phys. Chem. B* **1998**, *102*, 10165–10168.

(153) Li, D.; Kaner, R. B. Shape and Aggregation Control of Nanoparticles: Not Shaken, Not Stirred. *J. Am. Chem. Soc.* **2006**, *128*, 968–975.

(154) Alvarez, M. M.; Zalc, J. M.; Shinbrot, T.; Arratia, P. E.; Muzzio, F. J. Mechanisms of Mixing and Creation of Structure in Laminar Stirred Tanks. *AIChE J.* **2002**, *48*, 2135–2148.

(155) Huber, D. L. Synthesis, Properties, and Applications of Iron Nanoparticles. *Small* **2005**, *1*, 482–501.

(156) Veitch, R. .; Ilmer, A.; Lenz, W.; Richter, V. MP Technology for a New Generation of Magnetic Tapes. *J. Magn. Magn. Mater.* **1999**, *193*, 279–283.

(157) Vereda, F.; de Vicente, J.; Hidalgo-Alvarez, R. Physical Properties of Elongated Magnetic Particles: Magnetization and Friction Coefficient Anisotropies. *Chemphyschem* **2009**, *10*, 1165–1179.

(158) Lu, A.-H.; Salabas, E. L.; Schüth, F. Magnetic Nanoparticles: Synthesis, Protection, Functionalization, and Application. *Angew. Chemie Int. Ed.* **2007**, *46*, 1222–1244.

(159) Batlle, X.; Labarta, A. Finite-Size Effects in Fine Particles: Magnetic and Transport Properties. *J. Phys. D. Appl. Phys.* **2002**, *35*, R15–R42.

(160) Kodama, R. . Magnetic Nanoparticles. *J. Magn. Magn. Mater.* **1999**, *200*, 359–372.

(161) Al-Ali, Z. A.; Al-Buali, M. H.; AlRuwaili, S.; Ma, S. M.; Marsala, A. F.; Alumbaugh, D.; DePavia, L.; Levesque, C.; Nalonnil, A.; Zhang, P.; *et al.* Looking Deep into the Reservoir. *Oilf. Rev.* **2009**, 38–47.

(162) Saleh, N.; Kim, H.; Phenrat, T.; Matyjaszewski, K.; Tilton, R. D.; Lowry, G. V. Ionic Strength and Composition Affect the Mobility of Surface-Modified Fe 0 Nanoparticles in Water-Saturated Sand Columns. *Environ. Sci. Technol.* **2008**, *42*, 3349–3355.

(163) Laurent, S.; Forge, D.; Port, M.; Roch, A.; Robic, C.; Vander Elst, L.; Muller, R. N. Magnetic Iron Oxide Nanoparticles: Synthesis, Stabilization, Vectorization,

Physicochemical Characterizations, and Biological Applications. *Chem. Rev.* **2008**, *108*, 2064–2110.

(164) Ryoo, S.; Rahmani, A. R.; Yoon, K. Y.; Prodanović, M.; Kotsmar, C.; Milner, T. E.; Johnston, K. P.; Bryant, S. L.; Huh, C. Theoretical and Experimental Investigation of the Motion of Multiphase Fluids Containing Paramagnetic Nanoparticles in Porous Media. *J. Pet. Sci. Eng.* **2012**, *81*, 129–144.

(165) Berlin, J. M.; Yu, J.; Lu, W.; Walsh, E. E.; Zhang, L.; Zhang, P.; Chen, W.; Kan, A. T.; Wong, M. S.; Tomson, M. B.; *et al.* Engineered Nanoparticles for Hydrocarbon Detection in Oil-Field Rocks. *Energy Environ. Sci.* **2011**, *4*, 505–509.

(166) Lee, H.; Shin, T.-H.; Cheon, J.; Weissleder, R. Recent Developments in Magnetic Diagnostic Systems. *Chem. Rev.* **2015**, *115*, 10690–10724.

(167) Wu, W.; He, Q.; Jiang, C. Magnetic Iron Oxide Nanoparticles: Synthesis and Surface Functionalization Strategies. *Nanoscale Res. Lett.* **2008**, *3*, 397–415.

(168) Dunn, A. S. Polymeric Stabilization of Colloidal Dispersions. By D. H. Napper, Academic Press, London, 1984. Pp. Xviii + 428, Price £39.50, $65.00. ISBN 0-12-513980-2. *Br. Polym. J.* **1986**, *18*, 278–278.

(169) Arjunan Vasantha, V.; Junhui, C.; Ying, T. B.; Parthiban, A. Salt-Responsive Polysulfabetaines from Acrylate and Acrylamide Precursors: Robust Stabilization of Metal Nanoparticles in Hyposalinity and Hypersalinity. *Langmuir* **2015**, *31*, 11124–11134.

(170) Kowalczuk, A.; Trzcinska, R.; Trzebicka, B.; Müller, A. H. E.; Dworak, A.; Tsvetanov, C. B. Loading of Polymer Nanocarriers: Factors, Mechanisms and Applications. *Prog. Polym. Sci.* **2014**, *39*, 43–86.

(171) Li, X.; Lenhart, J. J.; Walker, H. W. Dissolution-Accompanied Aggregation Kinetics of Silver Nanoparticles. *Langmuir* **2010**, *26*, 16690–16698.

(172) Huynh, K. A.; Chen, K. L. Aggregation Kinetics of Citrate and Polyvinylpyrrolidone Coated Silver Nanoparticles in Monovalent and Divalent Electrolyte Solutions. *Environ. Sci. Technol.* **2011**, *45*, 5564–5571.

(173) Sinn, C. G.; Dimova, R.; Antonietti, M. Isothermal Titration Calorimetry of the Polyelectrolyte/Water Interaction and Binding of Ca 2+ : Effects Determining the Quality of Polymeric Scale Inhibitors. *Macromolecules* **2004**, *37*, 3444–3450.

(174) Lages, S.; Lindner, P.; Sinha, P.; Kiriy, A.; Stamm, M.; Huber, K. Formation of Ca 2+ -Induced Intermediate Necklace Structures of Polyacrylate Chains. *Macromolecules* **2009**, *42*, 4288–4299.

(175) Newman, J. K.; Mccormick, C. L. Water-Soluble Copolymers. 52. Sodium-23 NMR Studies. **1994**, 5114–5122.

(176) Newman, J. K.; McCormick, C. L. Water-Soluble Copolymers. 52. Sodium-23 NMR Studies of Ion-Binding to Anionic Polyelectrolytes: Poly(sodium 2-Acrylamido-2-Methylpropanesulfonate), Poly(sodium 3-Acrylamido-3-Methylbutanoate), Poly(sodium Acrylate), and Poly(sodium Galacturonate). *Macromolecules* **1994**, *27*, 5114–5122.

(177) Ditsch, A.; Laibinis, P. E.; Wang, D. I. C.; Hatton, T. A. Controlled Clustering and Enhanced Stability of Polymer-Coated Magnetic Nanoparticles Controlled Clustering and Enhanced Stability of Polymer-Coated Magnetic Nanoparticles. **2005**.

(178) Yoon, K. Y.; Kotsmar, C.; Ingram, D. R.; Huh, C.; Bryant, S. L.; Milner, T. E.; Johnston, K. P. Stabilization of Superparamagnetic Iron Oxide Nanoclusters in Concentrated Brine with Cross-Linked Polymer Shells. *Langmuir* **2011**, *27*, 10962–10969.

(179) Ersenkal, D. A.; Ziylan, A.; Ince, N. H.; Acar, H. Y.; Demirer, M.; Copty, N. K. Impact of Dilution on the Transport of Poly(acrylic Acid) Supported Magnetite Nanoparticles in Porous Media. *J. Contam. Hydrol.* **2011**, *126*, 248–257.

(180) Bagaria, H. G.; Neilson, B. M.; Worthen, A. J.; Xue, Z.; Yoon, K. Y.; Cheng, V.; Lee, J. H.; Velagala, S.; Huh, C.; Bryant, S. L.; *et al.* Adsorption of Iron Oxide Nanoclusters Stabilized with Sulfonated Copolymers on Silica in Concentrated NaCl and CaCl2 Brine. *J. Colloid Interface Sci.* **2013**, *398*, 217–226.

(181) Bagaria, H. G.; Yoon, K. Y.; Neilson, B. M.; Cheng, V.; Lee, J. H.; Worthen, A. J.; Xue, Z.; Huh, C.; Bryant, S. L.; Bielawski, C. W.; *et al.* Stabilization of Iron Oxide Nanoparticles in High Sodium and Calcium Brine at High Temperatures with Adsorbed Sulfonated Copolymers. *Langmuir* **2013**, *29*, 3195–3206.

(182) Bagaria, H. G.; Xue, Z.; Neilson, B. M.; Worthen, A. J.; Yoon, K. Y.; Nayak, S.; Cheng, V.; Lee, J. H.; Bielawski, C. W.; Johnston, K. P. Iron Oxide Nanoparticles Grafted with Sulfonated Copolymers Are Stable in Concentrated Brine at Elevated Temperatures and Weakly Adsorb on Silica. *ACS Appl. Mater. Interfaces* **2013**, *5*, 3329–3339.

(183) Xue, Z.; Foster, E.; Wang, Y.; Nayak, S.; Cheng, V.; Ngo, V. W.; Pennell, K. D.; Bielawski, C. W.; Johnston, K. P. Effect of Grafted Copolymer Composition on Iron Oxide Nanoparticle Stability and Transport in Porous Media at High Salinity. *Energy & Fuels* **2014**, *28*, 3655–3665.

(184) Ureña-Benavides, E. E.; Lin, E. L.; Foster, E. L.; Xue, Z.; Ortiz, M. R.; Fei, Y.; Larsen, E. S.; Kmetz, A. A.; Lyon, B. A.; Moaseri, E.; *et al.* Low Adsorption of Magnetite Nanoparticles with Uniform Polyelectrolyte Coatings in Concentrated Brine on Model Silica and Sandstone. *Ind. Eng. Chem. Res.* **2016**, *55*, 1522–1532.

(185) Kmetz, A. a.; Becker, M. D.; Lyon, B. a.; Foster, E.; Xue, Z.; Johnston, K. P.; Abriola, L. M.; Pennell, K. D. Improved Mobility of Magnetite Nanoparticles at

High Salinity with Polymers and Surfactants. *Energy & Fuels* **2016**, *30*, 1915–1926.

(186) Zhang, L.; Xue, H.; Gao, C.; Carr, L.; Wang, J.; Chu, B.; Jiang, S. Imaging and Cell Targeting Characteristics of Magnetic Nanoparticles Modified by a Functionalizable Zwitterionic Polymer with Adhesive 3,4-Dihydroxyphenyl-L-Alanine Linkages. *Biomaterials* **2010**, *31*, 6582–6588.

(187) Chanteau, B.; Fresnais, J.; Berret, J.-F. Electrosteric Enhanced Stability of Functional Sub-10 Nm Cerium and Iron Oxide Particles in Cell Culture Medium. *Langmuir* **2009**, *25*, 9064–9070.

(188) Barrera, C.; Herrera, A. P.; Bezares, N.; Fachini, E.; Olayo-Valles, R.; Hinestroza, J. P.; Rinaldi, C. Effect of Poly(ethylene Oxide)-Silane Graft Molecular Weight on the Colloidal Properties of Iron Oxide Nanoparticles for Biomedical Applications. *J. Colloid Interface Sci.* **2012**, *377*, 40–50.

(189) Amstad, E.; Textor, M.; Reimhult, E. Stabilization and Functionalization of Iron Oxide Nanoparticles for Biomedical Applications. *Nanoscale* **2011**, *3*, 2819.

(190) Lattuada, M.; Hatton, T. A. Functionalization of Monodisperse Magnetic Nanoparticles. *Langmuir* **2007**, *23*, 2158–2168.

(191) Peng, J.; Liu, Q.; Xu, Z.; Masliyah, J. Synthesis of Interfacially Active and Magnetically Responsive Nanoparticles for Multiphase Separation Applications. *Adv. Funct. Mater.* **2012**, *22*, 1732–1740.

(192) López-Cruz, A.; Barrera, C.; Calero-DdelC, V. L.; Rinaldi, C. Water Dispersible Iron Oxide Nanoparticles Coated with Covalently Linked Chitosan. *J. Mater. Chem.* **2009**, *19*, 6870.

(193) Xue, Z.; Foster, E.; Wang, Y.; Nayak, S.; Cheng, V.; Ngo, V. W.; Pennell, K. D.; Bielawski, C. W.; Johnston, K. P. Effect of Grafted Copolymer Composition on Iron Oxide Nanoparticle Stability and Transport in Porous Media at High Salinity. *Energy & Fuels* **2014**, *28*, 3655–3665.

(194) Wang, C.; Yan, Q.; Liu, H. B.; Zhou, X. H.; Xiao, S. J. Different EDC/NHS Activation Mechanisms between PAA and PMAA Brushes and the Following Amidation Reactions. *Langmuir* **2011**, *27*, 12058–12068.

(195) Ranka, M.; Brown, P.; Hatton, T. A. Responsive Stabilization of Nanoparticles for Extreme Salinity and High-Temperature Reservoir Applications. *ACS Appl. Mater. Interfaces* **2015**, *7*, 19651–19658.

(196) Čampelj, S.; Makovec, D.; Drofenik, M. Functionalization of Magnetic Nanoparticles with 3-Aminopropyl Silane. *J. Magn. Magn. Mater.* **2009**, *321*, 1346–1350.

(197) Wang, Y.; Li, Y.; Costanza, J.; Abriola, L. M.; Pennell, K. D. Enhanced Mobility of Fullerene (C 60) Nanoparticles in the Presence of Stabilizing Agents. *Environ. Sci. Technol.* **2012**, *46*, 11761–11769.

(198) Que, E. L.; Chang, C. J. Responsive Magnetic Resonance Imaging Contrast Agents as Chemical Sensors for Metals in Biology and Medicine. *Chem. Soc. Rev.* **2010**, *39*, 51–60.

(199) Somaskandan, K.; Veres, T.; Niewczas, M.; Simard, B. Surface Protected and Modified Iron Based Core-Shell Nanoparticles for Biological Applications. *New J. Chem.* **2008**, *32*, 201.

(200) Ma, Y.; Zhang, X.; Zeng, T.; Cao, D.; Zhou, Z.; Li, W.; Niu, H.; Cai, Y. Polydopamine-Coated Magnetic Nanoparticles for Enrichment and Direct Detection of Small Molecule Pollutants Coupled with MALDI-TOF-MS. *ACS Appl. Mater. Interfaces* **2013**, *5*, 1024–1030.

(201) Jeong, B. U.; Teng, X.; Wang, Y.; Yang, H.; Xia, Y.; Jeong, U.; Teng, X.; Wang, Y.; Yang, H.; Xia, Y. Superparamagnetic Colloids: Controlled Synthesis and Niche Applications. *Adv. Mater.* **2007**, *19*, 33–60.

(202) Bagaria, H. G.; Xue, Z.; Neilson, B. M.; Worthen, A. J.; Yoon, K. Y.; Nayak, S.; Cheng, V.; Lee, J. H.; Bielawski, C. W.; Johnston, K. P. Iron Oxide Nanoparticles Grafted with Sulfonated Copolymers Are Stable in Concentrated Brine at Elevated Temperatures and Weakly Adsorb on Silica. *ACS Appl. Mater. Interfaces* **2013**, *5*, 3329–3339.